



Showcasing research from Dr Ishita Neogi, Chemical Sciences and Technology Division, CSIR-NIIST, Thiruvananthapuram, Kerala, India, and Dr Keshaba N. Parida, School of Chemistry, IISER Thiruvananthapuram, Thiruvananthapuram, Kerala, India.

Fluorinated spacers: an effective strategy to tailor the optoelectronic properties and stability of metal-halide perovskites for photovoltaic applications

This highlight presents advances in fluorinated spacers in the realm of quasi-2D and 2D/3D-bilayer perovskites for applications in photovoltaics (PV). Also, extensively discussed are studies based on fluorinated spacer-based passivation to improve optoelectronic properties of perovskites for PV applications.

As featured in:



See Keshaba N. Parida, Ishita Neogi *et al.*, *J. Mater. Chem. C*, 2022, **10**, 16949.



Cite this: *J. Mater. Chem. C*, 2022, 10, 16949

## Fluorinated spacers: an effective strategy to tailor the optoelectronic properties and stability of metal-halide perovskites for photovoltaic applications

Gourab Mohanty,<sup>a</sup> Anjitha Sebastian,<sup>ab</sup> Haritha S.,<sup>a</sup> Keshaba N. Parida \*<sup>c</sup> and Ishita Neogi \*<sup>ab</sup>

Metal halide perovskites or simply known as perovskites are organic–inorganic hybrid materials that have surpassed silicon-based photovoltaic (PV) technology in terms of power-conversion efficiency (PCE). However, low environmental stability remains the key challenge to be addressed before the industrial prospects of perovskite-based PV technology are met. Ligand engineering to control dimensionality and tune optoelectronic properties of perovskites is the most attractive way to endow them with environmental stability, passivate defects, manoeuvre exciton binding energy, enhance carrier mobility, and improve carrier extraction along with the integration of other desirable properties into the perovskites. In this regard, the exploration of fluorinated spacer cations for developing perovskites for PV applications seems highly imperative. This highlight presents state-of-the-art recent developments in the area of multi-dimensional perovskites, particularly focusing on developments in the area by exploring fluorinated spacers with regard to quasi-2D and 2D/3D-bilayer perovskites to offer solutions to the key issues of stability, exciton binding energy, charge carrier mobility, defect passivation, and any other issues pertaining to perovskites for application in PV devices. Also literature reports of fluorinated spacer manifested passivation that could tailor the optoelectronic properties of perovskites for PV applications are covered.

Received 21st September 2022,  
Accepted 19th October 2022

DOI: 10.1039/d2tc03985k

rsc.li/materials-c

<sup>a</sup> Chemical Sciences and Technology Division, CSIR-NIIST, Thiruvananthapuram, Kerala, 695019, India. E-mail: ishita@niist.res.in

<sup>b</sup> Academy of Scientific and Innovative Research (AcSIR), Ghaziabad, 201002, India

<sup>c</sup> School of Chemistry, IISER Thiruvananthapuram, Thiruvananthapuram 695551, Kerala, India. E-mail: pkesh@iisertvm.ac.in

### 1. Introduction

Climate change due to global warming has posed the biggest threat to the diversity of life on earth. The recent collapse of ice glaciers of Antarctica as huge as the size of Rome is an indication of the side effects of the continuous rise in global



Gourab Mohanty

Gourab Mohanty obtained his BSc from Fakir Mohan University, Balasore, Odisha, India. He received his MSc degree in chemistry from Sambalpur University, Odisha, India. Currently he is working as a project associate at CSIR-National Institute for Interdisciplinary Science and Technology (CSIR-NIIST), Thiruvananthapuram, Kerala, India, under the supervision of Dr Ishita Neogi.



Anjitha Sebastian

Anjitha Sebastian received her BSc from St. Joseph's College for Women Alappuzha, Kerala, India. She obtained her MSc degree from Mahatma Gandhi University, Kerala, India. Currently, she is pursuing her PhD at CSIR-NIIST, Thiruvananthapuram, Kerala, India, under the supervision of Dr Ishita Neogi. Her ongoing PhD work mainly focuses on developing novel organic materials for application in solar cells.

## Highlight

temperature.<sup>1</sup> To undermine the effects of climate change, an immediate move towards green, sustainable, and carbon footprint-free energy is indispensable. In this direction, photovoltaic (PV) technologies for solar-light harvesting have brought dramatic breakthroughs in terms of generating green renewable energy in a carbon footprint-free fashion with high efficiency.<sup>2</sup>

Metal-halide perovskites (MHPs) or simply known as perovskites are represented with the general formula  $ABX_3$ .<sup>3</sup> These materials adopt a crystal structure similar to that of  $CaTiO_3$ , a well-known mineral, and are named after the crystallographer Lev Perovski.<sup>4</sup> These belong to the third generation of solar-light harvesting materials with excellent features that render them indispensable candidates for thin-film PVs.<sup>5</sup> Perovskites possess different dimensionality depending upon the propagation of the inorganic lattice. The three-dimensional perovskites are formed when the inorganic metal (B-site cation) halide (X) lattice propagates continuously over the three-dimensional space with the inclusion of small cations, like methylammonium (MA), formamidinium (FA), cesium (Cs), *etc.*, within the

interstitial lattice space.<sup>3,4,6</sup> The journey of perovskites towards PV applications began in 2009, when Miyasaka and co-workers explored  $MAPbI_3$  and  $MAPbBr_3$  nanocrystals decorated over  $TiO_2$  as sensitizers for dye-sensitized solar cells to achieve a power conversion efficiency (PCE) of 3.8%.<sup>7</sup> In 2012, a mesoscopic solid-state perovskite PV device was fabricated by Park and co-workers, where  $MAPbI_3$  was used as a light-harvesting layer offering a PCE of 9.7%.<sup>8</sup> The field of halide perovskites for PV applications continued to burgeon for the next few years, and in 2021, Seok and his group reported an efficiency of 25.5% by passivation of the perovskite and electron-transport layer (ETL) interface with  $SnO_2$ .<sup>9</sup> In a short period of nearly ten years, perovskites renaissance the era of thin-film PV technology by superseding crystalline silicon-based PV systems in terms of PCE from 3.8% to more than 25%, mostly in n-i-p configuration.<sup>7,9</sup> It is worth mentioning that crystalline silicon-based PV devices took several decades to attain a PCE of  $\sim 25\%$ , which was achieved with perovskite-based PV technology very rapidly in a shorter time span.<sup>10</sup> Also, there exists further room to improve the PCE of perovskite-based PV devices to 31–33%, as per the Shockley–Queisser limit.<sup>11</sup> Furthermore, the manufacture of silicon-based PV devices is an energy-intensive process, but it is not so in the case of perovskite PV devices, which has drawn colossal attention towards the R&D developments of perovskite PV devices from both academia and industry.<sup>12</sup> Although metals other than Pb are also explored as B-site cations to develop perovskites, like tin (Sn), germanium (Ge), bismuth (Bi), copper (Cu), *etc.*,<sup>13</sup> the low photon-to-current efficiency attributed to the unsuitable band gap, high trap density and high propensity towards oxidation led to the less popularity of Pb-free perovskites compared to Pb-based analogues for PV applications.<sup>13</sup>

This success of perovskites, mainly 3D-ones, is attributed to the unprecedented properties, such as high light absorption coefficient over the visible range ( $10^4$ – $10^5$   $M^{-1} cm^{-1}$ ),<sup>14</sup> low exciton binding energy ( $\sim 10$ – $50$  meV),<sup>15</sup> tuneable direct band gap,<sup>16,17</sup> great defect



**Haritha S.**

*Haritha S. received her BSc in chemistry from N.S.S College, Nemmara, Kerala, India. She obtained her MSc degree from N.G.M College Pollachi, Tamilnadu, India. Currently she is working as a project associate at CSIR-NIIST, Thiruvananthapuram, Kerala, India, under the supervision of Dr Ishita Neogi.*



**Keshaba N. Parida**

*Keshaba N. Parida received his BSc and MSc in Chemistry from Sambalpur University. He then moved to IIT Kanpur, where he obtained a PhD in organic synthesis under Prof. J. N. Moorthy. After PhD, he had two postdoctoral stints, first at Ariel University, Israel, with Prof. Alex M. Szpilman, and then at the University of Arizona, USA, with Prof. Dominic V. McGrath. Currently, he is a CSIR-SRA fellow (Pool Scientist) at IISER*

*Thiruvananthapuram, India. His research interests are oxidation chemistry based on hypervalent iodine compounds and exploring nanowire-type organic semiconductors.*



**Ishita Neogi**

*Ishita Neogi received her BSc and MSc from BHU, India. Thereafter, she pursued PhD in the JNM group at IIT Kanpur. Next, she joined Prof. Subodh Mhaisalkar at NTU, Singapore, for post-doctoral research. Thereafter, she moved to Ariel University, Israel, to pursue research under Prof. Flavio Grynspan. Following this, she joined the Szpilman group at Technion, Israel, for another post-doctoral stint. Since January 2019, Ishita has*

*been working as a scientist at CSIR-NIIST, Thiruvananthapuram. At NIIST, her research interest centres around design and development of new and efficient solar-light harvesting materials. Also, she is developing new materials for light emission and against SARS-CoV-2.*

tolerant attributes,<sup>18,19</sup> ambipolar nature,<sup>20</sup> low trap density,<sup>9</sup> long carrier diffusion length ( $100 \text{ nm}^{-1} \mu\text{M}$ ),<sup>20,21</sup> high carrier mobility,<sup>22</sup> feasibility of both solution processing and vacuum sublimation,<sup>23</sup> and abundantly available inexpensive precursors.<sup>24,25</sup> The solution processability enabled manufacture of large-scale PV modules cost-efficiently using perovskites.<sup>26</sup> However, to replace the market of polycrystalline silicon PV with perovskite technology, at least a minimum of 25 years of efficient operation is necessary to avoid the hassles of continuous replacement of solar panels.<sup>24</sup> Even though impressive PCE could be achieved using perovskite-based PV technology, stability upon exposure to thermal stress,<sup>27,28</sup> moisture,<sup>29–31</sup> oxygen<sup>17</sup> and UV-light<sup>32,33</sup> remains the major bottleneck, when a trade-off between cost, efficiency and stability is to be met for the commercial success of the technology.<sup>34</sup>

Intrinsic material problems caused by surface defects or defects at the grain boundaries of the perovskite film or crystal lower the barrier towards degradation due to moisture or oxygen leading to separation into non-functional phases.<sup>17,35,36</sup> Moisture penetration mainly takes place either from the surface or through grain boundaries.<sup>26</sup> Also, these grain boundaries act as the nucleation sites for the initiation of moisture or thermal induced degradation in the perovskite devices.<sup>37</sup> In addition, defects also invite trap-assisted carrier recombination, a highly detrimental process that affects PV performance.<sup>38</sup> Furthermore, the environment around the grain boundaries is also an important determinant of carrier transport and exciton binding energy.<sup>39</sup> Also, grain boundaries facilitate ion migration.<sup>40</sup> Generally, the ions with an unsatisfied coordination number present towards the surface of the perovskite or at the grain boundaries attract coordination of atmospheric water or oxygen molecules, initiating material decomposition.<sup>36</sup> Upon exposure to moisture, degradation of the perovskite layer into  $\text{PbI}_2$  is first mediated by the formation of  $\text{MAPbI}_3 \cdot \text{H}_2\text{O}$  which is further hydrated into  $(\text{MA})_4\text{PbI}_6 \cdot 2\text{H}_2\text{O}$ .<sup>31</sup> The HI generated as a by-product of the degradation under hot and humid conditions is also corrosive to the electrodes. Moreover, perovskite lattice expansion at higher temperature triggers oxygen and moisture penetration into the grain boundaries, further aggravating instability.<sup>37</sup> Decomposition under elevated temperature is also an intrinsic bottleneck associated with perovskites.<sup>37</sup> At higher temperature, ion diffusion due to the low energy of activation (*ca.* 0.2–0.8 eV) and morphological changes at the grain boundaries have been observed.<sup>37,41–43</sup> Venkatraman and co-workers found that thermally induced ion transport is related to the phase change due to perovskite lattice expansion, ultimately initiating device degradation.<sup>43</sup> Thus, to penetrate the commercial markets, a perovskite PV device should overcome all of these associated instability issues and qualify testing standards of IEC 61 646.<sup>44</sup>

In this regard, two-dimensional perovskites offer substantial environmental stability due to the incorporation of bulky spacer cations at the A-site, added by slicing inorganic sheets to form a water-proof jacket against the invasion of moisture. These 2D-perovskites can have (100), (110) or (111)-orientation depending upon the plane along which the A-site cations slices the inorganic lattice.<sup>3,6</sup> A well-defined quantum well structure with strong dielectric confinement and enhanced excitonic

characteristics are the features of 2D-perovskites.<sup>45</sup> The result of adding bulky spacer cations at the A-site is higher formation energy than that of 3D-perovskites.<sup>46</sup> It is mostly hydrogen bonding,  $\pi$ - or van der Waals interactions that are responsible for the well-organized self-assembly of spacer cations within the 2D-perovskite lattice.<sup>47</sup> Furthermore, 2D-perovskites are resilient towards degradation by thermal stress, oxygen and UV-light.<sup>2,48</sup> The advantages of incorporating big and hydrophobic spacer cations within the 2D-perovskite lattice are many, and are not just limited to offering moisture resistance or stability to ambient environmental factors, but tuning of optoelectronic properties is also feasible due to the changes in the inorganic metal halide lattice strain and quantum confinement in the two dimensions.<sup>2,6</sup> Mostly, non-conjugated or aliphatic A-site spacer cations do not contribute directly to the band edges; nevertheless, these cations can modulate the band edges to an extent due to the steric influence towards the overlap of Pb and I orbitals of the inorganic lattice.<sup>49</sup> The conjugated spacer cations depending upon their band edge or conjugation length may contribute towards light absorption.<sup>50</sup> Importantly, the steric strain imposed on the metal-halide lattice by the bulky spacer also hinders ion migration in 2D-perovskites.<sup>48</sup> Besides the steric effect, the bulky spacer cation also controls the directionality of inorganic metal-halide lattice growth. Additionally, the dielectric constant and the distance between the inorganic sheets are other factors controlled by the spacer cation in 2D-perovskites.<sup>12</sup> Even though due to the quantum confinement effect carrier transport takes place mostly through the inorganic sheet,<sup>51</sup> still the above are crucial factors that modulate carrier transport between organic and inorganic sheets.<sup>50</sup> Therefore, it is easily possible to integrate any exotic feature into 2D-perovskites by manoeuvring and engineering the spacer structurally.

Although 2D-perovskites can address the major stability issues pertaining to 3D-perovskites, these materials offer low PCE upon application as a light-harvesting layer in PV. The low efficiency of 2D-perovskites is the outcome of their high exciton binding energy (190–400 meV),<sup>52</sup> low out-of-plane carrier mobility or anisotropic mobility due to the insulating spacer cation,<sup>53</sup> high dielectric constant, wider band gap (2.6–2.9 eV),<sup>26</sup> quantum well structure and short diffusion length due to the strong attraction between excitons.<sup>2,54,55</sup> The influence of all these factors renders 2D-perovskites not very prospective as a solar absorber for high efficiency PV devices.<sup>56</sup>

Perovskite PV devices are generally fabricated by solution processing, which is in a way advantageous in terms of lowering the production cost. However, at the same time solution processing makes the film susceptible to defect formation either at the grain boundaries or at the surface, which also serves as the trap sites as well as the sites for degradation by external factors. Hence, 2D and 3D-perovskites have their respective advantages and disadvantages, when considered for PV applications. The best strategy to retain the superior properties of both higher- and lower-dimensional counterparts in a single film of perovskite is to develop multi-dimensional perovskites (MDPs). These multi-dimensional perovskites are apt to attain a trade-off between environmental stability and

## Highlight

PCE by limiting the quantum confinement. Multi-dimensional perovskites can be divided into two classes: (1) quasi-2D perovskites or mixed-dimensional perovskites;<sup>57</sup> and (2) low-dimensional 2D/3D-bilayer perovskites.<sup>31</sup>

Quasi 2D-perovskites possess mostly (100)-orientation and are mainly of two kinds: (1) Ruddlesden–Popper (RP) quasi 2D-perovskite, represented with the formula  $[(\text{RNH}_3)_2\text{A}_{n-1}\text{B}_n\text{X}_{3n+1}]$  ( $n = 2, 3, 4, 5, \dots$ ), and (2) Dion–Jacobson (DJ) quasi 2D-perovskite represented with the formula  $[(\text{R}(\text{NH}_3)_2) \text{A}_{n-1}\text{B}_n\text{X}_{3n+1}]$  ( $n = 2, 3, 4, 5, \dots$ ).<sup>6,58</sup> Here, R is a bulky aliphatic or aromatic spacer cation and A is the monovalent cation, mostly MA, FA, *etc.* The B in the formula represents the divalent metal cation and  $n$  is the number of continuous inorganic layers.<sup>59</sup> Mostly, these quasi 2D-perovskites are comprised of self-assembling inorganic sheets of different numbers ( $n > 1$ ), where monoammonium cations (RP-type) or diammonium cations (DJ-type) slice the self-assembling inorganic sheets along the (100) plane.<sup>2,6</sup> As with 2D-perovskites here too the organic spacer acts as a barrier for moisture penetration by insulating the metal-halide lattice.<sup>60,61</sup> These quasi 2D-perovskites are primarily stabilized by hydrogen bonding between ammonium headgroups and halide ions of the inorganic sheet.<sup>58</sup> Along with this, the interplay of other non-covalent interactions extended by the spacer is also responsible for the self-assembly of the organic sheet.<sup>58</sup> When an ideal RP-type perovskite is considered, two inorganic sheets are settled at an offset, but such offset of the inorganic sheet is absent in an ideal DJ-structure.<sup>58</sup> Nevertheless, deviations from the ideal structure of type RP or DJ are also possible.<sup>58</sup> In quasi 2D-perovskites, organic spacer cations not only segregate inorganic sheets but also passivate defects, conferring high stability towards different environmental factors along with improving PCE.<sup>62</sup> Noteworthy, by varying the thickness of inorganic sheets ( $n$ ) in these quasi 2D-perovskites, different degrees of quantum confinement can be achieved to tailor desirable exciton binding energy, carrier mobility and ultimately PV performance.<sup>50</sup> The phase distribution, crystal growth orientation and film morphology manoeuvre carrier transport, ion migration and trapping in these quasi 2D-perovskites, ultimately effecting PV performance.<sup>50,63,64</sup> It is well-known that RP-type structures contain a van der Waals gap, absent in the DJ-type quasi 2D-perovskites.<sup>6</sup> In the RP-type structure, monoammonium ligands self-assemble between inorganic sheets, and are primarily held by nondirectional, nonspecific and distance dependent van der Waals interactions.<sup>62</sup> However, in the DJ-type perovskite, the van der Waals gap closes due to the diammonium spacer, and inorganic sheets are primarily held by strong hydrogen bonding with the organic layers and electrostatic interactions, which increases the electronic coupling between the inorganic sheets, further improving carrier transport and ambient stability.<sup>2,65</sup> However, DJ-type perovskite structures are difficult to attain due to the harsh processing conditions and their reduced defect tolerant attributes.<sup>62</sup> It is to be noted that thermodynamic stability for any quasi 2D-perovskite decreases above  $n > 5$ , leading to the decomposition of larger slabs into smaller ones.<sup>66</sup> Also, the absorption edge decreases in energy with increasing number of continuous inorganic slabs ( $n$ ).<sup>6</sup> It has also been shown

that reorganization freedom of inorganic slabs in the quasi 2D-perovskite leads to a low-energy edge state, offering exciton dissociation.<sup>2,67</sup> To date, versatile architectures of spacers, including aliphatic, aromatic or different heterocyclic scaffolds with varying anchoring groups, have been explored for RP- and DJ-type perovskites towards PV applications.<sup>68–70</sup> Examples of these different spacers are phenylethylammonium (PEA),<sup>71</sup> 1,4-phenylenedimethylammonium,<sup>72</sup> benzylammonium (BA),<sup>73</sup> naphthalenemethylammonium,<sup>74</sup> anthracenemethylammonium,<sup>74</sup> 4-(aminoethyl)pyridine,<sup>75</sup> alkylammoniumbenzodithiophene,<sup>76</sup> thiophene-2-ethylamine,<sup>77</sup> 3- or 4-(aminomethyl)piperidinium,<sup>78</sup> benzamidine,<sup>59</sup> *etc.*

In 2D/3D-bilayer perovskites a thin passivating capping layer of 2D-perovskite self-assembles on top of the bulk 3D-material, enhancing stability towards moisture penetration without much compromise of PCE.<sup>31,79</sup> Furthermore, this capping layer passivates trap states and recombination centres at the grain boundaries.<sup>11</sup> Also, 2D/3D-bilayer perovskites possess some extent of quantum confinement due to the presence of the 2D-capping layer.<sup>80</sup> Here, the organic ammonium cation replaces the A-site cation to self-assemble into a bilayer structure upon exposure of a film of 3D-perovskite to the spacer cations. The stronger interaction of the spacer with the inorganic lattice ultimately leads to the replacement of the A-site cations with the spacer.<sup>53</sup> Also, low dimensional phases can self-assemble around the grain boundaries passivating the trap states to reduce losses due to non-radiative recombination and control the interfacial interactions at the boundary between 2D/3D or at the interface between perovskite and other transport layers of the PV device.<sup>31</sup>

Both quasi-2D and 2D/3D-bilayer perovskites not only provide a barrier towards moisture penetration, but also confer thermal stability and photostability due to the passivation of trap or defect states at the grain boundaries as already discussed.<sup>31,81</sup> It is also possible to combine a protective capping layer of RP-type 2D-perovskite over 3D-perovskite in the form of a 2D/3D-bilayer structure to offer extended environmental stability, along with passivation at the grain boundaries.<sup>82</sup> Thus, besides environmental stability, improved PCE of PV devices could be achieved from these multi-dimensional perovskites.<sup>83</sup> The low-dimensional phase also controls the crystal growth kinetics at the 2D/3D-interface and may provide a contact surface with the adjacent hole- or electron-transport layers in a PV device.<sup>79</sup> By using *n*-butylammonium (BuA) or PEA as spacer cations for 2D/3D-bilayer perovskites, a PCE of over 20% has been achieved.<sup>82</sup> Concomitantly, other kinds of spacers, like cyclohexylmethylammonium,<sup>84</sup> imidazole,<sup>85</sup> photo-crosslinkable 4-vinylbenzylammonium,<sup>86</sup> *s*-benzyl-L-cysteine,<sup>87</sup> 2,2-(ethylenedioxy)bis(ethylammonium),<sup>88</sup> *etc.*, have also been explored to develop 2D/3D-bilayer perovskites for PV applications. Subsequently, the search has been for more resilient spacer cations that can confer higher stability to the corresponding 2D/3D-bilayer perovskite without hampering carrier mobility to further boost PCE.<sup>79</sup> Moreover, the spacer cations that can limit the effect of quantum confinement in these 2D/3D-bilayer perovskites and further lower the exciton binding energy are also under exploration.<sup>80</sup> Likewise, the spacer cations that do not impact carrier transport

at the interface of 2D–3D layers through oriented alignment of the 2D-lattice over the 3D-layer are also exceedingly sought after.<sup>79</sup>

Hence, the best possible way to tailor a multi-dimensional perovskite to impart environmental stability towards moisture, heat, and oxygen, and to tune other photophysical properties is to structurally manoeuvre the spacer cation or ligand. Furthermore, substantial resistance towards photo-bleaching can be obtained through spacer engineering.<sup>89</sup> This opens up a plethora of opportunities for synthetic chemists to explore different possibilities of stereoelectronic effects to diversely engineer and functionalize spacer cations/ligands for developing perovskites to tailor optoelectronic properties, enhance carrier mobility, improve defect tolerance, and integrate long-term environmental stability.

Due to the electron density inversion upon hydrogen to fluorine substitution the molecular packing in the solid state or crystals could be manoeuvred.<sup>90</sup> Hence, the strategy of fluorine substitution to enhance molecular packing and to improve molecular planarity has been well adopted to develop polymers for organic photovoltaics (OPVs).<sup>91,92</sup> Further, fluorine substitution is also known to exert C–F···H, F···F, F···S, and F··· $\pi$  interactions, which not only enhances planarity, but also improves carrier mobility and crystallinity of polymers for application in bulk-heterojunction OPVs.<sup>90,93</sup> Fluorinated polymers when applied in organic field-effect transistors (OFETs) could substantially lower the LUMO energy level compared to the corresponding non-fluorinated analogues due to the electronegativity effect of the fluorine atom, which enhances the n-type transport properties.<sup>94</sup> The herringbone packing in the solid state due to the interaction of electronegative fluorine atoms with the pentacene core in perfluoropentacene improved the electron conductivity in OFETs.<sup>95</sup> Similarly, fluorine-substituted fullerenes are also known to be strong n-type acceptors due to the electron withdrawing attribute of the fluorine atom.<sup>90</sup> This n-type property of fluorinated fullerenes has also been explored for passivating perovskites, and will be discussed later. Also, fluorinated emitters like FIrpic have been well explored in the realm of phosphorescent organic light-emitting diodes (PhOLEDs).<sup>96</sup> Besides HOMO–LUMO manoeuvring, the low-vibrational frequency of the C–F bond could lower non-radiative decay in these heavy-metal complexes improving the emission efficiency of FIrpic.<sup>96</sup> Fluorinated polyphenylenes are chemically as well as thermally stable electron-transporting-hole-blocking materials for application in OLEDs, where thermal and chemical stability are imparted by the strong C–F bonds.<sup>96</sup> Other fluorine-tethered molecules also find application as electron-transport materials in OLEDs.<sup>97</sup> These observations indicate that fluorination of materials has been an exceptionally well received engineering approach to tune the optoelectronic properties. Along similar lines, fluorination of spacers to tailor the optoelectronic and other properties of perovskites has been strategically adopted in the area of PV research due to the diverse beneficial influences this small atom can exert, which are discussed in the following section.

## 2. Advantages of fluorine-based spacers for multi-dimensional perovskites

As already discussed, the approach of fluorination to manoeuvre morphology, energy levels, carrier mobility and intermolecular packing is well established in the realm of OPVs for developing materials with improved PV performance.<sup>98</sup> The swapping of fluorine, with average van der Waals and covalent radii of  $\sim 147$  and  $57 \pm 3$  pm (CSD) respectively, with hydrogen having  $\sim 110$  and  $31 \pm 5$  pm (CSD), respectively, does not alter the molecular size of a spacer cation very significantly.<sup>50</sup> Hence, considering not much enhancement in the steric restrictions upon hydrogen to fluorine substitution in a spacer cation, minimal structural distortions are expected in the perovskite structure.<sup>99</sup> Nevertheless, fluorinated spacers due to their high dipole moment confer a high dielectric constant and lower the quantum confinement in a multi-dimensional perovskite.<sup>61</sup> Enhancement in the dipole moment of a spacer cation also lowers the exciton binding energy favouring carrier separation.<sup>49,61,73,99</sup> In this regard, lowering of exciton binding energy due to the dipolar effect of fluorine with respect to 4-fluorophenylethylammonium (4-FPEA) and phenylethylammonium (PEA) cations is reported.<sup>45</sup> The dipole moments of different fluorinated aryl spacer cations explored for developing perovskites have been collated in the review article by Zhou and co-workers (*cf.* Fig. 1).<sup>100</sup> Thus, fluorination of spacer cations/ligands has been identified as an effective strategy to lower the exciton binding energy and to tune the optoelectronic properties of multi-dimensional perovskites with the simultaneous incorporation of hydrophobicity and new exotic features.<sup>59</sup> Nevertheless, a fluorinated spacer also favours better distribution of phases and reorientation of lattice growth from a horizontal to vertical direction facilitating cascade energy transfer and carrier transport across the perovskite.<sup>101</sup> Due to the high electronegativity of fluorine, fluorinated spacers can substantially increase the dipole moments rendering strong interactions with the metal-halide lattice.<sup>102</sup> Upon fluorination, not only the ionic bond strengthens, but also the hydrogen bond becomes stronger, which stabilizes the perovskite lattice.<sup>49</sup> A strong hydrogen bond between the fluorine atom and the ammonium group of the adjacent spacer within the organic sheet of  $(4\text{-FBA})_2\text{PbI}_4$  has been reported, where BA represents benzylammonium.<sup>58</sup> In addition to contributing towards stronger hydrogen bonds, fluorine-tethered spacers due to their high dipole moment also exert a strong inductive effect.<sup>103</sup> Likewise, fluorine substitution in the spacer induces strong non-covalent dipole–dipole interactions within the organic layer of the perovskite.<sup>60,65</sup> Stronger van der Waals interactions between organic and inorganic parts of the perovskite in the presence of a fluorinated spacer than that of the corresponding hydrogen analogues have been identified.<sup>99</sup> Also,  $\pi$ – $\pi$  interactions are strong between fluorinated spacers in a perovskite lattice.<sup>58</sup> It is noteworthy that the location of fluorine in a spacer cation is as well important for the packing of the organic layer within the perovskite.<sup>50</sup> It has been demonstrated that the spacer cation becomes more polarized upon the addition of fluorine onto the

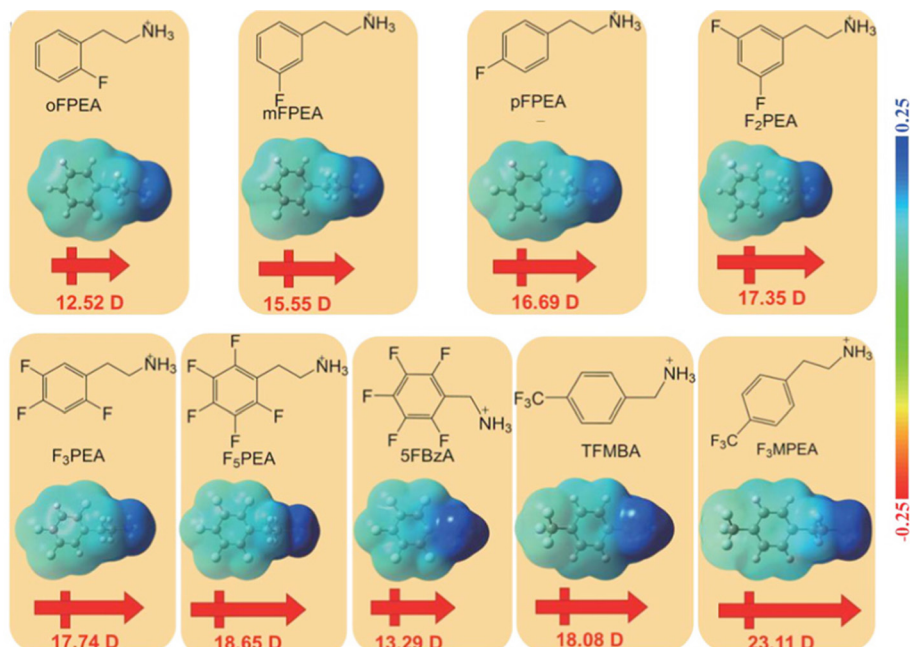


Fig. 1 Calculated dipole moments and electrostatic surface potentials (ESP) for different fluorinated spacers explored for developing perovskites (unit a.u.).<sup>100</sup> Reproduced with permission from ref. 100. Copyright 2022, IOPScience.

aromatic aryl ring, and this polarization may as well vary with the position of fluorine substitution.<sup>104</sup> Least polarization was observed for 4-fluorophenylethylammonium iodide (4-FPEAI or *p*-FPEAI) due to a greater symmetry than the corresponding *ortho* or *para*-isomers, *i.e.*, 2/3-FPEAI. This led to the highest exciton binding energy for 4-FPEAI-based layered perovskites, followed by 3-FPEAI- and 2-FPEAI-based layered perovskites.<sup>104</sup> Moreover, fluorine mediated polarization is known to influence other optical properties of perovskites.<sup>104</sup> These strong interactions and hydrogen bonding between fluorine atoms and the inorganic lattice improved the thermal stability of perovskites, as more heat could break these forces. Uniform and compact film morphology with minimum grain boundaries was achieved upon using fluorinated spacers due to the strong interactions.<sup>60</sup> Not only these, the entire perovskite lattice could be polarized by using fluorinated spacer cations possessing a high dipole moment, which could improve photogenerated carrier segregation, carrier mobility and carrier lifetime.<sup>49,99,105</sup> The high dipole moment of fluorinated spacers also shifts the Fermi energy level, which too further supports segregation of photogenerated charges.<sup>100</sup> It has been shown that fluorinated spacers may also red shift the absorption edge compared to non-fluorinated analogues.<sup>61</sup> Anion- $\pi$  interactions in fluoroarene-based perovskites are highly effective to prevent ion migration within the lattice.<sup>47,49</sup> Hence, the coalition of all these factors strongly backs the use of fluorine-tethered spacers as a significant and novel design approach to modulate optoelectronic properties and integrate stability into multi-dimensional perovskites.<sup>102</sup>

Also, lower trap assisted exciton recombination and lower Auger recombination are known for fluorinated spacer-based perovskites compared to the corresponding hydrogen analogues.<sup>45</sup> A decrease in the Auger recombination for fluorinated spacer cations reduces

Joule heating, enhancing the perovskite device stability.<sup>45</sup> Compared to aliphatic spacer cations, better delocalization of charges, easy functionalization, higher conductivity, higher dielectric constants, lower exciton binding energies, reduced interlayer spacings and higher hydrophobicity are expected from more rigid aromatic spacers, making them an obvious choice to investigate the effect of fluorination on the optoelectronic properties of perovskites.<sup>61,73,99</sup> Also, aromatic spacers can stabilize iodine defects due to their highly delocalized electronic structure, conferring better carrier transport than aliphatic spacers.<sup>80</sup> In contrast to arenes, fluoroarenes were shown to possess a reverse quadrupole moment, favouring a co-facial arrangement of the arene-fluoroarene mixed cation perovskite (*cf.* Fig. 2).<sup>47</sup>

It is not electrostatic but rather van der Waals interactions that determine the affinity of any surface towards water.

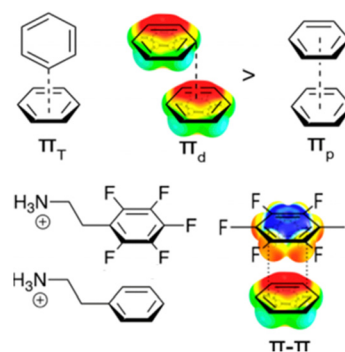


Fig. 2 Differences in arene-arene and arene-fluoroarene interactions to allow unlike modes of spacer stackings in perovskites.<sup>47</sup> Reproduced with permission from ref. 47. Copyright 2021, Creative Commons.

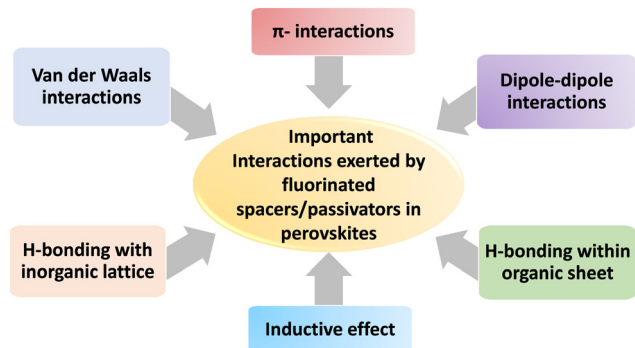


Fig. 3 Important interactions extended by fluorine-based spacers or passivators in perovskites.

The important interactions exerted by fluorine-based spacers are shown in Fig. 3. Accordingly, Dalvi and co-workers using atomistic molecular simulations showed that the hydrophobicity of fluorinated surfaces is an attribute of less dense surface packing and weak van der Waals interactions with water.<sup>106</sup> This allows water molecules to maintain their hydrogen bonded self-assembly structure upon interaction with a fluorinated surface.<sup>106</sup> Also, fluorine atoms due to their high electronegativity retard dispersion interactions which too contributes towards the water repulsive feature.<sup>53</sup> Likewise, the C–F bond is fatty in nature, repelling water penetration.<sup>107</sup> Remarkable hydrophobicity imparted by fluorine atoms has rendered fluorine-tethered materials a potential candidate for the making of superhydrophobic coatings.<sup>108</sup> In this respect, Teflon (polytetrafluoroethylene) is a well-known superhydrophobic polymer.<sup>107</sup> Hence, substitution with fluorine-based cations can create a barrier against moisture penetration and moisture-induced degradation of perovskite films.<sup>17,99</sup> Using computational studies, it has been shown that binding energy becomes highly repulsive towards interaction of water molecules with perovskites integrated with fluorinated spacers. This occurs due to the lone pair–lone pair repulsion between the fluorine atom of the spacer and the oxygen atom of the water molecule, which inhibits water binding and imparts hydrophobicity.<sup>64</sup> Besides offering superhydrophobicity, fluorinated cations also offer rigidity to the perovskites.<sup>12</sup> Likewise, superhydrophobic and conducting fluorinated spacers can passivate defects at the grain boundaries formed during solution processing, furthering thermal and moisture resistance without affecting carrier mobility.<sup>37,109</sup> Importantly, the passivation of defects at the grain boundaries is crucial to prevent moisture invasion. In this regard, Lermer and co-workers reported tremendous stability of several months for the crystals and films of  $(\text{FC}_2\text{H}_4\text{NH}_3)_2\text{PbCl}_4$ , even after exposure to ambient conditions.<sup>105</sup>

First, photostability upon incorporating fluorinated cations in perovskites was reported by Wei and co-workers.<sup>110</sup> Due to the presence of the electron withdrawing fluorine atom, the 4-FPEA-based spacer exhibited higher resistance towards photobleaching due to the impeding electrophilic attack of the transient photogenerated halogen radical ( $\text{X}^\bullet$ ).<sup>89,110</sup> Interestingly, the highest photostability was observed for the 4-FPEA

cation compared to the corresponding 2/3-FPEA cations. Nevertheless, it was also observed that the fluorine substituted spacer affects the emission efficiency of bromide-based perovskites probably due to the enhancement of non-radiative vibrational relaxation of the C–F bond.<sup>110</sup> As discussed at the beginning, even when not involved in the making of valence and conduction bands, the fluorinated spacer still influences the band gap of perovskites. The spacer cation size dependent tuning of band gap and exciton binding energy was reported by Grancini and co-workers.<sup>111</sup> It was observed that larger fluorinated spacers led to smaller band gap and exciton binding energy due to the strain imposed by the bulky spacer on the inorganic lattice leading to the dispersion of valence and conduction bands.<sup>111</sup> Due to these extended features, fluorine has been extensively used for imparting stability and tuning the properties of perovskites: (i) by substitution at the halide site;<sup>112</sup> or (ii) by substitution at the A-site;<sup>113</sup> or (iii) using fluorine-tethered organic molecules as an additive or passivator.<sup>37</sup>

Using density functional theory (DFT), Alharbi and co-workers demonstrated that controlled substitution of MA with difluorine-substituted MA could enhance the thermodynamic stability of the  $\text{MAPbI}_3$  lattice due to the formation of stronger hydrogen bonds between difluorine-substituted cations and the metal-halide lattice (*cf.* Fig. 4).<sup>102</sup> The elongation of the C–N bond in the difluorine-substituted MA was possible due to the higher electronegativity of fluorine, which also strengthened the hydrogen bond. Further, partial fluorination of MA also mitigated ion diffusion towards iodine vacancies by enhancing the energy barrier from  $\sim 0.3$  eV to  $\sim 0.5$  eV.<sup>102</sup>

First, a fluorinated cation-incorporated Sn-based perovskite was reported by Mitzi and co-workers.<sup>114–116</sup> Non-covalent fluoroarene–arene interactions to modulate the optoelectronic properties of Sn-based low-dimensional perovskites were also reported.<sup>116</sup> In 2001, Mitzi *et al.* adopted the strategy of fluorination to tune the electronic properties of Sn-based perovskites for field-effect transistors (FETs).<sup>114</sup> The authors in the work employed *ortho*-, *meta*- and *para*-fluorine substituted PEA cations and investigated the way the position of fluorine could influence the electronic properties of the corresponding FETs. The current density was observed to be highest for 4-FPEA-based perovskites and least for 2-FPEA-based

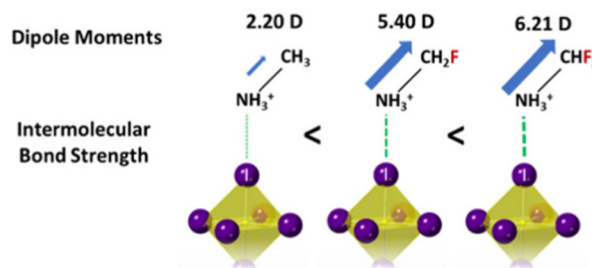


Fig. 4 The order of strengthening of the hydrogen bond between the A-site cation and the metal halide lattice due to the dipolar effect of fluorine.<sup>17</sup> Reproduced with permission from ref. 17. Copyright 2020, American Physical Society.



## Highlight

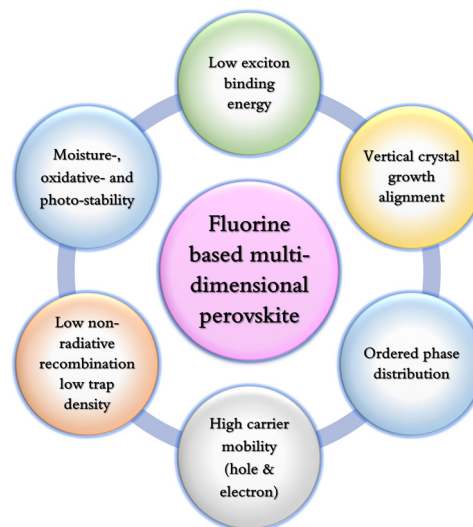
**Table 1** DFT-calculated physical parameters for perovskites with different A-site cations<sup>5</sup>

Cation	Molecular dipole (Debye, D)	Lattice electronic polarization ( $\mu\text{C cm}^{-2}$ )	Rotation barrier ( $\text{kJ mol}^{-1}$ )
$\text{CH}_3\text{NH}_3$ (MA)	2.29	38	1.3
$\text{CF}_3\text{NH}_3$	6.58	48	21.4

perovskites. Also, differences in the crystal structures, like Sn–I bond length, and variations in the interactions between organic and inorganic sheets were observed upon changing the position of fluorine substitution. Mitzi and Frost *et al.* also established that the polar fluorinated cation can enhance lattice polarization improving charge extraction and carrier lifetimes of perovskites.<sup>5</sup> In their work Frost *et al.* calculated and compared the extent of lattice polarization using Berry phase calculations, where A-site cations were either MA or its fluorinated analogue; the calculated molecular dipole, lattice polarization and rotation barrier are given in Table 1.

Although fluorinated spacers could improve the properties of perovskites mostly in a beneficial fashion, deviations from this useful attribute were noted in certain studies. For example, Grancini and co-workers reported band gap widening upon using a fluorinated spacer compared to a non-fluorinated spacer due to the steric influence exerted by fluorine atoms, which may not be cooperative towards PV applications.<sup>117</sup> Similarly, phase distribution was altered depending upon the choice of the fluorinated spacer, perovskite composition or processing conditions,<sup>50,60,65,73,101</sup> making prediction difficult regarding lattice orientation or phase distribution that could be achieved upon exploring a new fluorinated ligand for perovskites. Similarly, optoelectronic or structural properties as well as morphology of perovskites based on fluorinated spacers could vary widely and might even lead to a deteriorating PV performance depending upon the position of fluorine substitution, *vide infra*.<sup>50,73</sup> Similarly, the water repellent property was reported to be higher for the 4-OMePEAI-based spacer compared to the 4-FPEAI-based spacer.<sup>64</sup> Also, PV performance may manifest differently and depreciate depending upon the concentration of the fluorinated spacer used for developing a bilayer perovskite.<sup>11,118</sup> In some cases, even a better performance of non-fluorinated than fluorinated bilayer perovskites was noted.<sup>79</sup> Also, random orientation of lattice planes of 2D-perovskites in a bilayer structure was shown for 4-FPEAI and trifluorobutylammonium iodide ( $\text{CF}_3\text{BuAI}$ ) based spacers that led to higher trap density, higher recombination losses, lower defect passivation and lower electron mobility.<sup>82</sup> Be this as it may, nevertheless fluorine-based spacers were reported to be mostly salutary except the above cases, when performances towards PV applications based on these perovskites were taken into account.

In this highlight are presented insights and discussions regarding the way a fluorinated spacer in multi-dimensional perovskites influences different optoelectronic properties, simultaneously conferring stability towards various extrinsic factors (*cf.* Fig. 5). Such fundamental understanding is imperative to recognise different non-covalent interactions that a

**Fig. 5** Tailoring of optoelectronic properties and stability by exploration of fluorinated spacers or passivators.<sup>100</sup>

fluorinated spacer can extend to tune and improve the intrinsic properties of a perovskite, offering high PCE and resilience towards various external factors. Understanding these forces can also pave the way towards the discovery of new fluorine-tethered spacers/ligands to better modulate the perovskite lattice structurally to attain desirable optoelectronic properties and ambient stability along with higher conversion efficiency for PV applications. Herein, we collate comprehensive research done using fluorinated spacers to develop multi-dimensional perovskites, including RP-perovskites, DJ-perovskites and 2D/3D-bilayer perovskites, for PV applications. Also, we showcase literature reports of defect passivation at the surface or grain boundaries using fluorine-based molecules to attain superior PV performance.<sup>38</sup>

### 3. Fluorine-based spacers for quasi 2D RP-perovskites

In the section, an overall discussion of different arrays of fluorinated spacers and the way these could tune diverse properties of quasi 2D RP-perovskites crucial for application in PV devices are presented. The studies exploring aromatic 4-FPEAI-based quasi 2D RP-perovskites to integrate in-operando stability and allow vertical growth of the lattice in different RP-perovskite compositions are discussed in the beginning. Next, we showcase the way the properties of RP-perovskites could be manoeuvred by changing the position of the fluorine atom on the aryl ring of benzylammonium (BA)- or PEA-based spacers. What gives altogether different influences upon fluorine substitution on an aromatic spacer than substitution with other halogens (Cl/Br) or functional groups (OMe) is discussed in the following. The influences of quadrupole interactions extended by the multi-fluorinated aromatic ammonium spacer to manifest improvement in PV performances are discussed next. The studies based on RP-perovskites with an aromatic fluorinated spacer with

a different amidinium anchoring end group are organized thereafter. At the end of the section, studies of a RP-perovskite based on an aliphatic fluorinated spacer for application in PV devices are presented.

The first use of a moisture tolerant quasi 2D RP-perovskite  $(\text{PEA})_2(\text{MA})_2\text{Pb}_3\text{I}_{10}$  for PV application was shown by Karunadasa and co-workers in 2014.<sup>56</sup> The same group further explored a more hydrophobic 4-FPEAI spacer to develop an RP-type structure with  $n = 3$  (cf. Fig. 6a).<sup>26</sup> Comparison of the PXRD patterns revealed higher moisture tolerance for the film of the 4-FPEA-based perovskite compared to that of the PEA analogue (cf. Fig. 6b).<sup>26</sup>

To grow vertically orientated films of RP-perovskites with respect to the substrate, generally the hot casting method<sup>119,120</sup> or additive engineering techniques<sup>71,121,122</sup> are adopted. However, due to the difficulty in attaining precise substrate temperature and batch-to-batch reproducibility, the applications of both the hot casting method or additive engineering are limited. Zhu and co-workers showed that upon integration into the perovskite structure the 4-FPEA-based spacer not only enhanced the thermal stability but also allowed out-of-plane carrier mobility.<sup>113</sup> It was observed that the centroid-to-centroid distance reduced significantly between the spacer cations for the 4-FPEA-based perovskite compared to the PEA-based perovskite (Fig. 7). When  $n = 1$  (4-FPEA)<sub>2</sub>PbI<sub>4</sub> and (PEA)<sub>2</sub>PbI<sub>4</sub> were used for PV fabrication, a slightly higher PCE of 1.9% was achieved for 4-FPEA-based devices, likely due to the enhancement of out-of-plane carrier mobility, and was further confirmed from the time-resolved microwave conductivity (TRMC) studies. The TRMC studies revealed  $\sim 7$  times higher out-of-plane conductivity for (4-FPEA)<sub>2</sub>PbI<sub>4</sub> compared to (PEA)<sub>2</sub>PbI<sub>4</sub>. Single crystal studies also confirmed different intermolecular packing for PEA and 4-FPEA spacers inside the perovskite lattice.

Face-to-edge orientation was seen between PEA cations in the perovskite lattice, but face-to-face packing was confirmed for the 4-FPEA spacer leading to a reduced centroid to centroid ring distance (Fig. 7c and d).<sup>113</sup> DFT studies further confirmed that the face-to-face packing of cations in (4-FPEA)<sub>2</sub>PbI<sub>4</sub> was due to the long-range dispersion interactions. This clearly indicated that enhanced out-of-plane transport as observed for the (4-FPEA)<sub>2</sub>PbI<sub>4</sub> perovskite was due to the greater  $\pi$ -orbital overlap promoted by face-to-face packing of the spacer. However, crystal structure studies indicated a greater interlayer distance in (4-FPEA)<sub>2</sub>PbI<sub>4</sub> than (PEA)<sub>2</sub>PbI<sub>4</sub>, which also ruled out the dependence of out-of-plane conductivity upon the interlayer distance. According to the authors, tunnelling could be the mechanism of transport, and if so, not only the tunnelling distance but also the tunnelling barrier determined out-of-plane transport.<sup>113</sup> Also films of  $n = 4$  and 5 using PEA and 4-FPEA spacers along with the different stoichiometric ratios of MAI and PbI<sub>2</sub> were grown. Improved morphology with a larger grain size was observed for the films of the 4-FPEA-based spacer. Further, a 10-fold higher current was observed for  $n = 5$  films of 4-FPEA than for the PEA spacer during *c*-AFM studies. Similarly, TRMC studies indicated a higher carrier mobility of  $\sim 9 \text{ cm}^2 \text{ V}^{-1} \text{ s}^{-1}$  for (4-FPEA)<sub>2</sub>MA<sub>4</sub>Pb<sub>5</sub>I<sub>16</sub> than  $\sim 7 \text{ cm}^2 \text{ V}^{-1} \text{ s}^{-1}$  obtained for (PEA)<sub>2</sub>MA<sub>4</sub>Pb<sub>5</sub>I<sub>16</sub>. The PL lifetime was also higher for (4-FPEA)<sub>2</sub>MA<sub>4</sub>Pb<sub>5</sub>I<sub>16</sub> than (PEA)<sub>2</sub>MA<sub>4</sub>Pb<sub>5</sub>I<sub>16</sub>, suggesting a significant reduction in the defect density. The remarkable changes in the packing and orientation of the perovskite lattice rendered by fluorination of the spacer led to a significant improvement in the PCE of (4-FPEA)<sub>2</sub>MA<sub>4</sub>Pb<sub>5</sub>I<sub>16</sub> to 13.64%. However, only 9.6% of PCE could be achieved for the (PEA)<sub>2</sub>MA<sub>4</sub>Pb<sub>5</sub>I<sub>16</sub>-based device. Furthermore, thermal stability and environmental stability for the unencapsulated devices of (4-FPEA)<sub>2</sub>MA<sub>4</sub>Pb<sub>5</sub>I<sub>16</sub> vs. (PEA)<sub>2</sub>MA<sub>4</sub>Pb<sub>5</sub>I<sub>16</sub> were tested at 70 °C

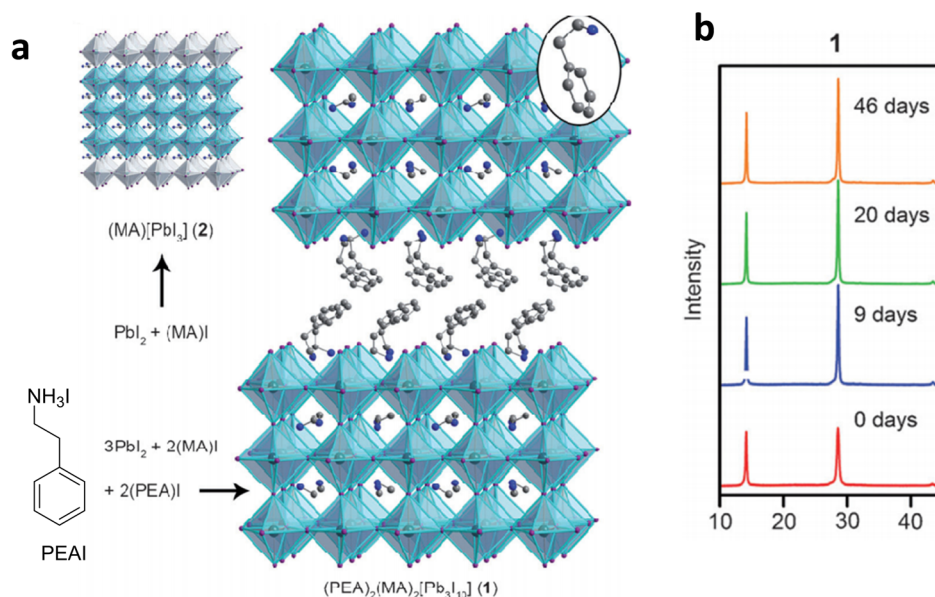


Fig. 6 (a) The crystal structure of the perovskite including the 4-FPEA cation with  $n = 3$ . (b) PXRD patterns for the films of MAPbI<sub>3</sub>-, PEA- and 4-FPEAI-based perovskites recorded over 0 days to 9 days at 66% relative humidity (RH).<sup>26</sup> Reproduced with permission from ref. 26. Copyright 2017, American Chemical Society.

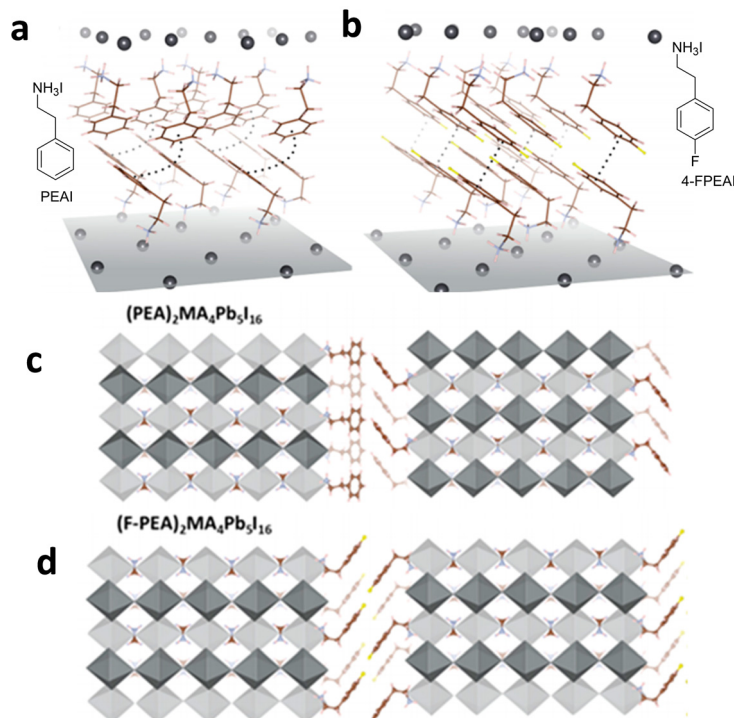


Fig. 7 (a and b) The crystal structure of  $(\text{PEA})_2\text{PbI}_4$  and  $(4\text{-FPEAI})_2\text{PbI}_4$ . (c and d) The schematic crystal structures of RP-perovskites  $(\text{PEA})_2\text{MA}_4\text{Pb}_5\text{I}_{16}$  and  $(4\text{FPEAI})_2\text{MA}_4\text{Pb}_5\text{I}_{16}$ .<sup>113</sup> Reproduced with permission from ref. 113. Copyright 2019, American Chemical Society.

under ambient conditions. The unencapsulated device of  $(4\text{-FPEAI})_2\text{MA}_4\text{Pb}_5\text{I}_{16}$  retained 65% of its initial PCE after heating at 70 °C for 576 h, whereas the PCE for the  $(\text{PEA})_2\text{MA}_4\text{Pb}_5\text{I}_{16}$ -based unencapsulated device dropped to 32% of its initial value when heated at 70 °C for a similar period of time. The overall performance and stability improvements for the  $(4\text{-FPEAI})_2\text{MA}_4\text{Pb}_5\text{I}_{16}$  based PV device were the result of higher out-of-plane carrier mobility, more ordered lattice growth, stronger interactions between the layers, reduced trap density and hydrophobicity imparted by the fluorine-tethered spacer cation.<sup>113</sup>

Coriolano and co-workers tested the photostability of single crystals of  $(\text{PEA})_2\text{PbI}_4$  vs.  $(4\text{-FPEAI})_2\text{PbI}_4$  under 488 nm laser irradiation for 30 min.<sup>81</sup> While the PL lifetime for the crystals of  $(\text{PEA})_2\text{PbI}_4$  was very short ( $\sim 4.6$  min) due to the photodegradation, more than 10-fold enhanced lifetime of  $\sim 66$  min was observed under similar laser irradiation conditions for the crystals of  $(4\text{-PEAI})_2\text{PbI}_4$ . It was also corroborated from the study that hydrophobicity and grain boundary passivation obtained from using a fluorinated spacer could impart more stability to photodegradation even under escalated humidity.<sup>81</sup>

Gao *et al.* studied the band structures of  $(\text{PEA})_2\text{PbI}_4$  vs.  $(4\text{-FPEAI})_2\text{PbI}_4$  using DFT calculations, where not many variations in the band structure were observed.<sup>57</sup> Contrary to this, substantial changes in the band structure of fluorinated spacer-based 2D-perovskite vs. non-fluorinated perovskite were reported by Grancini and co-workers,<sup>117</sup> where the structural distortion in the 2D-perovskite by the fluorine-tethered alkylammonium spacer was studied, and effects on the structural and optical properties were investigated. Here, the authors compared two low-dimensional perovskites, one with an aliphatic cation

$\text{C}_9\text{H}_{19}\text{NH}_3^+$  named Lc and the other with a partially fluorinated analogue  $\text{C}_9\text{H}_6\text{F}_{13}\text{NH}_3^+$  named Lf (*cf.* Fig. 8). The UV-Vis studies revealed a strong excitonic peak, a characteristic of 2D-perovskites. However, the excitonic peak in the UV-Vis spectrum was blue-shifted due to the fluorine substitution (*cf.* Fig. 8a). The Urbach energy (EU) was also larger for the perovskite including the fluorinated cation than the non-fluorinated analogue, which revealed larger distortion for the Lf-based perovskite. This increased structural distortion of the inorganic lattice widened the band gap. The exciton properties were also found to depend more upon the Pb–I–Pb angle between adjacent octahedra ( $\beta$ ) than the I–Pb–I bond angle within the metal-halide octahedra ( $\delta$ ). Fig. 8b shows the tilting of octahedra in terms of the angles  $\beta$  and  $\delta$ . Furthermore, higher was the structural distortion of the inorganic lattice due to the steric bulk of the fluorinated spacer cation, more was the increment in the band gap. This was probably caused by the difficulty in the overlap of atomic wavefunctions leading to the lowering of the valence and conduction band-widths.<sup>117</sup>

By increasing the thickness of the inorganic slab to  $n = 5$ , Shao *et al.* enhanced the PV performance of the 4-FPEAI-based RP-perovskite.<sup>60</sup> Here, the authors compared the PV performances of the  $n = 5$  RP-perovskite of 4-FPEAI with the PEAI-spacer. A high PCE of 17.3% with respect to 11% PCE for PEAI-based devices was shown in this study using 4-FPEAI.<sup>60</sup> Also, notable was the retention of high PCE even for a 1 cm<sup>2</sup> device of  $(4\text{-FPEAI})_2\text{MA}_4\text{Pb}_5\text{I}_{16}$ . The enhanced PV performance of  $(4\text{-FPEAI})_2\text{MA}_4\text{Pb}_5\text{I}_{16}$  compared to  $(\text{PEA})_2\text{MA}_4\text{Pb}_5\text{I}_{16}$  was attributed to the more preferred vertical lattice growth in the former, which has also been reported by Zheng *et al.* and will be

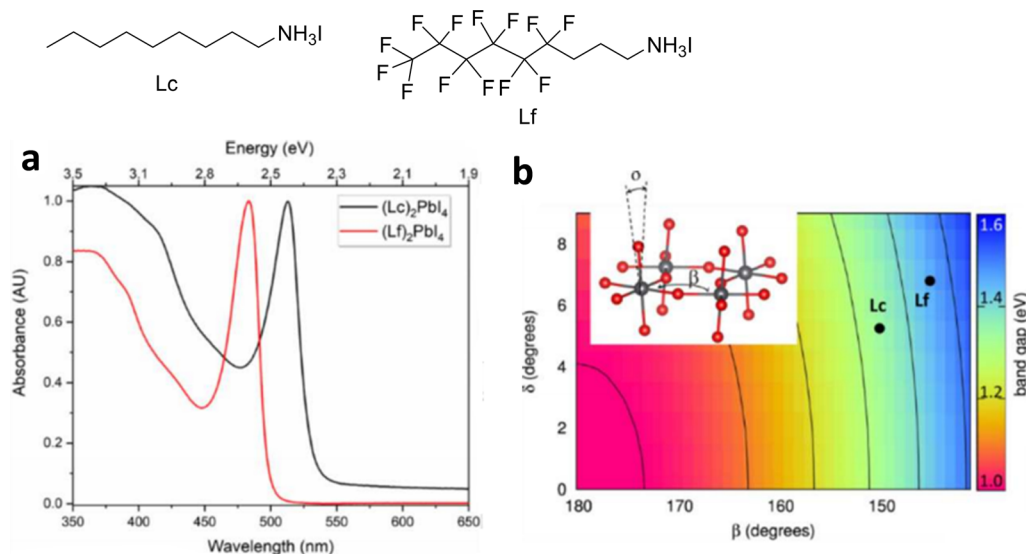


Fig. 8 (a) UV-Vis spectra of (Lc)<sub>2</sub>PbI<sub>4</sub> and (Lf)<sub>2</sub>PbI<sub>4</sub>. (b) Band gap map showing angles within and between the metal-halide octahedra.<sup>117</sup> Reproduced with permission from ref. 117. Copyright 2020, Frontiers Media S.A.

discussed later.<sup>101</sup> This preferential tailoring of crystal growth towards the vertical direction was confirmed from the increase in the intensity ratio for XRD peaks  $I_{(202)}/I_{(111)}$  for (4-FPEA)<sub>2</sub>MA<sub>4</sub>Pb<sub>5</sub>I<sub>16</sub> vs. (PEA)<sub>2</sub>MA<sub>4</sub>Pb<sub>5</sub>I<sub>16</sub> (*cf.* Fig. 9). It is to be noted that crystal growth along the (202) direction showed perfect vertical orientation, albeit growth along the (111) plane indicated inclined vertical alignment (*cf.* Fig. 9). Also, due to the influence of fluorine atoms, strong dipole-dipole interactions within the organic layer and hydrogen bonding interactions with the inorganic slabs offered smooth morphology with minimum grain boundaries for (4-FPEA)<sub>2</sub>MA<sub>4</sub>Pb<sub>5</sub>I<sub>16</sub> than (PEA)<sub>2</sub>MA<sub>4</sub>Pb<sub>5</sub>I<sub>16</sub>. Furthermore, an ordered gradient in the phase distribution with small *n*-phases dispersed towards the surface and higher *n*-phases towards the substrate was noted for (4-FPEA)<sub>2</sub>MA<sub>4</sub>Pb<sub>5</sub>I<sub>16</sub> than (PEA)<sub>2</sub>MA<sub>4</sub>Pb<sub>5</sub>I<sub>16</sub>, similar to another work discussed in this highlight.<sup>101</sup> Thus, a highly compact vertically oriented lattice with minimum grain boundaries or trap centres and more ordered phase distribution led to excellent carrier transport and cascade energy transfer across (4-FPEA)<sub>2</sub>MA<sub>4</sub>Pb<sub>5</sub>I<sub>16</sub>,

ultimately enhancing its PV performance compared to (PEA)<sub>2</sub>MA<sub>4</sub>Pb<sub>5</sub>I<sub>16</sub>. Also, higher dipole moment of fluorine favoured exciton segregation in (4-FPEA)<sub>2</sub>MA<sub>4</sub>Pb<sub>5</sub>I<sub>16</sub>.<sup>101</sup> The unencapsulated device of (4-FPEA)<sub>2</sub>MA<sub>4</sub>Pb<sub>5</sub>I<sub>16</sub> retained 93% of its initial PCE upon exposure to 55% RH for 500 h.<sup>101</sup> Under similar ageing conditions, a device of PEA lost 35% of its initial efficiency. Also, higher thermal stability could be seen for the device of (4-FPEA)<sub>2</sub>MA<sub>4</sub>Pb<sub>5</sub>I<sub>16</sub> due to several non-covalent interactions exerted by the fluorinated spacer cation within the perovskite lattice.<sup>60</sup>

You and co-workers studied the influence of fluorine substitution in the aryl ring (*o/m/p* or *2/3/4*) of the PEA cation on the macroscopic properties, like morphology, phase distribution, crystal growth orientation and PV performance, of the corresponding RP-perovskite (*n* = 4).<sup>50</sup> The best PV performance in the inverted device configuration was also achieved for the 4-FPEAI-based perovskite. Here UV-Vis studies confirmed the highest content of 3D-phases in 3-FPEAI- and 4-FPEAI-based RP-perovskites. However, entirely different vertical phase distributions were observed in this study than in another report by Zhang and co-workers discussed later.<sup>73</sup> The lower *n*-phases dominated toward the substrate side and higher *n*-phases dominated towards the surface for 3- or 4-FPEAI-based perovskites as corroborated from the results obtained from the front and back side excitations to obtain PL.<sup>50</sup> The heat triggered faster crystallization of smaller *n*-phases towards the glass side occurred due to the favourable formation energies of 3- or 4-FPEAI-based perovskites. Such a gradient of phase distribution supports cascade energy and charge transfer across the perovskite and improves the PV performance.<sup>50</sup> However, contrary to this, PL emission of 3D-phases dominated upon both front and back excitation of the 2-FPEAI-based perovskite film. This suggested the domination of 3D-phases towards both the front and back ends of the film and the presence of intermixed phases in the middle part of the film for the 2-FPEAI-based perovskite.

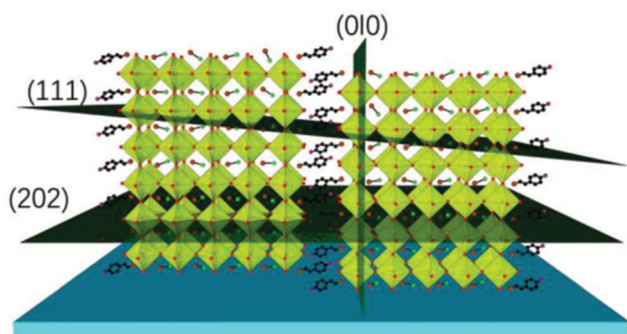


Fig. 9 Crystal growth along the (202) and (111) planes of (4-FPEA)<sub>2</sub>MA<sub>4</sub>Pb<sub>5</sub>I<sub>16</sub>.<sup>60</sup> Reproduced with permission from ref. 60. Copyright 2019, John Wiley and Sons.

## Highlight

The lower formation energy of the 2-FPEAI-based perovskite resulted in unorganized phase distribution and contributed towards carrier trapping, limiting PV performance. Further, highly oriented crystal growth for the 3- and 4-FPEAI-based perovskite was apparent from the grazing incidence wide-angle XRD (GIWAX) studies that imparted better carrier transport. In contrast to this, completely random crystal orientations were revealed from the GIWAX study of the 2-FPEAI-based perovskite, which lowered the carrier mobility in this case.<sup>50</sup> Nevertheless, highly noticeable differences were observed in the packing of the organic layers of  $(2/3/4\text{-FPEAI})_2\text{PbI}_4$  crystals, although the packing of the inorganic sheets was same in all the cases. The adjacent molecules in an organic sheet were fully aligned in the same direction in  $(4\text{-FPEAI})_2\text{PbI}_4$  (cf. Fig. 10a). However, an opposite orientation of organic molecules within a layer of  $(\text{-FPEAI})_2\text{PbI}_4$  led to a herringbone type of arrangement (cf. Fig. 10b). Similar facing direction for all molecules within one layer was confirmed for  $(2\text{-FPEAI})_2\text{PbI}_4$ , albeit the spacer molecules in the next layer were twisted by an angle of  $90^\circ$ , based on the crystal structure (cf. Fig. 10c). This orientational disorder of spacers within the organic bilayer may be the reason for the poor film quality of the 2-FPEAI-based perovskite. Notably, such differences in the packing of the organic bilayer resulted from the different degrees of dipole–dipole interactions rendered by the fluorine atoms present at different locations of 2/3/4-FPEAI-based spacers. Similarly, the formation energies obtained from DFT calculations followed the trend  $(2\text{-FPEAI})_2\text{PbI}_4 < (\text{PEAI})_2\text{PbI}_4 < (3\text{-FPEAI})_2\text{PbI}_4 < (4\text{-FPEAI})_2\text{PbI}_4$ . The highest formation energy of the 4-FPEAI-based perovskite may also offer minimal packing disorders within the organic layer rendering the highest PCE of  $\sim 10\%$  achieved for inverted planar device configuration, whereas the lowest PCE of  $\sim 1\%$  was observed for the device of the 2-FPEAI-based RP-type perovskite.<sup>50</sup> The very high formation energy can also account for the smooth morphology of the 4-FPEAI-based perovskite indicated from the SEM studies. Similarly, the poor morphology of the 2-FPEAI-based perovskite was the result of its low formation energy, which ultimately led to poor contact formation with other transport layers, lowering its PV performance.<sup>50</sup> The presence of a relatively high number of 2D-phases towards the

surface of the 3-FPEAI-based RP-perovskite could corroborate the highest stability seen for its unencapsulated PV device, when aged under 45% RH.<sup>50</sup> This study by You and co-workers well-presented property manoeuvring of perovskites with respect to the fluorine position in the spacer.<sup>50</sup>

Zhang and co-workers also studied the influence of fluorine substitution (*o/m/p* or 2/3/4) over the aryl ring of BA towards lattice orientation, formation energy and PV performance of the corresponding quasi 2D-perovskite ( $n = 5$ ).<sup>73</sup> Unlike another report,<sup>104</sup> the highest dipole moment (order 4-FBAI > 3-FBAI > 2-FBAI) and formation energy were observed for the 4-FBAI spacer followed by BA, 2-FBAI, or 3-FBAI spacers that led to the formation of perovskite films with superior morphology for 4-FBAI.<sup>73,123</sup> A well-known fact is that the higher is the dipole moment of the spacer cation, the smaller is the exciton binding energy and the better is the carrier segregation leading to better performance of the PV device, as observed for the 4-FBAI-based PV device.<sup>73</sup> Also, the highest formation energy of  $-3.52$  eV obtained from the DFT calculations suggested a more stable lattice for the 4-FBAI-based perovskite. The influence of the fluorinated spacer was the gradient growth of the perovskite lattice in the vertical direction with lower *n*-phases distributed at the top-side of the film and higher *n*-phases towards the bottom as seen for  $(2/3/4\text{-FBA})_2\text{MA}_4\text{Pb}_5\text{I}_{16}$ . This gradient growth of the lattice was confirmed by the XRD and PL studies. The PL emission obtained from the front excitation was of higher energy than that obtained from the bottom excitation confirming the gradient growth of the 4-FBAI-based perovskite. Interesting was the red-shifted PL emission of the fluorine-based perovskite, *i.e.*, 2/3/4-FBA, than the BA-based perovskite. Further, gradient growth was confirmed from the XPS studies. Particularly, the vertical orientation of lower *n*-phases not only offered better carrier mobility, but also led to higher absorbance in the range of 450–600 nm for  $(4\text{-FBA})_2\text{MA}_4\text{Pb}_5\text{I}_{16}$ .<sup>73</sup> This kind of gradient growth of different phases was effective in achieving greater defect passivation at the surface and improving the contact between the perovskite and the underlying HTM layer. However, lowering of solubility was observed upon introduction of fluorine onto the BAI spacer and the least solubility was reported for 2-FBAI in DMF

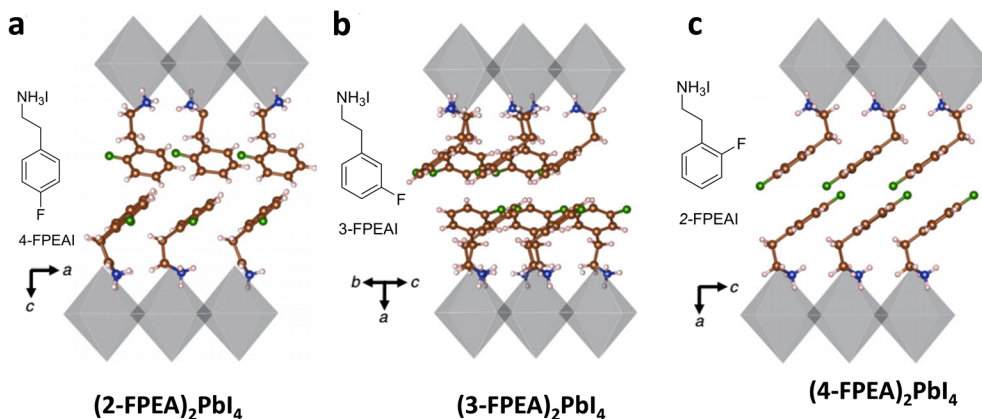


Fig. 10 (a) The crystal structure of  $(2\text{-FPEAI})_2\text{PbI}_4$ . (b) The crystal structure of  $(3\text{-FPEAI})_2\text{PbI}_4$ . (c) The crystal structure of  $(4\text{-FPEAI})_2\text{PbI}_4$ .<sup>50</sup> Reproduced with permission from ref. 50. Copyright 2019, Springer Nature.

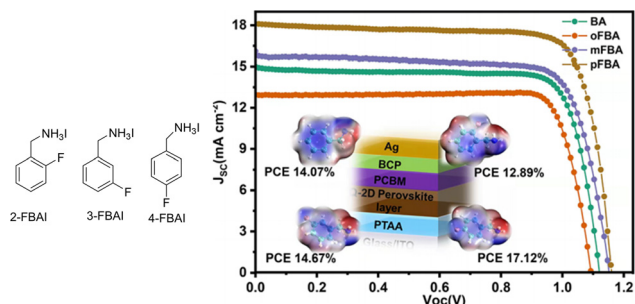


Fig. 11  $J$ - $V$  curve confirming the best performance for the (4-FBA)<sub>2</sub>-MA<sub>4</sub>Pb<sub>4</sub>I<sub>16</sub> PV device in an inverted configuration.<sup>73</sup> ESPs are shown in the inset (unit a.u.). Reproduced with permission from ref. 73. Copyright 2022, American Chemical Society.

leading to poor film quality. The highest PV performance of 17.12% with minimal hysteresis could be seen for (4-FBA)<sub>2</sub>MA<sub>4</sub>Pb<sub>4</sub>I<sub>16</sub> in an inverted device configuration (*cf.* Fig. 11).<sup>73</sup> The PCE obtained for BAI, 2-FBAI, and 3-FBAI devices was 14.07%, 12.89% and 14.67%, respectively. The better valence and conduction band alignment of (4-FBA)<sub>2</sub>MA<sub>4</sub>Pb<sub>5</sub>I<sub>16</sub> with adjacent hole-transport and electron-transport layers also facilitated carrier extraction and transport leading to the highest performance of (4-FBA)<sub>2</sub>MA<sub>4</sub>Pb<sub>4</sub>I<sub>16</sub>, when applied in the PV devices. At the same time, the lowest trap density was measured from the space charge limited current (SCLC) method for (4-FBA)<sub>2</sub>MA<sub>4</sub>Pb<sub>4</sub>I<sub>16</sub> compared to perovskites based on other isomeric spacers, that played a role in PV performance. Furthermore, the highest stability was also seen for the (4-FBA)<sub>2</sub>MA<sub>4</sub>Pb<sub>4</sub>I<sub>16</sub> device, which could retain PCE after 2000 h post storage in an Ar-filled glovebox.<sup>73</sup> The highest water contact angle of 66.1° was measured for the film of 4-FBAI and the order of water contact angle along the series was as follows: 4-FBAI > 3-FBAI > 2-FBAI > BAI.<sup>73</sup> The study confirmed that the best PV performance and stability could be achieved by fluorine substitution at the *para*-position of the BAI-spacer.

The influence of different electronegative halogen atoms at the *para*-position of the PEA cation, *i.e.*, the effects of 4-FPEAI, 4-CIPEAI and 4-BrPEAI, on the optoelectronic properties of RP-type perovskite (4-F/4-Cl/4-BrPEA)<sub>2</sub>MA<sub>2</sub>Pb<sub>3</sub>I<sub>10</sub> was investigated by Wang *et al.*<sup>61</sup> A lower exciton binding energy compared to the PEA-based perovskite was extracted from the temperature-dependent PL studies of these halogen substituted PEA-based perovskites. Due to the polar structure, the halogen substituted PEA spacer offered lower quantum confinement in the corresponding perovskite. The exciton binding energies were found to follow the trend 4-FPEAI < 4-CIPEAI < 4-BrPEAI (*cf.* Fig. 11). DFT studies also showed a decrease in the HOMO and an increase in the LUMO energies with respect to the vacuum level along the perovskite series including a spacer: PEAI < 4-FPEAI < 4-CIPEAI < 4-BrPEAI. The ultimate effect was the narrowing of the band gaps along the series, which was confirmed from the UV-Vis studies (*cf.* Fig. 12). Also the dipole moments of 4-FPEA<sup>+</sup>, 4-BrPEA<sup>+</sup>, 4-CIPEA<sup>+</sup> and PEA<sup>+</sup> were calculated using DFT, and higher dipole moments of X-PEA<sup>+</sup> (F, Cl, Br) than PEA<sup>+</sup> were observed, which was attributed to the electron-withdrawing halogen atoms (F, Cl, Br).<sup>61</sup> Besides, the calculated

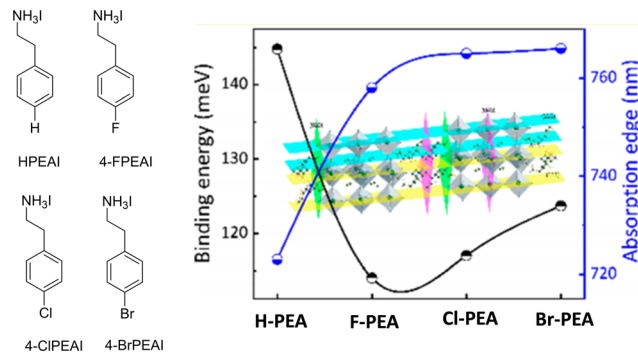


Fig. 12 The trend of binding energy and absorption edge across the series of RP-perovskites with PEA and different halogen-tethered PEA spacers.<sup>61</sup> Reproduced with permission from ref. 61. Copyright 2019, American Chemical Society.

dipole moment values were ~13.16 D for 4-FPEAI, ~13.49 D for 4-CIPEAI, and ~13.34 D for 4-BrPEAI. This higher dipole moment facilitated carrier dissociation and reduced the exciton binding energy of the corresponding perovskite. The films of (H/4-F/4-Cl/4-BrPEA)<sub>2</sub>MA<sub>2</sub>Pb<sub>3</sub>I<sub>10</sub> ( $x = \text{H, F, Cl, Br}$ ) were fabricated by a one-step spin coating method. Also, the influences of 4-FPEAI to enhance the crystallinity and out-of-plane growth of the perovskite lattice with respect to the substrate were studied from the XRD. This ordered out-of-plane growth of the perovskite lattice followed the trend PEAI ~ 4-FPEAI > 4-CIPEAI > 4-BrPEAI and was confirmed from the presence or absence of (0 $k$ 0) reflection as well as the strength of (111) and (222) reflections seen in the XRD profile. In the case of chloride- and bromide-tethered PEA cations, diffraction corresponding to (0 $k$ 0) was seen. However, (0 $k$ 0) reflections were rarely present and strong reflections corresponding to (111) and (222) planes were conspicuous in the RP-perovskites of PEA and 4-FPEA cations, suggesting highly oriented out-of-plane crystal growth. It was surmised that a strong hydrogen bond between highly electronegative fluorine and hydrogen atoms of the aromatic ring offered this oriented lattice growth. Also, much higher intensity obtained from the reflection of the (111) plane with respect to the (020) plane for the 4-FPEA-based perovskite than the PEA-based perovskite corroborated the more oriented out-of-plane lattice growth in the former. Furthermore, out-of-plane lattice growth decreased from 4-FPEA to 4-CIPEA to 4-BrPEA due to the increase in the atomic radii of the halogen across the series. The SEM images of all these RP-perovskites suggested smooth homogeneous coverage.<sup>61</sup> The Pb-I-Pb angle ( $\alpha$ ) (outside the Pb-X octahedron) of 4-F/4-Cl/4-BrPEA<sub>2</sub>PbI<sub>4</sub> was studied using single crystal XRD. From the study,  $\alpha$  angles for (PEA)<sub>2</sub>PbI<sub>4</sub>, (4-FPEA)<sub>2</sub>PbI<sub>4</sub>, (4-CIPEA)<sub>2</sub>PbI<sub>4</sub> and (4-BrPEA)<sub>2</sub>PbI<sub>4</sub> were 151.3°, 152.9°, 153.6° and 152.6°, respectively. The higher was this Pb-I-Pb angle, the lesser was the effect of the organic cation on metal-halide lattice distortion. Also, significant interactions and shorter distance between the ammonium group and aromatic carbon bonded to the ethylammonium linker of (4-FPEA)<sub>2</sub>PbI<sub>4</sub> suggested the strong electronic influence of fluorine. The longer component of the PL lifetime of RP-perovskites of PEAI, 4-BrPEAI, 4-CIPEAI, and 4-FPEAI was 31.60 ns, 43.58 ns,

## Highlight

50.12 ns, and 72 ns, respectively, which also indicated a decrease in the binding energy of the RP-perovskites in the following order: PEA > 4-BrPEAI > 4-ClPEAI > 4-FPEAI. The highest hole and electron mobilities were obtained for the 4-FPEAI-based RP-perovskite than the PEAI-based analogue. The best-verified PCE of 5.83% was obtained for the 4-FPEAI-based RP-perovskite PV device, which was 90% higher than that of the PEAI-based device. Also, the better PV performance of the 4-FPEAI-based RP-perovskite than other 4-BrPEAI or 4-ClPEAI-based RP-perovskites correlated with the most ordered out-of-plane lattice growth and lowest exciton binding energy among the series. Finally, the study demonstrated an effective stereoelectronic approach to integrate desirable optoelectronic properties into perovskites by rational tethering of a suitable electronegative atom of appropriate atomic size onto a spacer cation.<sup>61</sup>

For RP-perovskites with  $n \leq 5$ , it is furthermore crucial to obtain out-of-plane lattice growth to avoid impeding carrier transport due to the effect of the insulating spacer cation.<sup>60</sup> Zheng *et al.* demonstrated manoeuvring of vertical lattice growth by fluorine substitution at the *para*-position of the PEAI cation, which enhanced carrier transport in the out-of-plane direction for the  $n = 4$  RP-perovskite.<sup>61,101</sup> Also, the highest crystallinity, grain size and superior film morphology were observed for  $(4\text{-FPEA})_2\text{MA}_3\text{Pb}_4\text{I}_{13}$  than  $(\text{H}/4\text{-Br}/4\text{-ClPEA})_2\text{MA}_3\text{-Pb}_4\text{I}_{13}$ . Besides, the ordered distribution of different  $n$ -phases was also noted for  $(4\text{-FPEA})_2\text{MA}_3\text{Pb}_4\text{I}_{13}$ . The vertically oriented crystal growth and ordered phase distribution improved charge transport in the out-of-plane direction, ultimately offering a higher PCE of 18.10% for the inverted PV device of  $(4\text{-FPEA})_2\text{-MA}_3\text{Pb}_4\text{I}_{13}$  compared to 12.23% for  $(\text{PEA})_2\text{MA}_3\text{Pb}_4\text{I}_{13}$ , 7.93% for  $(4\text{-ClPEA})_2\text{MA}_3\text{Pb}_4\text{I}_{13}$  and 6.08% for  $(4\text{-BrPEA})_2\text{MA}_3\text{Pb}_4\text{I}_{13}$ . A minimum hysteresis was also seen for the device of  $(4\text{-FPEA})_2\text{-MA}_3\text{Pb}_4\text{I}_{13}$  reflecting minimal carrier trapping. Furthermore, a significant improvement in the PCE was noted compared to the previous report by Wang *et al.*<sup>61</sup> Transient absorption (TA) studies suggested a preferential vertical orientation of the lattice for  $(4\text{-FPEA})_2\text{MA}_3\text{Pb}_4\text{I}_{13}$  due to the elimination of  $n = 1$  phases. This elimination of  $n = 1$  phases hindered in-plane growth and allowed more growth in the vertical direction for  $(4\text{-FPEA})_2\text{MA}_3\text{Pb}_4\text{I}_{13}$ . Contrarily, random lattice orientations for  $(4\text{-Cl}/4\text{-BrPEA})_2\text{MA}_3\text{Pb}_4\text{I}_{13}$  and in-plane growth for  $(\text{PEA})_2\text{-MA}_3\text{Pb}_4\text{I}_{13}$  were noticed, hindering charge transport and lowering PV performance relative to  $(4\text{-FPEA})_2\text{MA}_3\text{Pb}_4\text{I}_{13}$ . An enhancement in the interlayer distance of inorganic sheets upon halogen substitutions was also observed for  $(4\text{-F}/4\text{-Cl}/4\text{-Br-PEA})_2\text{PbI}_4$  compared to  $(\text{PEA})_2\text{PbI}_4$ . The increase in the interlayer distance of the inorganic sheet followed the trend  $(4\text{-FPEA})_2\text{PbI}_4 < (4\text{-ClPEA})_2\text{PbI}_4 < (4\text{-BrPEA})_2\text{PbI}_4$  and was according to the increase in the atomic radii of halogen atoms. Nevertheless, different DFT-based dipole moment trends of these spacer cations compared to a previous report were noted in this study, which were 13.3 D for PEAI, 16.7 D for 4-FPEAI, 19.0 D for 4-ClPEAI, and 22.1 D for 4-BrPEAI.<sup>61</sup> Besides, a gradient vertical distribution of different  $n$ -phases could be seen for  $(\text{H}/4\text{-FPEA})_2\text{MA}_3\text{Pb}_4\text{I}_{13}$ , with smaller  $n$ -phases located more towards the bottom and higher  $n$ -phases concentrated

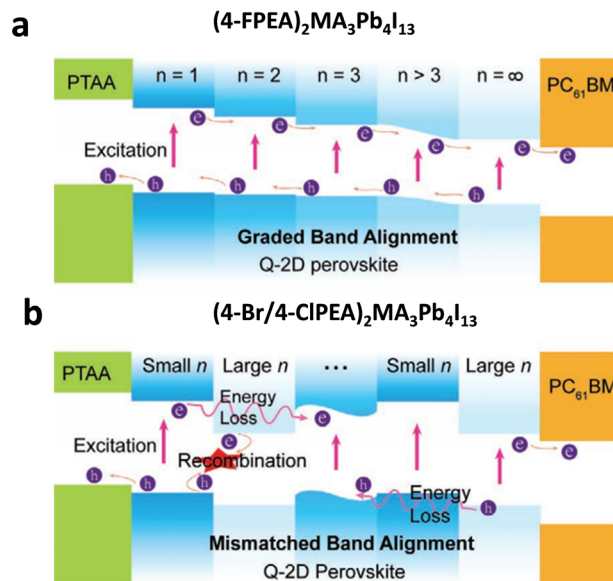


Fig. 13 (a) Suitable band alignment due to gradient phase distribution in  $(4\text{-FPEA})_2\text{MA}_3\text{Pb}_4\text{I}_{13}$ . (b) Carrier trapping due to random phase distribution in  $(4\text{-Br}/4\text{-ClPEA})_2\text{MA}_3\text{Pb}_4\text{I}_{13}$ .<sup>101</sup> Reproduced with permission from ref. 101. Copyright 2020, John Wiley and Sons.

towards the surface of the film. Such oriented phase distribution enhanced carrier extraction and boosted PV performance for  $(4\text{-FPEA})_2\text{MA}_3\text{Pb}_4\text{I}_{13}$  (*cf.* Fig. 13a). Also, with the increase in the annealing time, more growth of smaller  $n$ -phases beneath the higher  $n$ -phases was correlated from the enhancement of absorption peaks for  $n = 2, 3$  phases of  $(4\text{-FPEA})_2\text{MA}_3\text{Pb}_4\text{I}_{13}$ . In contrast, completely random phase distribution without any gradient was confirmed for  $(4\text{-Br}/4\text{-ClPEA})_2\text{MA}_3\text{Pb}_4\text{I}_{13}$ , which led to carrier trapping and lowered PV performance (*cf.* Fig. 13b). For  $(4\text{-Br}/4\text{-ClPEA})_2\text{MA}_3\text{Pb}_4\text{I}_{13}$  an increase in the annealing time offered enhancement in the peak intensity of both smaller and higher  $n$ -phases, suggesting randomness in the phase orientation. These varied orders of phase distribution could be correlated with the different dipole moments of the halogenated spacer cation. As the dipole moment increased with an increase in the atomic size of the spacer cation ( $4\text{-FPEAI} < 4\text{-ClPEAI} < 4\text{-BrPEAI}$ ), the solubility of the spacer cation decreased. This reduced solubility of the spacer cation led to the crystallization of smaller  $n$ -phases upon annealing of  $(4\text{-Br}/4\text{-ClPEA})_2\text{MA}_3\text{Pb}_4\text{I}_{13}$ . However, for  $(4\text{-FPEA})_2\text{MA}_3\text{Pb}_4\text{I}_{13}$ , higher  $n$ -phases rich in MA crystallized first and smaller  $n$ -phases rich in the spacer crystallized at the end due to the enhanced solubility, leading to a gradient phase distribution. Further, this kind of ordered phase distribution favoured cascade transport of holes from higher  $n$ -phases to lower  $n$ -phases and electrons from lower  $n$ -phases to higher  $n$ -phases across  $(4\text{-FPEA})_2\text{MA}_3\text{Pb}_4\text{I}_{13}$ . Additionally, the highest electron extraction efficiency of 48% and reduced carrier trapping due to the appropriate band gap alignment were seen for  $(4\text{-FPEA})_2\text{MA}_3\text{Pb}_4\text{I}_{13}$  (*cf.* Fig. 13a). Nevertheless, the random phase distribution of  $(4\text{-Br}/4\text{-ClPEA})_2\text{MA}_3\text{Pb}_4\text{I}_{13}$  prevented cascade carrier transport and higher  $n$ -phases distributed randomly

in between the layers acting as the trap sites for holes and electrons. The out-of-plane lattice growth and gradient phase distribution rendered by the influence of the fluorine atom in the 4-FPEAI spacer ultimately offered an excellent PCE of 18.10% for the device of  $(4\text{-FPEAI})_2\text{MA}_3\text{Pb}_4\text{I}_{13}$ . The highest stability with the retention of 90% of initial PCE was observed for the  $(4\text{-FPEAI})_2\text{MA}_3\text{Pb}_4\text{I}_{13}$ -based device upon storage at 40–50% RH for 1 month, due to the hydrophobicity imparted by the fluorine atom. However, the PCE of the control 3D-perovskite dropped to 30% of its initial value under similar ageing conditions. Higher stability than the PEAI-based device was also confirmed for the devices of  $(4\text{-Br}/4\text{-ClPEAI})_2\text{MA}_3\text{Pb}_4\text{I}_{13}$  upon storage at 40–50% RH for 1 month. Similarly, higher thermal stability than the control device of the 3D-perovskite was noted for the devices of  $(4\text{-F}/4\text{-Br}/4\text{-Cl-PEAI})_2\text{MA}_3\text{Pb}_4\text{I}_{13}$  upon heating at 80 °C inside a glovebox, with the retention of 80% of initial PCE after 1 month for the  $(4\text{-FPEAI})_2\text{MA}_3\text{Pb}_4\text{I}_{13}$ -based device, which is the highest among the series.<sup>101</sup>

Jen and co-workers compared and tailored the intrinsic properties of the  $n = 5$  RP-perovskite by using 4-FPEAI, 4-OMePEAI and PEAI-based spacers.<sup>64</sup> A highest PCE of 14.5% was achieved for the 4-FPEAI-based inverted PV device. This superior PV performance was an attribute of the best hole and electron mobility as measured for the 4-FPEAI-based perovskite in this study. The optical band gaps were according to the order  $\text{PEAI} > 4\text{-FPEAI} > 4\text{-OMePEAI}$ . PL studies confirmed higher  $n$ -phases for 4-FPEAI than the PEAI-based RP perovskite which probably lowered its band gap. Ultraviolet photoelectron spectroscopy (UPS) determined HOMO/LUMO energies were deeper for the 4-FPEAI-based RP-perovskite compared to the others due to the different dipolar effects of the spacers 4-FPEAI and 4-OMePEAI. The interlayer spacing of these perovskites followed the order  $4\text{-OMePEAI} > 4\text{-FPEAI} > \text{PEAI}$ , and was according to the decrease in the spacer size.<sup>64</sup> The larger size of 4-OMePEAI also lowered crystallinity compared to the 4-FPEAI-based perovskite due to the greater lattice distortion in the former. This might be the reason for the lower PV performance of 4-OMePEAI than the 4-FPEAI-based perovskite. Computation studies were also carried out by the authors to reveal the water-repellent properties of these perovskites. When the spacer was 4-OMePEAI, water molecules were repelled away from the perovskite surface due to the steric hindrance between the oxygen atom of the spacer and water molecules; repulsion was also observed between the lone pairs of spacer oxygen and water molecules below a critical interacting distance, which escalated the repulsive interaction, inhibiting water attack. In the case of 4-FPEAI, the water-phobicity was mainly attributed to the lone pair–lone pair repulsion between the fluorine atom of the spacer and the oxygen atom of the water molecule and was not influenced by any other steric factors.<sup>64</sup> The overall effect of such repulsive interactions was an increase in the binding energy towards water, below a critical distance from the surface of the perovskite (*cf.* Fig. 14).<sup>64</sup> The outcome of these repulsive interactions between perovskite and water molecules was the retention of 90% of PCE for the encapsulated devices of 4-FPEAI upon exposure to 40–50% RH for 40 days.

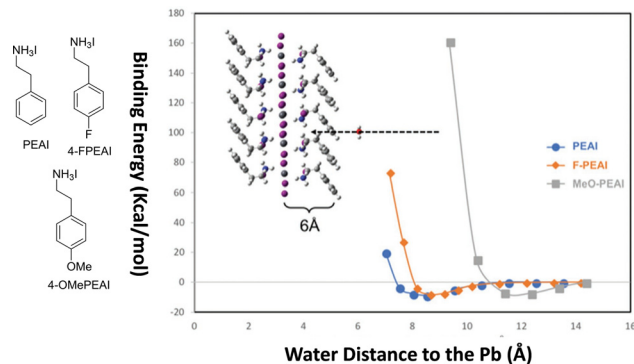


Fig. 14 Plots for theoretically calculated binding energy vs. water distance from the Pb layer for the RP-perovskites based on PEAI, 4-FPEAI, and 4-OMePEAI spacers.<sup>64</sup> Reproduced with permission from ref. 64. Copyright 2019, John Wiley and Sons.

Similarly, high photostability with retention of 97% PCE was revealed for the 4-FPEAI-based device under AM 1.5G illumination for 3 h.<sup>64</sup>

Aryl-perfluoroaryl quadrupole forces between PEA and pentafluorophenylethyl ammonium spacer ( $\text{F}_5\text{PEA}$ ) were exploited by You *et al.* to enhance the interaction within the organic sheet of RP-perovskites.<sup>62</sup> The inorganic layer thickness chosen for the study was  $n = 4$ . The UV-Vis and PL spectra revealed the presence of mixed dimensional phases with  $n = 1, 2, 3, 4$  upon 25–75% replacement of PEA with  $\text{F}_5\text{PEA}$  (*cf.* Fig. 15b and c). Also, the highest PL intensity for the 3D-phase upon front excitation suggested a vertical distribution of phases of different dimensions (*cf.* Fig. 15c). However, no phase segregation of PEA and  $\text{F}_5\text{PEA}$ -rich domains was traced in the study. 50% replacement of PEA with  $\text{F}_5\text{PEA}$  (1:1 PEA: $\text{F}_5\text{PEA}$ ) led to a maximum PV efficiency of 10.24% in an inverted configuration, whereas the devices with PEA ( $n = 4$ ) offered a lower PCE of 7.64%. Also, the unencapsulated devices of 50%  $\text{F}_5\text{PEA}$  offered the best stability with retention of 80% of initial PCE, post 30 days of exposure to 45% RH. A notable recovery of 92% of initial PCE after deposition

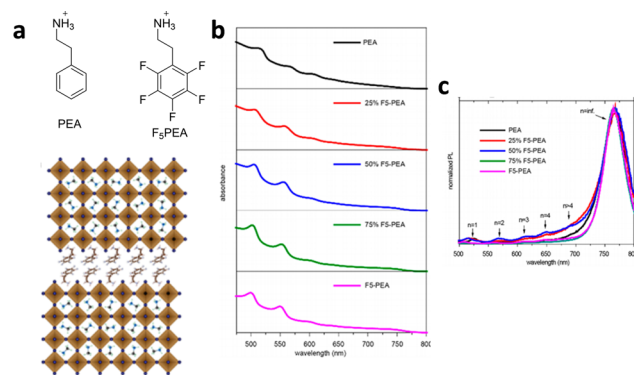


Fig. 15 (a) RP-perovskite with 1:1 PEA :  $\text{F}_5\text{PEA}$  cations. (b) UV-Vis and PL spectra reveal the presence of mixed-dimensional phases with  $n = 1, 2, 3, 4$ , etc. upon 25–75% replacement of PEA with the  $\text{F}_5\text{PEA}$ -based spacer. (c) PL spectrum obtained from the front excitation revealing the highest intensity of the 3D-phase.<sup>62</sup> Reproduced with permission from ref. 62. Copyright 2019, American Chemical Society.



## Highlight

of the fresh electrode was feasible for a 1:1 PEA:F<sub>5</sub>PEA-based device. Nevertheless, such a recovery could not be achieved for the PEA-based RP-perovskite. Interestingly, 75% replacement of PEA with F<sub>5</sub>PEA led to a lowering of PV performance. This indicated that the hydrophobicity of the fluorinated cation was not the sole factor conferring device stability and efficiency improvement as observed during the study. The GIWAX studies indicated a more random crystal orientation for the films with 75% or higher concentration of the F<sub>5</sub>PEA cation. This suggested that aryl-perfluoroaryl quadrupole interactions were highest for 1:1 PEA:F<sub>5</sub>PEA films and might be the major contributing factor towards higher efficiency and stability. Also, a smooth pinhole-free film with bigger grain sizes was seen in SEM images of 50% F<sub>5</sub>PEA-based perovskite films that led to better interfacial contacts with various transport layers in the PV devices, further improving the performance. The higher enthalpy of transition as obtained from the DSC study of the 1:1 PEA:F<sub>5</sub>PEA-based 2D-perovskite than the perovskite of individual spacers also confirmed strong aryl-perfluoroaryl quadrupole forces within the organic sheet.<sup>62</sup>

Liu and co-workers explored amidinium-anchored spacers benzamidine (PhFA) and 4-fluorobenzamidine (4-FPhFA) to develop RP-perovskites ( $n = 5$ ) for PV applications.<sup>59</sup> The objective of the study was to investigate the way a fluorine substitution at the *para* position of the spacer tailored the properties of RP-perovskites compared to a non-fluorinated amidinium spacer. A similar comparative study with PhFA and 4-FPhFA in the realm of bilayer perovskites was also reported and will be discussed later.<sup>63</sup> A higher PCE of 17.37% was reported for 4-FPhFA compared to 12.92% for PhFA-based inverted planar devices.<sup>59</sup> This PCE of 17.37% obtained for the 4-FPhFA-based RP-perovskite is the best conversion efficiency known so far for any amidinium-based spacer to the best of our information. The higher dipole moment of 3.53 D for 4-FPhFA than 3.03 D (calculated) for PhFA not only limited the quantum confinement, but also led to lower exciton binding energy for the 4-FPhFA-based RP-perovskite, improving the segregation of photogenerated carriers as observed in the study. A stronger hydrogen bonding interaction between the 4-FPhFA spacer and the inorganic slab was confirmed from the higher binding energies for Pb (4f) and I (3d) compared to the same peaks in the PhFA-based perovskite, as revealed from the XPS. This kind of stronger non-covalent interactions not only led to a superior film with a larger grain size but also imparted higher stability to the 4-FPhFA-based perovskite film. Also, vertical lattice growth was confirmed from the SEM studies of the 4-FPhFA-based RP-perovskite film, which led to a greater out-of-plane carrier mobility. Contrary to this, both parallel and vertical lattice growths were noted from the SEM studies of the PhFA-based perovskite, significantly restricting carrier mobility across the layers.<sup>59</sup> The higher ratio of  $I_{(202)}/I_{(111)}$  XRD peaks obtained for the 4-FPhFA-based RP-perovskite than the PhFA-based perovskite also confirmed more perfect vertical lattice alignment in the former. Similarly, higher crystallinity and out-of-plane growth for the 4-FPhFA-based RP-perovskite than the non-fluorinated one were also indicated from the sharper Bragg diffractions for (111) and (202) planes. Significant reduction in non-radiative recombination was confirmed from the higher PL intensity and lifetime



Fig. 16 The energy level diagrams for PhFA and 4-FPhFA-based perovskites, illustrating greater n-type character for the latter.<sup>59</sup> Reproduced with permission from ref. 59. Copyright 2021, American Chemical Society.

for the 4-FPhFA-based perovskite. A lower trap density and higher carrier concentration were confirmed from the time-resolved confocal fluorescence microscopy studies (TCFM) of 4-FPhFA and PhFA-based RP-perovskites. Here also, ordered phase distributions with small  $n$ -phases towards the bottom and high  $n$ -phases at the top of the film were seen for both PhFA and 4-FPhFA-based RP-perovskites, which facilitated cascade hole and electron transports across the perovskites (*cf.* Fig. 16). UPS was used in this study to explore the valence and conduction band energies of the perovskites. A deeper conduction band energy of  $-4.25$  eV for the 4-FPhFA-based perovskite than  $-3.91$  eV for the PhFA-based perovskite corroborated greater n-type character for the 4-FPhFA-based perovskite, which allowed the filling of electronic traps at the surface of the film (*cf.* Fig. 14). Also, a higher surface potential due to the electron-trap filling in the 4-FPhFA-based perovskite than the other one was confirmed from the Kelvin probe force microscopic (KPFM) studies. The retention of 82% of initial PCE than 77% and 59% for PhFA and control 3D-perovskites, respectively, upon continuous illumination using a  $100 \text{ mW cm}^{-2}$  white LED lamp for 200 h suggested enhanced photostability. Similarly, a higher shelf-life with retention of 99% PCE was noted for the unencapsulated devices of 4-FPhFA upon storage inside a glovebox for 3000 h.<sup>59</sup>

Zhou *et al.* explored a combination of 2,2,2-trifluoroethylammonium iodide (F<sub>3</sub>EAI) with *n*-butylammonium iodide (BuAI)-based aliphatic spacers to develop RP-type perovskite  $[(\text{BuAI})_{1-x}(\text{F}_3\text{EA})_x]_2\text{MA}_3\text{Pb}_4\text{I}_{13}$ , with  $x \leq 0.1$ .<sup>124</sup> Subsequently, doping of F<sub>3</sub>EAI into the organic sheets limited the quantum confinement due to the dipolar effect of the electronegative fluorine atom. The polar fluorine atom enhanced the dielectric constant of the organic sheet due to localized polarization, limiting the dielectric differences between the organic and inorganic layers that led to a weaker coulombic interaction between the holes and electrons (*cf.* Fig. 17). This effectively lowered the exciton binding energy to 147 meV for 6% doping with respect to 128 meV for control. The lower binding energy also facilitated the segregation of photogenerated carriers in the PV device. The ultimate outcome of using this mixed spacer combination as an absorber in an inverted planar PV device was a high PCE of 12.51% for 6% doping. Nearly 0–10% doping of F<sub>3</sub>EAI into the organic layer of the BuAI-based RP perovskite could not alter the lattice phase and



Fig. 17 The lattice polarization imparted by the  $F_3EAI$  spacer offering exciton screening and lower binding energy.<sup>124</sup> Reproduced with permission from ref. 124. Copyright 2018, John Wiley and Sons.

was confirmed from the XRD studies. However, a slight reduction in bandgap was noted upon an increase in the concentration of  $F_3EAI$  from 0 to 10%. Also, the superior film quality could be seen upon introducing 0–10%  $F_3EAI$  to develop the RP-perovskite; however, beyond this limit pinholes started appearing in the film. An enhancement in the PL intensity and lifetime for the 6%  $F_3EAI$ -doped RP perovskite compared to the reference suggested a significant reduction in the trap-assisted non-radiative recombination. The longer photovoltage decay time for the 6%  $F_3EAI$ -doped RP-perovskite than the reference sample also confirmed slower and more effective carrier recombination and transport. Since the doping percentage of  $F_3EAI$  was low ( $\sim$ 0–10%), it could not impact the stability of the perovskite extensively, as observed in the study.<sup>124</sup>

#### 4. Fluorine-based spacers for quasi 2D DJ-perovskites

The effects of a fluorinated spacer upon the PV performance of a DJ-perovskite were investigated by Yin and co-workers. To the best of our knowledge, this is the only report of a DJ-perovskite based on a fluorinated spacer and the present section covers this. Here, the  $n = 4$  DJ-perovskite offered a PCE of 16.62%, the highest value known so far for any DJ-perovskites with an aromatic spacer. The fluorinated spacer chosen in this study to assemble into a DJ-type perovskite was 2,3,5,6-tetrafluoro-1,4-phenylenedimethan ammonium iodide ( $F_4PhDMAI$ ).<sup>65</sup> Noncovalent  $CH \cdots F$  hydrogen bonding interactions between adjacent spacers and electrostatic  $F \cdots I$  interactions between the spacer and the inorganic lattice led to a higher dissociation energy of 7.32 eV for DJ-perovskite ( $F_4PhDMAI$ )(MA)<sub>3</sub>Pb<sub>4</sub>I<sub>13</sub> (cf. Fig. 18). Also, intramolecular  $CH \cdots F$  interactions in the crystal structure of the  $F_4PhDMAI$ -based DJ-perovskite were revealed. These interactions offered higher stability to the  $F_4PhDMAI$ -based DJ-perovskite than the  $PhDMAI$ -based DJ-perovskite towards disintegration by moisture, light and temperature. Also, these different noncovalent interactions reduced the distance between the inorganic sheets of the  $F_4$ - $PhDMAI$ -based perovskite



Fig. 18 The crystal structure of ( $F_4$ - $PhDMAI$ ) $PbI_4$ , showing different non-covalent interactions.<sup>65</sup> Reproduced with permission from ref. 65. Copyright 2021, American Chemical Society.

enhancing carrier mobility. The shorter  $I \cdots I$  distance of 6.39 Å between the inorganic layers of the  $F_4$ - $PhDMAI$ -based perovskite than 6.75 Å for the  $PhDMAI$ -based perovskite was calculated from DFT, further suggesting closer interlayer stacking and stronger interactions in the former perovskite. A higher content of lower  $n$ -phases towards the surface of the  $F_4PhDMAI$ -based perovskite than  $PhDMAI$  affected greater passivation of electronic traps and led to higher environmental stability as well as shallower conduction band energy. However, the content of lower  $n$ -phases was more towards the substrate for the  $PhDMAI$ -based perovskite and was established from the PL studies from the front and back side excitations. The vertical growth of crystals with minimal grain boundaries was confirmed from the SEM and XRD studies for the  $F_4$ - $PhDMAI$ -based perovskite film, which contributed towards greater out-of-plane carrier mobility. However, GIWAX studies indicated random crystallite orientation in the  $PhDMAI$ -based perovskite film. These results showed that fluorination of the  $PhDMAI$  cation could indeed influence the orientation of lattice growth in the corresponding perovskite. The greater passivation of trap density and reduction in non-radiative recombination were also indicated from the enhancement in the PL intensity and PL lifetime for the  $F_4PhDMAI$ -based perovskite.<sup>65</sup> Also were confirmed higher electron mobility and lower trap density for the  $F_4PhDMAI$ -based perovskite than  $PhDMAI$  using the SCLC method. Improved hydrophobicity was revealed from the higher water contact angle of 82.03° for the  $F_4PhDMAI$ -based perovskite film than 60.75° obtained for the  $PhDMAI$ -based perovskite film.<sup>65</sup> Similarly, illumination with a 100 mW  $cm^{-2}$  white-LED light and also the ageing test at 80 °C confirmed higher photostability as well as thermal stability for  $F_4PhDMAI$  than the  $PhDMAI$ -based perovskite device.<sup>65</sup>

#### 5. Fluorine-based spacers for 2D/3D-bilayer perovskites

As discussed at the outset, the 2D/3D-bilayer perovskite can retain the superior carrier mobility and absorption property of a higher dimensional counterpart, at the same time retaining the stability of the lower dimensional capping layer.<sup>57</sup> In the case of the bilayer perovskite, bulky spacer cations are present as a

## Highlight

passivating upper coating over the 3D-perovskite or are located mostly around the  $\text{PbI}_2$ -rich grain boundaries, leading to the passivation of defects at the surface or grain boundaries.<sup>35</sup> In this regard, the exploration of fluorinated spacer cations as a passivator to offer enhanced hydrophobicity to 2D/3D-bilayer perovskites seems obvious. This section covers the studies pertaining to the exploration of fluorinated spacers to develop 2D/3D-bilayer perovskites. The section first collates studies of the 4-FPEAI-based spacer to develop bilayer perovskites of diverse compositions for PV applications. Then are presented discussions showcasing the way the position of fluorine substitution on the aromatic spacer could impact photophysical properties and PCE. After this are organized discussions on multi-fluorinated aromatic spacers to manoeuvre PV performance. The studies with fluorinated amidinium-type spacers followed by aliphatic spacers to develop bilayer perovskites are discussed towards the end.

Gao and co-workers explored fluorinated aromatic spacers, like 4-FPEAI, to develop stacked 2D/3D-bilayer perovskites with improved PV performance and stability compared to 3D-perovskites.<sup>57</sup> The improved PCE and stability were due to the passivating effect of the fluorinated cation, which not only lowered non-radiative recombination but also imparted hydrophobicity to the perovskite and protected against moisture and other external factors.<sup>57</sup> Eventually, 4-FPEAI passivated films were stable in the air at 30–40% RH for more than 10 days. Also, suppressed hysteresis was observed for the 4-FPEAI-passivated device than for the control 3D device apparently due to the slower ion diffusion from the perovskite layer to the other transport layers. The authors could obtain a very high PCE of more than 20% from the PV device using this bilayer perovskite as an absorber.<sup>57</sup> Furthermore, Gao and co-workers also computationally calculated the surface energies of  $(4\text{-FPEAI})_2\text{PbI}_4$ ,  $(\text{PEAI})_2\text{PbI}_4$  and CS/MA/FA-triple cation 3D-perovskites.<sup>57</sup> The lowest surface energy was calculated for  $(4\text{-FPEAI})_2\text{PbI}_4$  and highest for the CS/MA/FA-triple cation 3D-perovskite (*cf.* Fig. 19). This simulation of surface energy gave clue for the kinetically favoured formation of the bilayer structure upon contact of a film of the 3D-perovskite with the fluorinated cation. Further,



Fig. 19 The slab surface energy calculated for the Cs/MA/FA-triple cation 3D-perovskite,  $(\text{PEAI})_2\text{PbI}_4$  and  $(4\text{-FPEAI})_2\text{PbI}_4$ .<sup>57</sup> Reproduced with permission from ref. 57. Copyright 2019, John Wiley and Sons.

the calculated defect formation energy was also higher for  $(4\text{-FPEAI})_2\text{PbI}_4$  than  $(\text{PEAI})_2\text{PbI}_4$ .<sup>100</sup>

Ishikawa and co-workers also explored the 4-FPEAI spacer to develop a 2D/3D-bilayer structure, using the Cs/FA-double cation 3D-perovskite.<sup>118</sup> The formation of the 2D/3D-bilayer structure was confirmed from the UV-Vis absorption and XRD studies. The peak at 5.3 ( $2\theta$ ) in the XRD profile indicated the formation of a 2D-capping layer. The presence of characteristic absorption of the 3D-perovskite and the excitonic peak of the 2D-perovskite in the UV-Vis spectrum also confirmed the formation of a bilayer structure. The highest PCE of 20.6% was obtained for the device of the bilayer perovskite fabricated using 8 mM IPA solution of 4-FPEAI compared to 18.6% obtained for the control device. The improvement in PCE was the result of defect passivation and was confirmed from the enhancement in the PL intensity and PL lifetime. The formation of a 2D/3D-bilayer structure led to proper band alignment and blocked the migration of electrons from the perovskite layer to the hole-transport layer (HTL). The passivation using a higher or lower concentration of 4-FPEAI than 8 mM was detrimental to the PV performance due to the IPA mediated dissolution of the perovskite layer. Also, a higher concentration of 4-FPEAI increased the thickness of the insulating 2D-capping further hindering carrier mobility as observed in the study.<sup>118</sup>

The influence of spacer cations to manoeuvre the lattice orientation to affect carrier mobility and recombination kinetics at the interface of the 2D/3D-bilayer perovskite was studied by Grancini and co-workers.<sup>79</sup> The choice of the spacer cation was decisive in allowing oriented alignment of the 2D-layer over the 3D-perovskite that can significantly impact the PV performance. In the study, the authors compared fluorinated and nonfluorinated spacers, *i.e.*, PEA and 4-FPEAI, in passivating the Cs/FA/MA-triple cation perovskite and also investigated differences in their interfacial lattice growth alignment that impacted carrier dynamics to different degrees in these bilayer perovskites. Contrarily,<sup>118</sup> the better influence of PEA than 4-FPEAI to render parallel lattice alignment over a 3D-layer was confirmed in this study, which might have offered a better surface passivation leading to a slightly better PCE for the PEA than 4-FPEAI-based bilayer perovskite.<sup>79</sup> The PCE obtained from the PV devices of PEA and 4-FPEAI-based bilayer perovskites was 20.62% and 20.53%, respectively. Here, ultrafast transient absorption (TA) studies indicated that energy transfer from the 2D-layer to 3D-layer was absent in both these perovskites, which suggested probable dissociation of electrons.<sup>79</sup>

In continuation of a previous work,<sup>57</sup> Gao and co-workers investigated the way crystallization behaviour may be manoeuvred by changing the position of fluorine substitution in the PEA spacer due to the different dipole moment and formation energy along the series ( $o/m/p$  or  $2/3/4$ ) to impact morphology and other optoelectronic properties of the corresponding Cs/FA/MA-triple cation-based 2D/3D-bilayer perovskite.<sup>123</sup> The dipole moment increased in the order 2-FPEAI (12.37 D) < 3-FPEAI (16.04 D) < 4-FPEAI (17.39 D), facilitating carrier segregation (Fig. 20a). The authors observed that the best

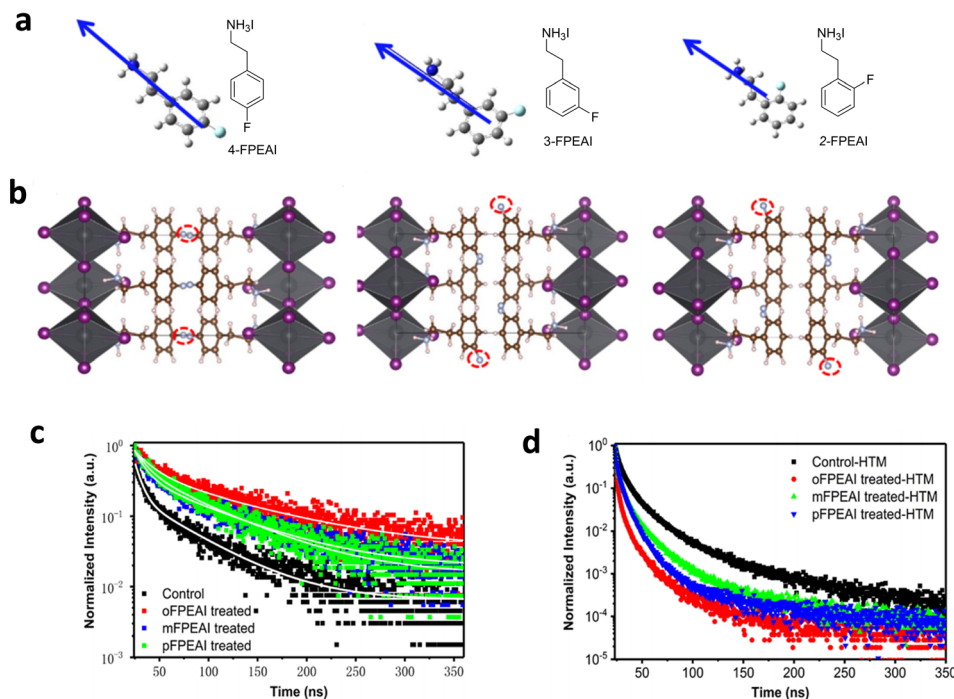


Fig. 20 (a) Dipole moments of (4/3/2)-FPEAI cations. (b) Crystal structures of (4/3/2)-FPEAI-based 2D-perovskites. (c) TRPL studies of (4/3/2)-PEAI treated 2D/3D-bilayer perovskites. (d) TRPL studies of the (4/3/2)-FPEAI-based 2D/3D-bilayer perovskite with HTL.<sup>123</sup> Reproduced with permission from ref. 123. Copyright 2020, John Wiley and Sons.

passivation offered by the 2-FPEAI-based bilayer perovskite was due to the hydrogen bonding between the F-atom and the NH-group of the FA cation that could reduce the defect density and facilitate carrier mobility, leading to a PCE of 20.06%, much higher than that obtained for the pristine 3D-perovskite. However, the best stability was seen for the 4-FPEAI-based bilayer perovskite showing a loss of only 1% efficiency upon exposure of unencapsulated devices to 10–30% RH over 1440 h. Also, the highest water contact angle of 81.7° for 4-FPEAI compared to the film of (2/3)-FPEAI was noted. The highest stability achieved upon 4-FPEAI passivation was the result of the lowest formation energy of the corresponding 2D-perovskite that resisted moisture-assisted hydrolysis.<sup>50</sup> Also, the better passivating effect of the 2-FPEAI cation was proven by the authors using the time-resolved photoluminescence studies (TRPL) that revealed the longest average lifetime of 63.1 ns for the 2-FPEAI-based bilayer perovskite compared to the (3 or 4)-FPEAI (*cf.* Fig. 20c).<sup>123</sup> Nevertheless, better carrier extraction from the perovskite layer to the HTL led to the best accelerated PL decay for the 4-FPEAI-based bilayer perovskite film with HTL (*cf.* Fig. 20d).

In another work, Gao and co-workers tailored the intrinsic properties, stability and PCE of 2D/3D-bilayer perovskites by manoeuvring the extent of fluorination of the PEA spacer.<sup>35</sup> The fluorinated spacers chosen for the study were 4-fluorophenylethylammonium iodide (4-FPEAI), 3,5-difluorophenylethylammonium iodide (3,5-F<sub>2</sub>PEAI), 2,4,5-trifluoroethylphenylethylammonium iodide (2,4,5-F<sub>3</sub>PEAI), and perfluorophenylethylammonium iodide (F<sub>5</sub>PEAI). From the DFT study, the dipole moments of these four spacers were calculated to be 11.7 D (4-FPEAI), 12.3 D

(3,5-F<sub>2</sub>PEAI), 14.2 D (2,4,5-F<sub>3</sub>PEAI), and 14.3 D (F<sub>5</sub>PEAI) (*cf.* Fig. 21a). This enhancement of the dipole moment with the extent of fluorination lowered the exciton binding energy and facilitated carrier dissociation, when explored for developing bilayer perovskites for PV devices.<sup>35</sup> Also, using DFT, formation energies of the corresponding 2D-perovskites were determined, and were found to increase with the increase in the fluorination of the spacer. A higher formation energy is responsible for higher stability, defect passivation and inhibition of ion migration in the 2D-phase of the 2D/3D-bilayer structure. The XRD studies revealed minimal changes in the FA/MA-double cation perovskite upon passivation with these fluorinated spacers. Also, XRD analysis suggested higher crystallinity for the films of all bilayer perovskites than the pristine 3D-perovskite; moreover the 2,4,5-F<sub>3</sub>PEAI passivated film had the highest crystallinity among the series with the smallest FWHM for the peak at ~14.1°. <sup>35</sup> The UV-Vis spectra of 3D and 2D/3D-bilayer perovskites were almost identical, revealing not many changes in the absorption properties. The PL emission around 780 nm was observed for the control 3D and 2D/3D-perovskite films. Notably, this emission peak at ~780 nm was intense for the passivated films than the pristine 3D-perovskite, and this intensity was highest for 2,4,5-F<sub>3</sub>PEAI, indicating highest suppression of non-radiative recombination.<sup>35</sup> A PL emission peak at 530 nm obtained from the top-side excitation confirmed the presence of the 2D-capping layer. The gradual distortion of the lattice with the increase in the extent of fluorination was confirmed from the crystal structure analysis (*cf.* Fig. 21b), and also from the blue-shift for PL emission of the pristine 2D-perovskites based on these spacers. The presence of surface islands in the SEM images of the 3D-film was probably due to the unreacted PbI<sub>2</sub> and could not

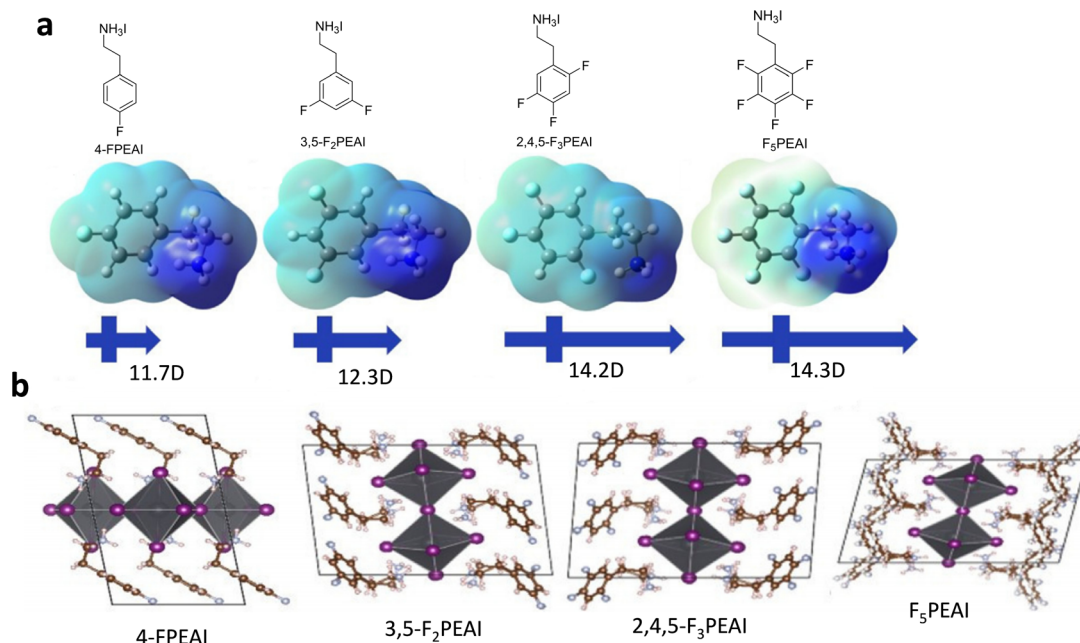


Fig. 21 (a) Dipole moments and ESPs (unit a.u.) of different fluorinated spacers. (b) The crystal structure of 2D-perovskites with different fluorinated cations, showing the enhanced lattice distortion with increasing numbers of fluorine atoms.<sup>35</sup> Reproduced with permission from ref. 35. Copyright 2022, Elsevier.

be traced during the SEM studies of the bilayer perovskites. This suggested consumption of excess PbI<sub>2</sub> during the formation of a bilayer structure. The SEM studies also indicated the formation of larger grains and good surface coverage upon passivation with these fluorinated spacers. Also, XPS studies revealed the presence of a C=O (C 1s) signature in the control 3D-film, which was absent for the 2D/3D-bilayer perovskites, suggesting inhibition of oxygen-triggered oxidation. The authors also studied the images of 2D/3D-bilayer perovskites using laser scanning confocal microscopy (LSCM). Prominent green emission from the top 2D-layer with a slight red emission from the underlying 3D-perovskite confirmed the formation of a bilayer structure. With the increase in the fluorination of the spacer cation, the intensity of green and red emissions observed from the LSCM became weaker, suggesting degradation of film quality and correlated with the trend of perovskite formation energy as obtained from DFT. Furthermore, a lower hole trap density for the 2D/3D-bilayer perovskite than the pristine 3D-perovskite was observed and the lowest value was for the 3,5-F<sub>2</sub>PEAI-based 2D/3D-bilayer perovskite. The highest PCE of 22.7% and large area PCE of 19.3% were achieved for the 2,4,5-F<sub>3</sub>PEAI-based bilayer perovskite. The high formation energy promoted effective defect passivation in the case of the 2,4,5-F<sub>3</sub>PEAI-based bilayer perovskite improving PV performance. However, the high formation energy could also deteriorate the morphology of the perovskite film due to the formation of poor-quality crystals over the 3D-perovskite, and might be the reason for a slightly lower PCE of 21.8% for the F<sub>5</sub>PEAI-based device. Compared to devices of the pristine 3D-perovskite, hysteresis was much lower for all the bilayer perovskites. Also, hysteresis dropped with an increase in the extent of fluorination of the spacer indicating slowed ion migration. An efficient carrier extraction at the interface between HTL and

perovskite was noted for the bilayer structure than the pristine one. To display hydrophobicity, water contact angles of 2D/3D-perovskite films were measured, which increased with increasing fluorine substitutions. The highest contact angle value of 85.1° for the F<sub>5</sub>PEAI-based bilayer perovskite was observed. For verified stability testing, films of 2D/3D-bilayer perovskite were stored inside a glove box for 105 days and, in all cases, PCEs were retained to an extent of 95% of the original value. In order to gain further insights into the moisture stability, control 3D and 2D/3D-perovskite devices were exposed to ambient environmental conditions with 60% RH for a period of 15 days. These 2D/3D-bilayer perovskites retained more than 89% of initial PCE. However, for pristine 3D-devices, PCE dropped below 79% of the initial value.<sup>35</sup>

Generally, the incorporation of bulky cations in bilayer perovskites limits the carrier mobility. Kai Zhu and his group addressed this transport issue pertaining to 2D/3D-bilayered perovskites by using a mixture of F<sub>5</sub>PEAI (0.75%) and PEAI (0.25%) to develop a 2D-passivating layer over the 3D-perovskite.<sup>39</sup> For this mixed cation-based passivated device, a high PCE of 21.1% in the inverted architecture under reverse scan was obtained.<sup>39</sup> Also extended moisture stability could be seen for this mixed cation-based 2D/3D-bilayer perovskite compared to only PEAI-based bilayer perovskite probably due to the hydrophobicity of the spacer. Furthermore, longer carrier lifetime and reduced density of traps led to a superior PV performance for this mixed cation-based bilayer perovskite. Interestingly, lower exciton binding energy for the mixed cation than PEAI-based perovskite also allowed carrier segregation and improved the transport property of the former. The higher conductivity of the mixed cation than PEAI-based bilayer perovskite was corroborated from the conductive atomic force

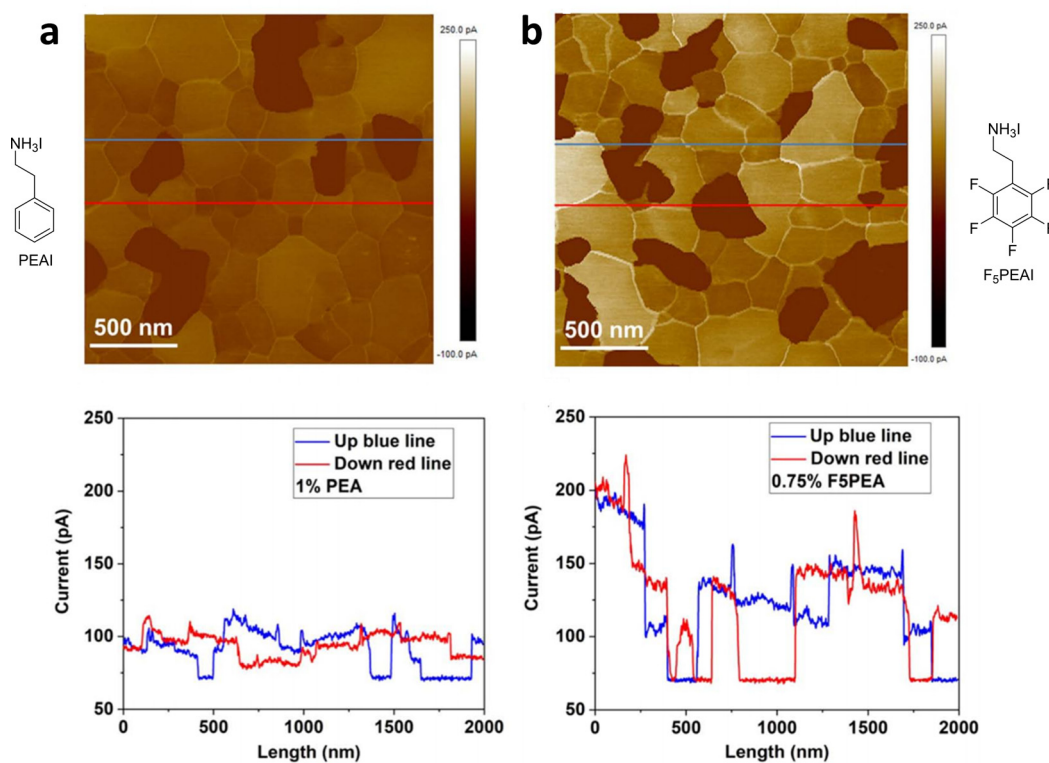


Fig. 22 (a) c-AFM studies of the 1%-PEAI-based bilayer perovskite. (b) c-AFM studies of the 0.75% F<sub>5</sub>PEAI and 0.25% PEA I-based bilayer perovskite.<sup>39</sup> Reproduced with permission from ref. 39. Copyright 2020, John Wiley and Sons.

microscopy (c-AFM) studies (*cf.* Fig. 22). The strong non-covalent interactions between F<sub>5</sub>PEAI and PEA I cations were also confirmed from the NMR and FTIR studies, which also contributed towards enhanced carrier mobility and superior performance of this mixed cation PV device.<sup>39</sup>

The nanoscale phase segregation upon self-assembly of arene-fluoroarene-based mixed spacers, which harvested an improved PCE of 21% with enhanced stability, was shown by Emsley and co-workers.<sup>47</sup> Improvement in the PV performance of the mixed spacer-based perovskite than the perovskite of individual spacer cations was seen.<sup>47</sup> For the study were explored the Cs/FA/MA-based triplet cation 3D-perovskite and a passivating composition of 1 : 1 PEA I : F<sub>5</sub>PEAI, which rendered a 2D/3D-bilayer structure. Unaltered peaks in the XRD suggested that passivation could not alter the structure of the 3D-phase to a greater extent. Similarly, unaltered UV-Vis and PL spectra for the bilayer perovskite also confirmed unaffected optoelectronic properties of the 3D-perovskite, a beneficial aspect when PV applications are considered. The superficial surface localization of the fluorinated spacer was also suggested from the XPS analysis of the PEA I : F<sub>5</sub>PEAI passivated films.<sup>47</sup> The PCE of the mixed cation passivated device was *ca.* 20% higher than that of the passivated devices of the individual cations due to the nanoscale phase segregation. Also, higher device stability from this mixed-cation passivation could be achieved in the study.

Nazeeruddin and co-workers explored and compared the effects of a more fluorinated spacer pentafluorophenylmethylammonium iodide (F<sub>5</sub>BAI) *vs.* a less fluorinated spacer 4-FPEAI

to tailor the lattice orientation, crystallinity, superhydrophobicity and other optoelectronic properties of the corresponding 2D/3D-bilayer perovskites.<sup>12</sup> The superior properties of the F<sub>5</sub>BAI-passivated film were the result of strong dispersion forces exerted by more fluorine atoms in the spacer. Furthermore, the defect passivation effect of F<sub>5</sub>BAI was due to the strong halogen bonding interactions that allowed parallel growth of the lattice, and did not alter the carrier transport and extraction. However, the random orientation of the lower dimensional phase was observed for the 4-FPEAI-based 2D/3D-perovskite, and was confirmed from the GIWAX studies. Interesting was the expansion of the lattice upon doping with F<sub>5</sub>BAI rather than 4-FPEAI. The UPS studies revealed no change in the valence band energies of F<sub>5</sub>BAI and pristine 3D-perovskites. Nevertheless, much deeper valence band energy was observed for the 4-FPEAI passivated film. Although wide band gap organic cations do not influence the valence and conduction band energies of the corresponding perovskites, they can influence the structure of the inorganic lattice due to the non-covalent interactions, tuning the optoelectronic properties (*cf.* Fig. 23). All these interactions and also in-plane oriented lattice growth induced by the F<sub>5</sub>BAI spacer rendered a PCE of 21.6% and long-term photostability over 1100 h under continuous illumination with retention of 86% of initial PCE for the unencapsulated device.<sup>12</sup> Further, improved resistance to photodegradation for the F<sub>5</sub>BAI passivated 2D/3D-perovskite was confirmed from the voltage-dependent transient photocurrent studies. The less affected PL decay kinetics for the F<sub>5</sub>BAI-based aged device suggested a

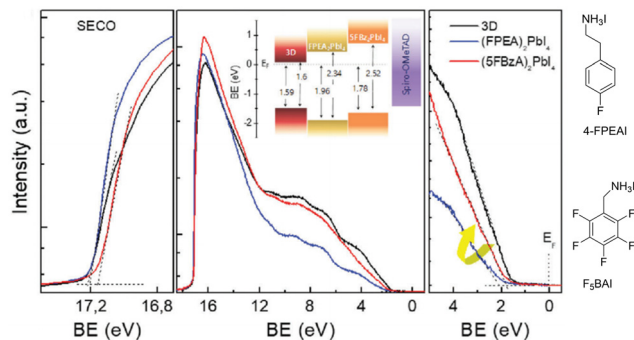


Fig. 23 UPS spectra and valence and conduction band energies of pristine 3D, 4-FPEAI and  $F_3$ BAI passivated perovskites.<sup>12</sup> Reproduced with permission from ref. 12. Copyright 2020, John Wiley and Sons.

lowering of the trap density due to the stabilizing interactions of this spacer. Also, high hydrophobicity for the  $F_3$ BAI-based 2D/3D-hybrid perovskite film was revealed from the water contact angle measurement, which was close to  $90^\circ$ . The voltage-dependent TRPL studies here indicated almost no change in the interface structure between perovskite and transport layers for the  $F_3$ PMAI-based device with ageing. The authors performed DFT studies and obtained a higher electrostatic surface potential (ESP) for the  $F_3$ BAI-based device than the 4-FPEAI-based bilayer perovskite, probably due to the influence of larger number of fluorine atoms in the former.<sup>12</sup>

Michael Grätzel and co-workers also explored  $F_3$ BAI to develop a superhydrophobic 2D/3D-bilayer perovskite.<sup>53</sup> The authors investigated the XPS depth profile of the bilayer structure to confirm the presence of the ligand within a thin 9 nm top layer. The GIWAX study revealed out-of-plane growth of the 2D-layer in this case. Also, GIWAX studies confirmed the consumption of the non-perovskite phase of  $FAPbI_3$  upon the formation of a bilayer structure. More than 90% PL quenching in the presence of HTL indicated the efficient extraction of holes from the bilayer perovskite, which also indicated strong interfacial interactions of the lower dimensional phase of the bilayer perovskite with HTL.<sup>53</sup> It is to be noted that strong interactions between the superhydrophobic lower-dimensional perovskite and the hydrophobic HTL were due to similar nature. The long carrier lifetime and efficient carrier extraction at the perovskite/HTL interface offered a PCE of 22.1%, independent of the scan speed. An electrochemical impedance spectroscopy study (EIS) also indicated inhibition of ion migration in this bilayer perovskite. The retention of 90% of initial PCE for unencapsulated device of the bilayer perovskite was observed upon 1000 h of exposure to 40% RH under 1 sun condition. However, a 43% drop in the PCE of the unencapsulated device for the 3D-perovskite under similar humidity and light conditions was evident. The lower surface energy of  $24.3 \text{ mJ m}^{-2}$  for the bilayer perovskite compared to a higher surface energy of  $54.7 \text{ mJ m}^{-2}$  for the pristine 3D-perovskite revealed superhydrophobic property induced by the perfluorinated cation.<sup>53</sup>

Chen *et al.* investigated the way electric dipoles at the interface of the 2D/3D-bilayer perovskite are oriented with the increase in the electronegativity of the spacer, that can potentially

manipulate carrier transport from the 3D-perovskite to the HTL.<sup>80</sup> In this work, a 2D/3D-bilayer perovskite was developed using the spacer cations PEAI, 4-FPEAI, and 4-trifluorophenylethylammonium iodide (4- $CF_3$ PEAI) over the FA/MA-based 3D-perovskite.<sup>80</sup> The XPS measurements of the 4- $CF_3$ PEAI-based 2D/3D-bilayer perovskite showed distinguished C=N and C-N peaks in the C 1s spectra, indicating the formation of a bilayer structure. The order of the electronegativity of these spacers as calculated from DFT was PEAI (1.27 D) < 4-FPEAI (2.69 D) < 4- $CF_3$ PEAI (4.27 D). The highest dipole moment of 4- $CF_3$ PEAI promoted best carrier segregation in the corresponding bilayer perovskite. Also, the largest interfacial dipole was deciphered for the 4- $CF_3$ PEAI-based 2D/3D-bilayer perovskite, followed by 4-FPEAI and PEAI-based bilayer perovskites from the work function calculations. Also, the highest calculated Bader charge value at the interface of the 4- $CF_3$ PEAI-based 2D/3D-perovskite suggested most facile carrier transport across this 2D/3D-heterojunction among the series.<sup>80</sup> In this study, the contact potential difference (CPD) was measured from the KPFM studies and the highest value was noted for the 4- $CF_3$ PEAI-based 2D/3D-heterojunction, indicating the formation of a largest interfacial dipole.<sup>80</sup> The best passivation effect of 4- $CF_3$ PEAI in the 2D/3D-perovskite was attributed to the strong hydrogen bonding interactions between the  $CF_3$  group and FA/MA cations that led to superior PV performance. Although the band gap widened for the PEAI-based 2D/3D-perovskite that offered some extent of passivation, due to the non-polarity of PEA, the electric field was not much enhanced at the 2D/3D-interface, necessary for the de-trapping of charge carriers from within the intrinsic defects of the 3D-perovskite. However, for highly electronegative spacer 4- $CF_3$ PEAI, and also for 4-FPEAI, charge carrier de-trapping from within the intrinsic defects of the 3D-perovskite was facilitated by a larger electric field generated at the interface of the 2D/3D-layer due to the orientation of the  $CF_3$  group of the spacer towards the 3D-perovskite and the ammonium group towards the HTL side (*cf.* Fig. 24). This higher carrier de-trapping reduced non-radiative recombination and improved carrier transport across the 2D/3D-heterojunction boosting PCE to a remarkable high of 22.4% for the 4- $CF_3$ PEAI-based 2D/3D-bilayer perovskite, highest among the series. Subsequently, this carrier de-trapping lowered the ion migration and reduced the hysteresis significantly for the 4- $CF_3$ PEAI-based device. Also, the highest carrier density, carrier extraction and lowest non-radiative recombination were confirmed from the PL studies of the 4- $CF_3$ PEAI-based 2D/3D-perovskite with and without the presence of a HTL layer. The high stability of the 4- $CF_3$ PEAI-based bilayer perovskite was confirmed after storing the unencapsulated devices under  $\sim 30\%$  RH at room temperature for >1400 h. The devices of the 4- $CF_3$ PEAI-based bilayer perovskite retained 80% of initial PCE, whereas the PCE of the control 3D device dropped to 60% of the initial value. An AIMD simulation was also done to gain insights into the high stability of the 4- $CF_3$ PEAI-based bilayer perovskite towards humidity. It was observed that the water repellent  $CF_3$  group formed a compact hydrophobic surface over the 3D-perovskite by adopting an upright configuration within the 2D-layer, suppressing hydrogen bonding with water, and offering long-term stability.<sup>80</sup>

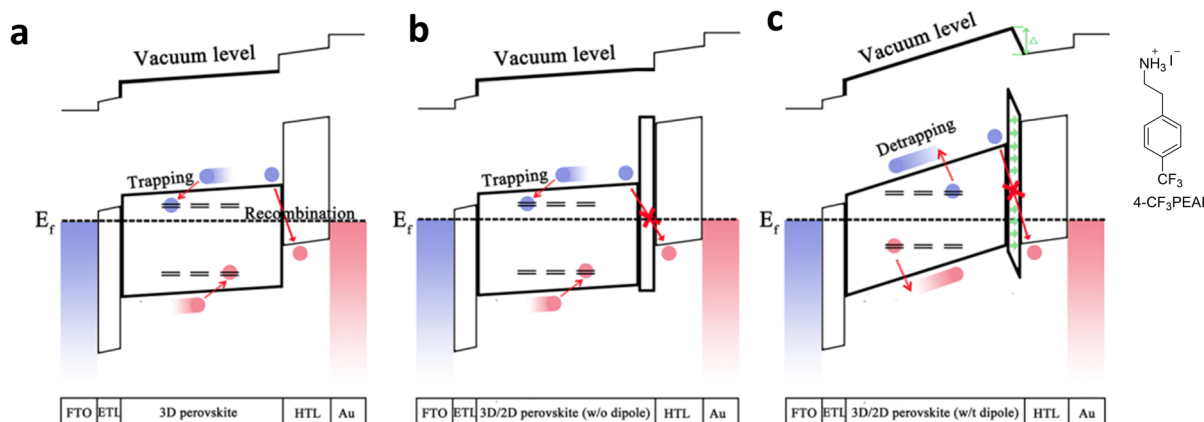


Fig. 24 (a) Carrier trapping and de-trapping at the interface of 3D-perovskite/HTL. (b) Carrier trapping and de-trapping at the interface of the 2D/3D-bilayer perovskite based on the nonpolar spacer (PEAI)/HTL. (c) Carrier trapping and de-trapping at the interface of the 2D/3D-bilayer perovskite based on the polar spacer (4-CF<sub>3</sub>PEAI)/HTL.<sup>80</sup> Reproduced with permission from ref. 80. Copyright 2021, American Chemical Society.

By using amidinium-based ligands with different *para*-substitutions, *i.e.*, benzamidine hydrochloride (PhFACI), 4-hydroxybenzamidine hydrochloride (4-HOPhFACI) and 4-fluorobenzamidine hydrochloride (4-FPhFACI), Chen and co-workers tailored the properties of the corresponding FA/MA-double cation 2D/3D-bilayer perovskite to improve the PV performance.<sup>63</sup> The SEM images revealed larger grains without any horizontal grain boundaries for these 2D/3D-hybrid perovskites based on amidinium ligands compared to the control 3D-perovskite. Similarly, crystallinity was also improved relative to the 3D-perovskite as confirmed from the sharper XRD peaks. Band gap widening due to the higher content of the 2D-perovskite in the bilayer structure led to slightly blue-shifted absorption and emission for PhFACI/4-FPhFACI/4-HOPhFACI-based 2D/3D-perovskites than control 3D. Notably, this blue shift was least for the 4-FPhFACI-based perovskite. Enhanced PL lifetime for all these bilayer perovskites than the control 3D-perovskite was revealed, which suggested strong NH<sub>2</sub>⋯I hydrogen bonding interactions between the organic layer and the inorganic lattice that quenched non-radiative recombination due to the defect passivation. Contrary to another report, regarding RP-perovskites with the same amidinium cations, 20.65% PCE obtained for the 4-FPhFACI-based 2D/3D-bilayer perovskite device was slightly lower than the 21.42% and 20.90% PCE obtained, respectively, for 4-HOPhFACI and PhFACI-based bilayer perovskites.<sup>59,63</sup> This subtle difference in the PV performance could be due to the different architectures and compositions of the perovskite layers followed in the two works: an RP-type perovskite structure was explored in the work of Liu *et al.*<sup>59</sup> and a 2D/3D-bilayer structure was reported in this work.<sup>63</sup>

Zhao and co-workers investigated the influence of ligand-mediated physicochemical events at the interface of the 2D/3D-bilayer perovskite that impacted interfacial carrier extraction and PV performance.<sup>82</sup> The orientation of the 2D-layer over the 3D-perovskite in a bilayer structure is crucial for carrier extraction from 3D to 2D-phase.<sup>11</sup> In this work, Zhao revealed the influence of a fluorinated spacer in controlling the thickness and lattice orientation within the quantum well-2D-capping layer of a bilayer

perovskite. Not only that, a fluorinated spacer could influence the carrier extraction at the interface of the 2D/3D-bilayer perovskite. Zhao *et al.* in the study developed a RP-type 2D-perovskite over a 3D-FAPbI<sub>3</sub> template.<sup>82</sup> Notably, this RP-perovskite was developed by spin coating a solution of PEA, 4-FPEAI, BuAI (butylammonium iodide) or CF<sub>3</sub>BuAI (trifluorobutylammonium iodide) over thermally annealed (1:1.08) FAI:PbI<sub>2</sub> films. Improved surface morphology for the bilayer perovskite was noted. Interestingly, a phase pure (*n* = 2) 2D-perovskite over the 3D-perovskite was obtained, upon the use of aliphatic spacers like CF<sub>3</sub>BuAI or BuAI. However, when aromatic spacers PEA or 4-FPEAI were used for developing 2D/3D-bilayer structures, mixed phases (*n* = 1, *n* = 2) resulted, hindering the interfacial carrier extraction and transport. The randomly oriented growth of lattice planes of the 2D-perovskite within the bilayer structure confirmed the influence of fluorinated spacers 4-FPEAI and CF<sub>3</sub>BuAI towards this.<sup>82</sup> Contrary to other reports, the absence of fluorine atoms in the spacer cations, such as for PEA or BuAI, yielded more aligned out-of-plane quantum well structures within the capping layer of the 2D/3D-bilayer and was confirmed from both GIWAX and TA studies. Also, TA studies indicated the negligible influence of the fluorine-tethered spacers towards interfacial carrier transport dynamics within the 2D/3D-bilayer perovskite, which is in contrast to other reports.<sup>82</sup> Similarly contrary to other reports, electron mobility was measured to be much lower within the 2D-capping layer of the 2D/3D-bilayer perovskite of fluorinated cations.<sup>39</sup> This lower electron mobility within 2D/3D-bilayer films developed with fluorinated cations suggested higher trap density, higher recombination losses, lower passivation and a randomly oriented lattice within the capping layer, which are contrary to the other studies discussed in this highlight.<sup>82</sup> We believe that the differences in the properties of the perovskite observed in this work from the other ones could be due to the different structures of the capping layer.<sup>39,82</sup>

Nazeeruddin and his group explored a multi-fluorinated organic cation (CF<sub>3</sub>)<sub>3</sub>Co(CH<sub>3</sub>)<sub>3</sub>NH<sub>3</sub><sup>+</sup>, namely A43, as a water-proof protective jacket in a 2D/3D-bilayer perovskite (*cf.* Fig. 25).



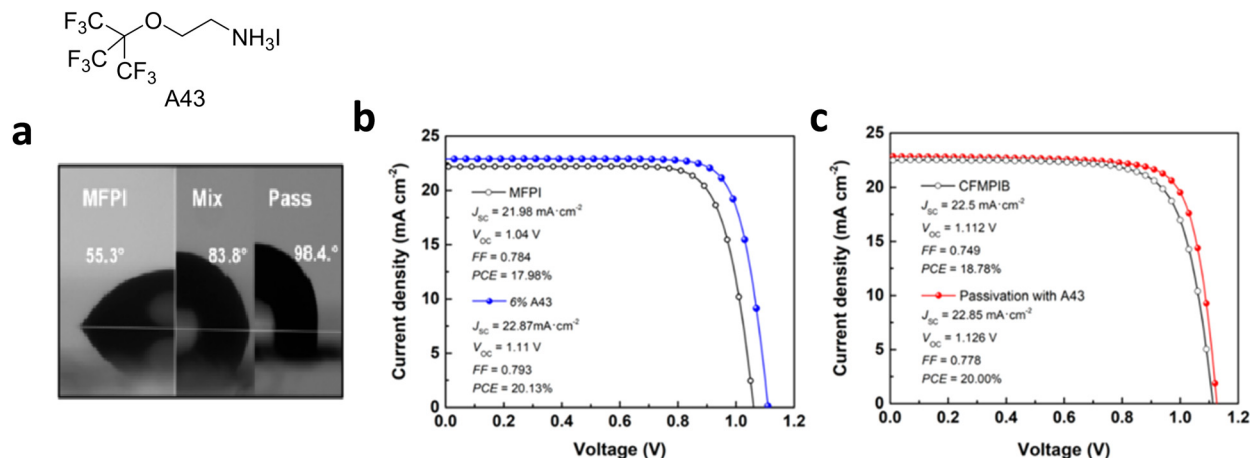


Fig. 25 (a) Water contact angle studies of pristine MFPI and A43 doped 2D/3D-films of MFPI and CFMPIB. (b) Current–voltage curves for MFPI- and A43-MFPI based 2D/3D-perovskite devices. (c) Current–voltage curves for pristine CFMPIB and A43-based 2D/3D-perovskite devices.<sup>31</sup> Reproduced with permission from ref. 31. Copyright 2018, American Chemical Society.

This protective capping of the 2D-perovskite offered resistance from moisture invasion and ion migration. Here, the bilayer perovskite was developed either by direct mixing A43 with MA<sub>0.9</sub>FA<sub>0.1</sub>PbI<sub>3</sub>(MFPI) in different percentages or by layered deposition over 3D-perovskite Cs<sub>0.1</sub>FA<sub>0.74</sub>MA<sub>0.13</sub>PbI<sub>2.48</sub>Br<sub>0.39</sub>-(CFMPIB).<sup>31</sup> From the UV-Vis absorption study, a constant peak around 780 nm suggested retention of the optical features of 3D-MFPI in the doped films. Except for slightly blue-shifted absorption spectra of pure CFMPIB with respect to MFPI, probably due to the presence of Cs, no other substantial differences in the absorption properties were revealed upon the formation of the bilayer structure. A highly oriented lattice growth for a film of A43 doped MFPI was seen, which suggested the influence of the fluorinated spacer in the self-assembly process to form a bilayer structure. Also was analyzed PL emission of 2D/3D-bilayer MFPI and CFMPIB-based perovskites both from the top and bottom excitations. The emission peak around 770 nm for top and bottom excitations obtained for the doped MFPI and CFMPIB films matched the emission property of the 3D-perovskite, confirming the presence of a pristine 3D-phase. The emission peak at 570 nm for A43 doped MFPI indicated the growth of very small crystals of lower-dimensional phase over the 3D phase. The water contact angle enhancement to 83° and greater values also indicated the presence of a hydrophobic lower dimensional moisture tolerant capping layer over pristine 3D-MFPI and CFMPIB layers (*cf.* Fig. 25). The stability test by monitoring the XRD of the pristine film stored under 50% RH revealed complete decomposition, but extended stability was observed for the doped films. A champion PCE of 20% independent of scan speed was observed for 6% A43 passivated devices of MFPI and CFMPIB, suggesting inhibition of ion movement and reduction of non-radiative recombination (*cf.* Fig. 25b and c). Also, enhanced stability for more than 100 h was observed for A43-doped devices. However, a drop in PCE beyond 20% doping revealed the presence of a greater amount of lower-dimensional phases.<sup>31</sup>

## 6. Fluorine-based spacers or additives as passivators for perovskites

In this section, passivation studies involving aromatic fluorinated spacers are discussed first, followed by multi-fluorinated aromatic spacers with the ammonium anchoring group for PV applications. Next studies exploring aromatic imidazolium-type and iodopentafluorobenzene spacers are summarized. Then, we discuss the tailoring of perovskite properties and PV performances using molecules with fluorine atoms present on aliphatic side arms. At the end, passivation with photocurable fluorinated polymers, fluorinated graphene nanoplates and fluorinated fullerenes is discussed.

Direct interfacial passivation of the FA/MA-mixed cation 3D-perovskite with a hydrophobic 4-FPEAI spacer was shown by Xu and co-workers.<sup>11</sup> In this study, the presence of a capping layer of 4-FPEAI rather than the corresponding 2D-perovskite was confirmed from the XRD study. Furthermore, the formation of the 4-FPEAI capping layer could not influence the absorption spectrum. The binding energy at ~292 eV obtained by the XPS study confirmed the formation of intermolecular  $\pi$ - $\pi$  interactions between 4-FPEAI spacers. Also, the filling of iodine vacancies post passivation was established from the increase in the I/Pb ratio as indicated from the XPS study (*cf.* Fig. 26). Importantly, this passivation strategy could protect the underlying 3D-layer from heat, as annealing was not necessary here. Such passivation improved carrier mobility, lowered carrier trapping, reduced non-radiative recombination and offered higher stability leading to an improved PCE of 21% compared to 19.5% for the pristine 3D-device.<sup>11</sup> Nevertheless, increasing the passivation with 4-FPEAI above a critical limit was detrimental and reduced PCE probably due to the excessive accumulation of the insulating spacers over the 3D-layer. Also, lower electron trap density upon passivation with 4-FPEAI was confirmed from the SCLC method. The PL intensity and lifetime enhanced post-passivation and confirmed suppressed non-radiative recombination. Similarly, SEM studies also established

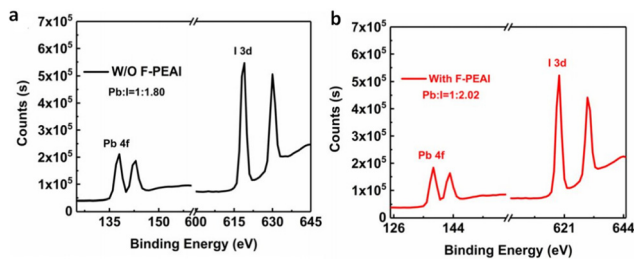


Fig. 26 (a) XPS profile of the control 3D-film showing the Pb:I ratio. (b) XPS spectrum of the passivated film showing an enhanced Pb:I ratio.<sup>11</sup> Reproduced with permission from ref. 11. Copyright 2021, American Chemical Society.

the filling of surface traps upon 4-FPEAI passivation. Moreover, higher stability for 4-FPEAI treated unencapsulated devices than unencapsulated devices of the pristine 3D-perovskite was confirmed from the retention of 90% of initial PCE, after 720 h upon exposure to 40% RH. However, the PCE of the pristine 3D device decayed to 23% of the initial value under similar conditions. Likewise, inhibition of oxygen-mediated surface oxidation upon passivation was confirmed from the decrease in the XPS peak area of C=O/C-C.<sup>11</sup>

Shaw and co-workers explored a combination of F<sub>5</sub>PEAI and MAPbI<sub>3</sub> to attain a high PCE of 21.1% for PV devices in an inverted architecture, integrating stability to heat and moisture at the same time.<sup>125</sup> Here also the PCE of devices dropped when the concentration of the fluorine-based spacer was kept above a critical limit. The best cell was made with 0.3 mol% of (F<sub>5</sub>PEA)<sub>2</sub>PbI<sub>4</sub>, which outperformed the PV performance of pristine 3D-MAPbI<sub>3</sub>. The absorption spectrum of the 3D-perovskite

containing up to 10 mol% of (F<sub>5</sub>PEA)<sub>2</sub>PbI<sub>4</sub> was identical to that of the pristine MAPbI<sub>3</sub>; nevertheless, red hue was relatively clear in these doped films, probably due to the differences in the crystal size and orientation. Similar absorption spectra as of the pristine 3D-material corroborated the presence of a limited amount of 2D-phases with  $n \leq 4$  in the doped films.<sup>125</sup> No significant PL shift compared to the 3D-pristine film upon doping with a 2D-perovskite of concentration less than 10 mol% also suggested limited content of lower dimensional phases with  $n \leq 4$ . However, upon increasing doping to 50 mol% of (F<sub>5</sub>PEA)<sub>2</sub>PbI<sub>4</sub>, a new peak in the PL emission at < 600 nm suggested the presence of the  $n \geq 4$  phase. Notably, the GIWAX study, in this work, could not indicate the presence of a separate 2D-capping layer over the 3D-perovskite. Nevertheless, conspicuous was the formation of larger more oriented crystals of the 3D-perovskite towards the surface than in the bulk post-doping. Also, the parallel orientation of (110) planes of MAPbI<sub>3</sub> upon doping with 10 mol% of (5-FPEA)<sub>2</sub>PbI<sub>4</sub> was confirmed from the GIWAX study. This suggested that (5-FPEA)<sub>2</sub>PbI<sub>4</sub> crystals capped the MAPbI<sub>3</sub> crystals towards the surface promoting parallel alignment. Such a capping of MAPbI<sub>3</sub> crystals towards the surface offered defect passivation, which was also confirmed from the enhanced PL intensity. The XPS studies confirmed the location of the fluorine-tethered ligand in the top 50 nm thick layer of doped films (*cf.* Fig. 27a). Besides, mostly a similar composition was revealed for the bulk part of doped and pristine films from the XPS study. Due to the electronegativity of the fluorine atom, an enhancement in the work function with the increase in the mol% of 2D-perovskite was revealed from the scanning Kelvin probe microscopic studies (SKPM) (*cf.* Fig. 27d). Also, the highest surface potential

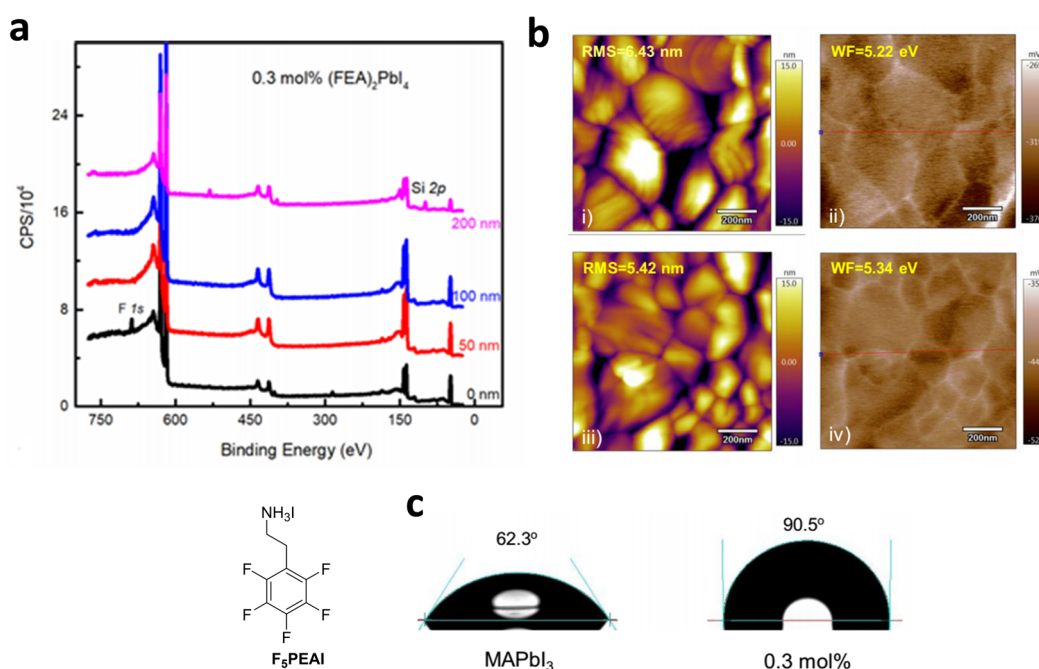


Fig. 27 (a) XPS-depth profiles of 0.3 mol% (F<sub>5</sub>PEA)<sub>2</sub>PbI<sub>4</sub> films. (b) AFM and SKPM images of MAPbI<sub>3</sub> (i and ii) and 0.3 mol% (F<sub>5</sub>PEA)<sub>2</sub>PbI<sub>4</sub> doped films (iii and iv). (c) Water contact angles of pristine and doped films.<sup>125</sup> Reproduced with permission from ref. 125. Copyright 2021, Springer Nature.

## Highlight

difference was seen at the grain boundaries, suggesting maximum localization of fluorinated spacers over these regions. The higher moisture tolerance of the doped film was suggested from the water contact angle studies, which were  $\sim 90^\circ$  for 0.3 mol% doped and  $\sim 60^\circ$  for pristine films (*cf.* Fig. 27c). Similarly, the higher thermal stability of the doped than pristine devices was confirmed by heating the unencapsulated devices at  $85^\circ\text{C}$  at a RH of  $85 \pm 10\%$ . In this regard, a higher T80 value of 183 h for 0.3 mol% doped films than 55 h for the pristine 3D-perovskite suggested higher thermal stability due to greater defect passivation.<sup>125</sup> The results presented in this work extended a unique concept of doping with a small mol% of fluorinated spacers to grow 3D-perovskites that may not always offer a 2D/3D-bilayer assembly. Nevertheless, such a small percentage of doping could be substantial to offer remarkable stability towards moisture or heat. Besides, an increase in the doping above a critical limit could also be detrimental to the PV performance and stability as highlighted in this work.<sup>125</sup>

CsPbI<sub>2</sub>Br has superior light-harvesting properties and phase stability than the CsPbI<sub>3</sub> perovskite.<sup>129</sup> However, the bottleneck in the way of its application as a solar-light absorber is low in-operando stability. The surface passivation to reduce trap states and improve the stability of CsPbI<sub>2</sub>Br using fluorine-tethered spacer 4-CF<sub>3</sub>PEAI was reported by Zheng *et al.*<sup>129</sup> The SEM studies revealed pinhole free compact morphology for the passivated CsPbI<sub>2</sub>Br film compared to the pinhole populated morphology of the control perovskite. This pinhole-free superior morphology remarkably reduced the trap-assisted recombination at the grain boundaries. Also, the interaction between the inorganic lattice and 4-CF<sub>3</sub>PEAI was confirmed from the shift of the Pb (4f) XPS peak towards higher binding energy post-passivation. The reduced trap density was also confirmed from the PL enhancement post-passivation. It was envisaged that 4-CF<sub>3</sub>PEAI led defect passivation at the grain boundaries was due to the electrostatic interaction exerted towards Pb<sup>2+</sup> that filled iodine and Cs-vacancies. Notably, absorption properties and phase purity of CsPbI<sub>2</sub>Br were not influenced by the passivation with 4-CF<sub>3</sub>PEAI which was confirmed from the UV-Vis and XRD studies. Furthermore, the XRD study also confirmed the absence of a diffraction peak for 2D (4-CF<sub>3</sub>PEA)<sub>2</sub>PbI<sub>4</sub>, corroborating the absence of a bilayer structure. This surface passivation with 4-CF<sub>3</sub>PEAI improved PCE to 16.07% compared to 14.05% for the non-passivated device. Also, around a 10% drop in the hysteresis index was noticed for the passivated device due to the remarkable reduction in the trap density. Likewise, shelf-life improved considerably for the passivated and encapsulated CsPbI<sub>2</sub>Br device with retention of 88% of initial PCE after 7 days, which however dropped to 61% of initial PCE in the control device. A higher water contact angle of  $95^\circ$  than  $70^\circ$  for the control film suggested higher hydrophobicity achieved upon 4-CF<sub>3</sub>PEAI passivation.<sup>129</sup>

Michael Grätzel and co-workers treated the Cs/FA/MA-triple cation perovskite with 4-(trifluoromethyl)benzylammonium iodide (4-CF<sub>3</sub>BAI) to impart hydrophobicity, passivate cation vacancies and prevent infiltration of lithium ions from the HTL into the underlying perovskite layer.<sup>130</sup> Upon use as a surface passivating agent, the ammonium group of the 4-CF<sub>3</sub>BAI spacer

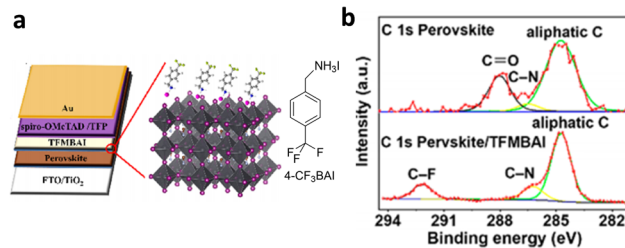


Fig. 28 (a) The passivation of the triple cation perovskite with 4-CF<sub>3</sub>BAI. (b) XPS spectrum showing disappearance of the C=O peak upon passivation.<sup>130</sup> Reproduced with permission from ref. 130. Copyright 2021, American Chemical Society.

entered inside the A-site vacancies, and passivated them (*cf.* Fig. 28a). This passivation prevented non-radiative recombination and improved PLQY. However, the effect of passivation on carrier extraction at the perovskite/HTL interface was not seen from the TRPL study. Upon passivation, a textured top layer formed as the SEM study indicated. Further, the XPS depth profile suggested a 50 nm thick capping layer. This surface passivation with 4-CF<sub>3</sub>BAI was effective in preventing perovskite oxidation as revealed from the disappearance of the C=O peak at 288 eV in the XPS profile (*cf.* Fig. 28b). Notable was a high PCE of 23.94% with minimum hysteresis of 0.6% for the 4-CF<sub>3</sub>BAI passivated device. Moreover, reproducible PV parameters were achieved upon 4-CF<sub>3</sub>BAI passivation. Also, the water contact angle improved from  $60^\circ$  for the pristine film to  $90^\circ$  for the passivated film. Less than 3% reduction in the PCE of the passivated device was confirmed from the ageing test under 60–70% RH for 45 days, which indicated in-operando stability.<sup>130</sup>

Huang and co-workers also studied passivation of the Cs/FA/MA-based triple cation perovskite with 4-CF<sub>3</sub>BAI.<sup>109</sup> The best result was achieved with 1% passivation using 4-CF<sub>3</sub>BAI which led to a champion PCE of 20.56% compared to 19.25% for the control device. The passivation not only improved the PCE, but also enhanced the hydrophobicity of the perovskite film, as indicated from the increase in the water contact angle from  $76.05^\circ$  to  $106.38^\circ$ . At the same time, enhanced absorption intensity without significant shift of the absorption edge was noticed post-passivation of the perovskite in the study.<sup>109</sup> The 1% passivation induced increased crystallinity and superior film morphology with enhanced grain size were confirmed from the increase in the intensity of the XRD peaks and also from the SEM studies. Here, the passivating effect of 4-CF<sub>3</sub>BAI was attributed to strong interactions with Pb<sup>2+</sup> that shifted the binding energy of the Pb<sup>2+</sup> (4f) peak in the XPS spectrum and tremendously reduced trap-assisted recombination at the iodine vacancies. Likewise, suppressed redox reaction of Pb was confirmed from the weakening of the metallic Pb<sup>0</sup> peak after passivation. Enhancement in the PL intensity and lower hole trap density confirmed effective passivation with 4-CF<sub>3</sub>BAI, which led to better extraction and transport of the holes from the perovskite to the HTL. After 3500 h of exposure to 25–35% RH, the 1% 4-CF<sub>3</sub>BAI passivated device without encapsulation retained 84% of initial PCE, whereas under similar ageing conditions the pristine device lost 80% of initial PCE. Remarkable

stability could be noted with the retention of the black colour of the passivated film, post-soaking inside water for 60 s. Nevertheless, the non-passivated perovskite film turned yellow within 5 s of soaking. Similarly, 4-CF<sub>3</sub>BAI passivation rendered higher thermal and photostability compared to the control device.<sup>109</sup>

The vertical growth of the inorganic slabs of the (ThMA)<sub>2</sub>-(FA)<sub>4</sub>Pb<sub>5</sub>I<sub>16</sub>-based RP-perovskite was achieved using 4-CF<sub>3</sub>BAI, where ThMA represents the 2-thiophenemethylammonium cation.<sup>51</sup> Here, passivation was performed by dropping an IPA solution of 4-CF<sub>3</sub>BAI over the film of the RP-perovskite. The SEM studies confirmed compact, pin-hole-free superior morphology for the passivated compared to control RP-perovskite films.<sup>51</sup> The surface distribution of fluorine for the passivated film was mapped using energy dispersive spectroscopy (EDS). No change in the band gap upon passivation was confirmed from the UV-Vis study. Further, the XRD study confirmed out-of-plane growth of the inorganic slabs with respect to the substrate due to the absence of (0k0) diffraction for the 4-CF<sub>3</sub>BAI passivated film. Also, the increased XRD peak ratio of  $I_{(202)}/I_{(111)}$  for the passivated film suggested preferential vertical alignment of the lattice. Nevertheless, parallel growth of the inorganic slabs with respect to the substrate was traced from the XRD studies of the control sample. The high quality of the film and preferential vertical orientation of the inorganic slabs led to remarkable improvement in the PCE to 19.06% for the passivated compared to 16.18% for the control perovskite device. The more negative work function upon passivation suggested n-type character for the passivated compared to the control film. This signified a reduction in the trap density and also trap assisted non-radiative recombination due to 4-CF<sub>3</sub>BAI passivation, which was also confirmed from the two-times enhancement in the PL intensity and PL lifetime upon passivation.<sup>51</sup> The out-of-plane growth of the inorganic slabs offered higher hole and electron mobility and reduced the trap density for the passivated films.<sup>51</sup> Furthermore, passivation achieved here improved in-operando stability due to the hydrophobicity of the 4-CF<sub>3</sub>BAI-based spacer. Upon exposure to 30 ± 5% RH, the control unencapsulated device lost 66% of initial PCE after 552 h. However, the passivated perovskite device retained 99% of initial PCE even after similar exposure for 552 h. Also, extensive improvement in thermal stability was seen upon passivation with retention of 96% of initial PCE upon heating at 80 °C under a nitrogen atmosphere for 576 h.

1-Methyl-3-(1*H*,1*H*,2*H*,2*H*-nonafluorohexyl)-imidazolium iodide, named FIm, as a passivating layer for the 3D-MAPbI<sub>3</sub>-based perovskite was explored by Ahmad and co-workers.<sup>108</sup> Here, the passivation led to extended stability under ambient conditions for more than 100 days for the unencapsulated devices without impacting PCE.<sup>108</sup> The doping with FIm at 1 mol% could not affect the lattice structure or grain size of the 3D-perovskite, which was confirmed from the XRD and SEM studies. However, the dopant formed a thin capping layer around the 3D-perovskite, which was apt to retain the efficiency and remarkable inherent properties of the 3D-material, with the integration of stability at the same time.<sup>108</sup>

As discussed before, a perovskite film or crystal contains unbalanced charges, due to the uncoordinated A-site, B-site or

X<sup>-</sup> ions present at the surface.<sup>36</sup> These uncoordinated A/B sites or halide ions act as the defect sites to trap carriers, particularly for holes that are injected into the HTL, and create interfacial dipole. Also, these unsaturated X<sup>-</sup> sites initiate perovskite decomposition due to the interaction with water or oxygen molecules at the surface. Snaith and co-workers passivated these uncoordinated X<sup>-</sup> centres of the MAPbI<sub>3</sub> perovskite using iodopentafluorobenzene (IPFB). IPFB-based passivation was the result of halogen bonding interactions between the electron-deficient iodine centre of IPFB and electron-rich coordinatively unsaturated halide centres.<sup>36</sup> It is to be noted that these iodine centres in IPFB are extremely electron deficient due to the electron withdrawing effects of the five electronegative fluorine atoms. Hence, these iodine atoms formed halogen bonds with electron-rich X<sup>-</sup> centres that ultimately suppressed interfacial hole-trapping due to the screening of X<sup>-</sup> sites from the injected holes (*cf.* Fig. 29). This halogen bonding between iodine of IPFB and uncoordinated X<sup>-</sup> centres of the perovskite was proven with the help of solid state <sup>13</sup>C and <sup>19</sup>F NMR studies. The downfield shift of *ca.* 2 ppm for the carbon attached to the iodine centre indicated the involvement of this iodine centre in halogen bonding.<sup>36</sup> The passivation led to an improvement in the PCE to 15.7% for the passivated device compared to 13% obtained for the control device. TA studies for the passivated film also revealed a three-fold enhancement in the hole lifetime compared to the control film, confirming the slower recombination due to the defect passivation.<sup>36</sup>

The degradation of perovskites is initiated not only from the defects present towards the surface, but also from the defects present at the grain boundaries. These defects are detrimental to the stability and PV performance due to the carrier trapping led non-radiative recombination as discussed already.<sup>36,38</sup> Importantly, the density of these defects is higher towards the grain boundaries than at the surface due to the larger specific area of the former. In order to co-passivate both kinds of defects at the surface and at the grain boundaries of the MAPbI<sub>3</sub>-perovskite, Guo *et al.* explored 1*H*,1*H*-perfluorooctylamine (PFOA) as an additive in the perovskite precursor solution. It was shown that co-passivation of both these defects improved the PV performance and stability to a greater extent than obtained only from the surface defect passivation.<sup>38</sup>

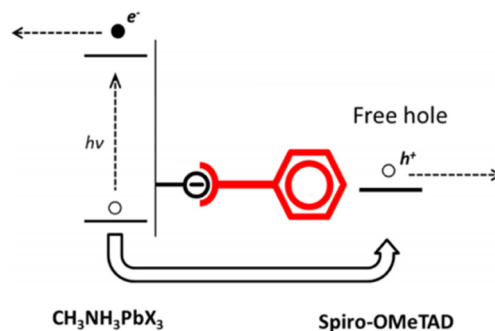


Fig. 29 Passivation of X<sup>-</sup> centres present towards the surface of the perovskite film or crystal with IPFB.<sup>36</sup> Reproduced with permission from ref. 36. Copyright 2014, American Chemical Society.

## Highlight

The PFOA-mediated co-passivation of both kinds of defects was due to the electron donation from the nitrogen atom of the fluorinated molecule to the empty 6p-orbital of the uncoordinated  $\text{Pb}^{2+}$  centre. Further, this co-passivation led by PFOA improved the film morphology without affecting the grain size due to the suppression of over-crystallization of  $\text{PbI}_2$ . The enhancement of the absorption intensity was also noticed upon co-passivation with PFOA. The presence of PFOA at the surface and within the deeper layers of the film was confirmed from the mapping of fluorine using EDX, which suggested the co-passivation of defects both at the surface and also within the interior grain boundaries. The crystallinity of the perovskite was not much affected by the co-passivation, as confirmed from the XRD study. The remarkable enhancement in the PL intensity and lifetime upon passivation revealed a drop in the trap-assisted non-radiative recombination, which improved PV performance. The influence of co-passivation with 6% PFOA upgraded PCE to 16.18% compared to 12.71% obtained for the pristine perovskite. Also, negligible hysteresis was seen upon co-passivation. Along with improved PCE, improved stability was attained upon PFOA co-passivation with a retention of 95% of initial PCE upon exposure to  $50 \pm 5\%$  RH at  $25^\circ\text{C}$  after 800 h for the unencapsulated device. On the other hand, the control device lost 80% of initial PCE within 500 h, under similar ageing conditions.<sup>38</sup> The broader scope of this effective co-passivation strategy with PFOA was also illustrated using the Cs/FA/MA-triple cation perovskite that also showed a remarkable improvement in the PCE and moisture stability.<sup>38</sup>

Mostly bulky spacer cations used for the defect passivation at the grain boundaries hinder carrier transport.<sup>39</sup> In an attempt to reduce defects at the grain boundaries without affecting the carrier mobility, Chen and team explored a highly conducting and hydrophobic fluorinated perylenediimide molecule, *N,N'*-bis-(1,1,1,2,2,2,3,3,3,4,4-nonafluorododecan-6-yl)-perylene-3,4,9,10-tetracarboxylic diimide, named F-PDI, to passivate the grain boundaries of  $\text{MAPbI}_3$  and  $\text{Cs}_{0.05}(\text{FA}_{0.83}\text{MA}_{0.17})_{0.95}\text{Pb}(\text{Br}_{0.17}\text{I}_{0.83})_3$ -based perovskites.<sup>37</sup> Fluorine substitution of perylenediimide is known to overcome the solubility issues of the parent molecule.<sup>126</sup> Here, the chelation formed between the carbonyl group of F-PDI and non-coordinated  $\text{Pb}^{2+}$  could passivate defects at the perovskite surface and also at the grain boundaries. Further, hydrogen bonding was observed between the fluorine atoms of F-PDI and hydrogen atoms of MA, that could hinder thermally assisted ion migration leading to higher thermal stability. Besides, the F-PDI-incorporated perovskite had a larger grain size, a defect-free structure and improved crystallinity. Restriction of the F-PDI molecule towards the grain boundaries or surface was confirmed from the XRD analysis. Also, the influence of F-PDI on the absorption properties of the parent perovskite was minimal. Enhancement in the PL intensity and lifetime due to the passivation of grain boundaries upon doping with F-PDI was observed. Further, PCE improved to 18.28% and 19.26%, respectively, for  $\text{MAPbI}_3$  and  $\text{Cs}_{0.05}(\text{FA}_{0.83}\text{MA}_{0.17})_{0.95}\text{Pb}(\text{Br}_{0.17}\text{I}_{0.83})_3$ -based perovskites post-passivation. Substantially, low hysteresis for the F-PDI incorporated devices than pristine was noted. The hindered movement of the iodide ion upon F-PDI passivation was confirmed from the time-of-flight secondary ion mass

spectroscopy (TOF-SIMS). Higher hole and electron mobility for F-PDI incorporated devices was obtained, suggesting improved charge transport upon defect passivation at the grain boundaries.<sup>37</sup> Upon exposure to 50% RH for 30 days, F-PDI passivated devices retained 80% of PCE. Besides moisture stability, F-PDI incorporated films exhibited a higher resistance to thermal decomposition than the pristine perovskite due to the inhibition of ion migration at the grain boundaries. Furthermore, upon annealing to a higher temperature of  $160^\circ\text{C}$ , F-PDI passivated films exhibited minimal decomposition to  $\text{PbI}_2$ , as indicated from the elemental depth profiling.<sup>37</sup> The hydrogen bonding between F-PDI and the MA cation prohibited MA ion migration, rendering higher thermal stability (*cf.* Fig. 30).<sup>39</sup>

The aliphatic fluorinated spacer pentafluoropropylammonium iodide (PFPAI) was explored by Mathews *et al.* for surface passivation, band gap tuning and imparting superhydrophobic properties to the MA/FA/CS-triple cation perovskite.<sup>131</sup> Retention of the intrinsic structure of the triple cation perovskite and slight expansion of the lattice upon passivation with fluorinated salt were confirmed from the XRD. An enhanced water contact angle up to  $66^\circ$  compared to the pristine 3D-triple cation perovskite revealed superhydrophobic properties imparted by passivation with the fluorinated cation. The inhibition of  $\delta$ -phase formation of  $\text{FAPbI}_3$  was confirmed from the absence of a diffraction peak in XRD at  $11.7^\circ$  upon passivation. Also, band gap narrowing could be seen upon bromide to iodide substitution after passivation and was confirmed from the UV-Vis studies (*cf.* Fig. 31).<sup>131</sup> A reduced peak area in the XPS spectrum for the binding energy of 69.6 eV for Br (3d) and an increased peak area for binding energies of 631.3 eV and 620 eV for I (3d) core peaks confirmed bromide to iodide substitution upon passivation with PFPAI. An enhanced

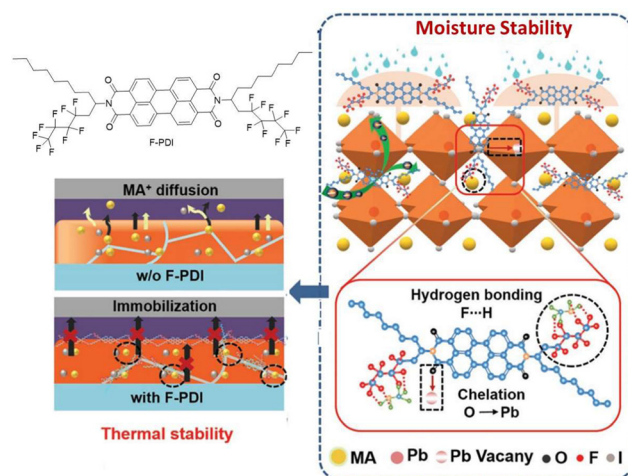


Fig. 30 The mitigation of ion-migration in the F-PDI passivated perovskite due to the hydrogen bonding between the fluorine atom of the F-decorated PDI molecule and the MA cation. Also, illustrated here are interactions rendering moisture tolerance upon F-PDI passivation.<sup>37</sup> Reproduced with permission from ref. 37. Copyright 2019, John Wiley and Sons.

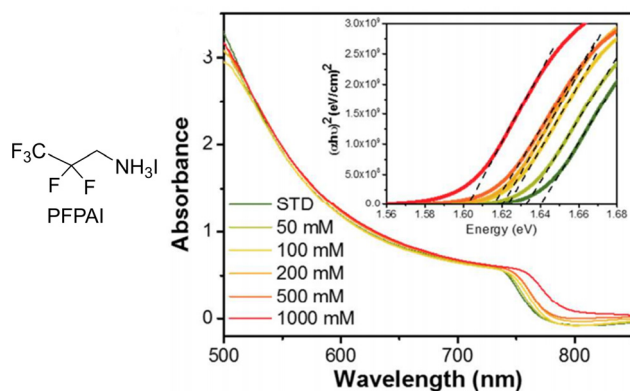


Fig. 31 UV-Vis spectra showing the tuning of the band gap upon passivation with different concentrations of PFPAl.<sup>131</sup> Reproduced with permission from ref. 131. Copyright 2018, American Chemical Society.

PCE of 16.6% for the passivated film compared to 14.6% for the non-passivated film indicated a reduction in non-radiative recombination and trap states upon PFPAl passivation, which was further confirmed from the impedance study. Upon PFPAl passivation, unencapsulated devices retained 90% of the initial PCE upon exposure to 55% RH for 169 days.<sup>131</sup>

Nazeeruddin and co-workers explored aliphatic spacer CF<sub>3</sub>EAI (1,1,1-trifluoroethyl ammonium iodide) as a passivator to enhance the in-operando stability of MAPbI<sub>3</sub>.<sup>128</sup> Improved morphology compared to the pristine MAPbI<sub>3</sub> film was observed for 3 mol% doping with CF<sub>3</sub>EAI. A doping ratio of more than 3 mol% of CF<sub>3</sub>EAI led to a reduction in the film crystallinity as confirmed from the XRD. A maximum PCE of 18% was observed when the blending ratio of CF<sub>3</sub>EAI was limited to 3 mol%. However, pristine MAPbI<sub>3</sub> exhibited a lower PCE of 15%.<sup>128</sup> The water contact angle measurement showed a 5° higher value for the 3% doped than the pristine film. After exposure to air for 120 days, the device with 3 mol% CF<sub>3</sub>EAI retained 92% of initial PCE. Under similar storage conditions, PCE dropped to 21% of the initial value for the pristine perovskite device.<sup>128</sup>

The concept of coating the perovskite surface with photo-curable fluorinated polymers containing a luminescent dye to impart thermal and moisture resistance was explored by Gerbaldi and co-workers.<sup>127</sup> A 1–2 wt% luminescent dye F-Violet 570 doped photocurable fluorinated polymer absorbed sunlight in the UV region and transmitted the rest of the light in the visible range to the underlying perovskite, thus slowing the process of UV-light triggered photodecomposition of the underlying perovskite layer. Here, the device of polymer-coated perovskite exhibited ~15.5% PCE without hysteresis and also showed extraordinary stability to water. Remarkably, the PCE was not changed even upon dipping in water for a period of 1 day for the front- and back-side polymer passivated perovskite device.<sup>127</sup>

Effective passivation using peripherally fluorinated graphene nanoplates (EFGnPs-F) for inverted perovskite PV devices was demonstrated by Kim and co-workers.<sup>85</sup> EFGnPs-F was synthesized from peripheral fluorination of graphite with XeF<sub>2</sub> using the ball milling method. The passivating EFGnPs-F layer was

deposited over the PCBM layer in the MAPbI<sub>3</sub>-based perovskite device, which tremendously improved the water repellent features.<sup>107</sup>

Also, fluorinated-[6,6]-phenyl-C<sub>61</sub>-butyric acid methyl esters (3F/5F-PC<sub>61</sub>BM) with improved solubility in DMF than PC<sub>61</sub>BM were explored as additives for engineering the MAPbI<sub>3</sub>-based bulk-heterojunction PV device (*cf.* Fig. 32).<sup>132,133</sup> In this study, the lower solubility in DMF, an issue associated with an earlier developed fluorine-based fullerene additive DF-C<sub>60</sub>, was addressed by introducing substituents trifluoroethyl-(3F-PC<sub>61</sub>BM) or penta-fluoropropyl-(5F-PC<sub>61</sub>BM) onto PC<sub>61</sub>BM (*cf.* Fig. 32).<sup>134</sup> A smooth pin-hole free morphology with out-of-plane lattice growth led by blending with 0.1% 3F-PC<sub>61</sub>BM allowed an improved PCE of 16.17% in inverted architecture compared with 14.12% PCE obtained for the control device without any additive. Also, faster carrier segregation in 0.1% 3F-PC<sub>61</sub>BM blended MAPbI<sub>3</sub> compared to the pristine was confirmed from the PL and TRPL studies. Extended stability of the unencapsulated device with retention of 80% of initial PCE post 550 h could be seen upon blending 0.1% 3F-PC<sub>61</sub>BM. However, a 20% PCE drop for the control device was evident within 240 h.<sup>132</sup> Nevertheless, passivation with 5F-PC<sub>61</sub>BM was not effective due to self-sorting upon blending with the perovskite.<sup>132</sup>

Along a similar line, fluorine-decorated isoxazolino[60]-fullerenes (IS-1 and IS-2) and pyrazolino[60]fullerenes (PI-1 and PI-2) were blended with MAPbI<sub>3</sub> to develop ETL-free PV devices (*cf.* Fig. 32).<sup>135</sup> These fluorine-based fullerenes displayed strong n-type character due to their electron-deficient nature and could improve electron transport. Among the series, the deepest LUMO energy of *ca.* 4.08 eV was observed for PI-2. The best PV performance of 12.7% was obtained for the IS-2 blended perovskite device, followed by 11.8% for IS-1 and 11.7% observed for PI-2 blended perovskite devices. Nevertheless, PI-1 could not be explored for PV fabrication due to the poor solubility in DMF. Upon further solvent engineering with *o*-xylene, PCE could be further improved to 14.3% for the IS-2 blended perovskite device. However, the fullerene-free perovskite device exhibited a much lower PCE of 10.5%. Also, these fluorinated fullerene blended perovskite devices demonstrated photostability upon exposure to continuous AM1.5G solar irradiation.<sup>135</sup>

A pyridine-functionalized fullerene molecule, named C<sub>60</sub>-PyF15, when explored as an additive for engineering MAPbI<sub>3</sub> led to a remarkable PCE of 20.1% in inverted architecture (*cf.* Fig. 32).<sup>136</sup> The PCE obtained for the control device without the additive was 17.09%. This high PCE obtained with C<sub>60</sub>-PyF15 engineering was the result of the double-site passivation effect led by the coordination of the pyridine motif of C<sub>60</sub>-PyF15 to uncoordinated Pb<sup>2+</sup> sites, as well as the hydrogen bonding between the fluorine atoms of the additive and ammonium groups of MAPbI<sub>3</sub>, which were confirmed from the XPS and NMR studies. The doped C<sub>60</sub>-PyF15 molecules reduced the trap state density, enhanced the carrier segregation and improved the hole and electron mobility in the perovskite film. Also, improved crystallinity with out-of-plane lattice growth for the C<sub>60</sub>-PyF15 included film of MAPbI<sub>3</sub> was evident from the XRD and GIWAX studies. This enhanced crystallinity was the result

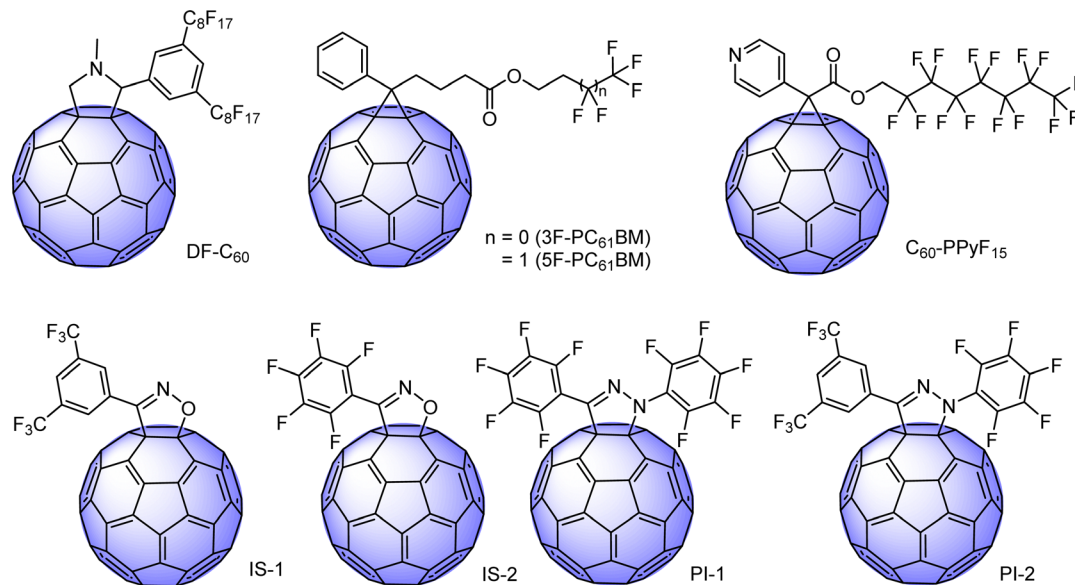


Fig. 32 Designs of fluorine-based fullerenes blended with perovskites for PV applications.<sup>132–136</sup>

of C<sub>60</sub>-PyF<sub>15</sub> molecules acting as the nucleation sites for the growth of the perovskite lattice due to their low surface energy, which also increased the grain size as well as reduced the grain boundaries. Furthermore, C<sub>60</sub>-PyF<sub>15</sub> manifested double-site passivation could prevent the escape of MA<sup>+</sup> after heating, and improved the thermal stability as indicated by the retention of 81% of initial PCE upon heating the C<sub>60</sub>-PyF<sub>15</sub> passivated device at 85 °C for 660 h. However, the PCE of the control and corresponding hydrogen analogue C<sub>60</sub>-PyH<sub>15</sub>-based devices dropped to 43% and 55% of the initial values, respectively, upon exposure to similar heat stress. Likewise, the C<sub>60</sub>-PyF<sub>15</sub> passivated unencapsulated device retained 85% of initial PCE upon exposure to 35% RH under ambient conditions compared to 69% of PCE retained by the C<sub>60</sub>-PyH<sub>15</sub> included device.<sup>136</sup>

## 7. Outlook and conclusions

From the above discussions, fluorine-tethered spacers can substantially manoeuvre the properties of RP-, DJ- and 2D/3D-bilayer perovskites towards the improvement of PV performance. Due to the influence of the fluorine atom of the spacer, lower exciton binding energy, lower non-radiative recombination, inhibition of ion migration, more aligned ordered phase distribution and effective defect passivation could be attained, besides in-operando stability. All these features led to fluorine-based spacers being superior to their hydrogen counterparts in the realm of perovskites, particularly towards solar-light harvesting. By now an efficiency of 22.7% has already been manifested with 2D/3D-bilayer perovskites using 2,4,5-F<sub>3</sub>PEAI, opening further room for attaining a value even closer to the Shockley–Queisser limit.<sup>35</sup> Thus, the approach of minor structure tailoring involving swapping hydrogen with fluorine may be an attractive strategy to integrate totally new exotic properties into the perovskites without compromising material efficiency. As can be

conceived from the covered literature, substantial developments have been already showcased by exploring fluorine-based spacers for PV applications. Nevertheless, still a lot of potential exists to confer new properties to the perovskite using fluorinated spacers not only in the realm of PV applications, but also towards different other applications, like LED, lasing or photodetectors.<sup>137–139</sup> Also, fluorinated spacers can be structurally engineered in a myriad of ways for exploring new perovskites. Some of the ways the structural tuning of fluorinated spacers could be realized for developing novel and more efficient perovskites for PV applications are as follows:

(i) Photo-crosslinkable fluorine-tethered molecules could be one of the important kinds of spacers to be explored to integrate extraordinary stability into the perovskites. These kinds of spacers besides offering high ambient stability would possibly contribute to vertical lattice alignment in the perovskites affected by the combined influence of the fluorine atom and photo-crosslinking.<sup>86</sup>

(ii) To the best of our knowledge, 2022 Nobel prize winning concepts of click chemistry to structurally and functionally engineer perovskites have not been explored so far.<sup>140,141</sup> Exploration of fluorine-tethered spacers with suitable functional groups that could exhibit molecular recognition to allow topochemical click reactions upon attaining a particular spatial proximity within a perovskite lattice would be one of the exceptionally challenging and novel problems to investigate. Such topochemical click reactions have the potential to lock or polymerize spacers and might integrate novel properties heretofore unknown in the realm of perovskites. Also, interesting would be to fundamentally understand in what ways such topochemical click reaction-induced locking of spacers could tailor the properties of perovskites.

(iii) Fluorinated spacers with enhanced conjugation length also could remarkably improve the carrier segregation and out-of-plane transport within the perovskite and would be another

important class of molecules to take up for perovskite synthesis, when limitations with the conventional perovskites are to be overcome.

(iv) Recipe optimization for scale-up to develop unencapsulated perovskite PV devices based on various fluorine-based spacers is another important avenue that needs attention. Moreover, testing of the scaled-up PV panels under ambient environmental conditions and prolonged operation would be significant to study, when the suitability of the recipes based on fluorinated spacers for practical applications is envisioned.

(v) Additionally, the effects of fluorinated spacers could be explored in the domains of environmental friendly Pb-free perovskites, that would possibly lead towards tremendous material efficiency and stability, so that the dream of superseding the Si-based PV market with efficient perovskite panels will not be so far.<sup>142</sup>

(vi) Similarly, a key concept of  $\sigma$ -hole interactions towards halogen bonding within the perovskite lattice could be explored using fluorinated spacers, which would indeed be very exciting.<sup>143,144</sup>

## Author contributions

IN envisaged the idea of the review. IN collected the literature. IN, GM and KNP wrote the review. AS and HS helped with editing. The manuscript was approved by all the authors before submission.

## Conflicts of interest

There are no conflicts to declare.

## Acknowledgements

I. N. acknowledges financial support from the Department of Science and Technology (DST), Government of India (DST/INT/ISR/P-26/2020(G)). K. N. P. thanks CSIR, India, for CSIR-SRA fellowship. GM thanks DST, Government of India, for the project fellowship. A. S. thanks DST-INSPIRE for JRF, and AcSIR Ghaziabad for PhD registration. H. S. thanks CSIR, India, for the project fellowship.

## Notes and references

- Satellite data shows entire Conger ice shelf has collapsed in Antarctica, <https://www.theguardian.com/world/2022/mar/25/satellite-data-shows-entire-conger-ice-shelf-has-collapsed-in-antarctica>.
- K. Zheng and T. Pullerits, *J. Phys. Chem. Lett.*, 2019, **10**, 5881–5885.
- A. Krishna, S. Gottis, M. K. Nazeeruddin and F. Sauvage, *Adv. Funct. Mater.*, 2019, **29**, 1806482.
- J. Gebhardt and A. M. Rappe, *Adv. Mater.*, 2019, **31**, 1802697.
- J. M. Frost, K. T. Butler, F. Brivio, C. H. Hendon, M. van Schilfgaarde and A. Walsh, *Nano Lett.*, 2014, **14**, 2584–2590.
- L. Mao, C. C. Stoumpos and M. G. Kanatzidis, *J. Am. Chem. Soc.*, 2019, **141**, 1171–1190.
- A. Kojima, K. Teshima, Y. Shirai and T. Miyasaka, *J. Am. Chem. Soc.*, 2009, **131**, 6050–6051.
- H.-S. Kim, C.-R. Lee, J.-H. Im, K.-B. Lee, T. Moehl, A. Marchioro, S.-J. Moon, R. Humphry-Baker, J.-H. Yum, J. E. Moser, M. Grätzel and N.-G. Park, *Sci. Rep.*, 2012, **2**, 591.
- H. Min, D. Y. Lee, J. Kim, G. Kim, K. S. Lee, J. Kim, M. J. Paik, Y. K. Kim, K. S. Kim, M. G. Kim, T. J. Shin and S. Il Seok, *Nature*, 2021, **598**, 444–450.
- National Renewable Energy Laboratory (NREL), <https://www.nrel.gov/pv/assets/pdfs/best-research-cell-efficiencies.pdf>.
- X. Jiang, S. Chen, Y. Li, L. Zhang, N. Shen, G. Zhang, J. Du, N. Fu and B. Xu, *ACS Appl. Mater. Interfaces*, 2021, **13**, 2558–2565.
- S. Paek, C. Roldán-Carmona, K. T. Cho, M. Franckevičius, H. Kim, H. Kanda, N. Drigo, K. Lin, M. Pei, R. Gegevičius, H. J. Yun, H. Yang, P. A. Schouwink, C. Corminboeuf, A. M. Asiri and M. K. Nazeeruddin, *Adv. Sci.*, 2020, **7**, 2001014.
- T. Wu, D. Cui, X. Liu, X. Meng, Y. Wang, T. Noda, H. Segawa, X. Yang, Y. Zhang and L. Han, *Sol. RRL*, 2020, **4**, 2000240.
- S. De Wolf, J. Holovsky, S.-J. Moon, P. Löper, B. Niesen, M. Ledinsky, F.-J. Haug, J.-H. Yum and C. Ballif, *J. Phys. Chem. Lett.*, 2014, **5**, 1035–1039.
- T. C. Sum, N. Mathews, G. Xing, S. S. Lim, W. K. Chong, D. Giovanni and H. A. Dewi, *Acc. Chem. Res.*, 2016, **49**, 294–302.
- E. L. Unger, L. Kegelmann, K. Suchan, D. Sörell, L. Korte and S. Albrecht, *J. Mater. Chem. A*, 2017, **5**, 11401–11409.
- B. M. Lefler, S. J. May and A. T. Fafarman, *Phys. Rev. Mater.*, 2020, **4**, 120301.
- P. Docampo, S. Guldin, T. Leijtens, N. K. Noel, U. Steiner and H. J. Snaith, *Adv. Mater.*, 2014, **26**, 4013–4030.
- K. X. Steirer, P. Schulz, G. Teeter, V. Stevanovic, M. Yang, K. Zhu and J. J. Berry, *ACS Energy Lett.*, 2016, **1**, 360–366.
- G. Xing, N. Mathews, S. Sun, S. S. Lim, Y. M. Lam, M. Grätzel, S. Mhaisalkar and T. C. Sum, *Science*, 2013, **342**, 344–347.
- S. D. Stranks, G. E. Eperon, G. Grancini, C. Menelaou, M. J. P. Alcocer, T. Leijtens, L. M. Herz, A. Petrozza and H. J. Snaith, *Science*, 2013, **342**, 341–344.
- N. K. Tailor, Y. R. Ranjan, S. Ranjan, T. Sharma, A. Singh, A. Garg, K. S. Nalwa, R. K. Gupta and S. Satapathi, *J. Mater. Chem. A*, 2021, **9**, 21551–21575.
- Q. Guo, C. Li, W. Qiao, S. Ma, F. Wang, B. Zhang, L. Hu, S. Dai and Z. Tan, *Energy Environ. Sci.*, 2016, **9**, 1486–1494.
- H. J. Snaith, *J. Phys. Chem. Lett.*, 2013, **4**, 3623–3630.
- Q. Chen, H. Zhou, Z. Hong, S. Luo, H.-S. Duan, H.-H. Wang, Y. Liu, G. Li and Y. Yang, *J. Am. Chem. Soc.*, 2014, **136**, 622–625.
- A. H. Slavney, R. W. Smaha, I. C. Smith, A. Jaffe, D. Umeyama and H. I. Karunadasa, *Inorg. Chem.*, 2017, **56**, 46–55.



- 27 X. Li, M. Ibrahim Dar, C. Yi, J. Luo, M. Tschumi, S. M. Zakeeruddin, M. K. Nazeeruddin, H. Han and M. Grätzel, *Nat. Chem.*, 2015, **7**, 703–711.
- 28 Y. Zhou, Y. Yin, X. Zuo, L. Wang, T.-D. Li, Y. Xue, A. Subramanian, Y. Fang, Y. Guo, Z. Yang, M. Cotlet, C.-Y. Nam and M. H. Rafailovich, *Chem. Mater.*, 2021, **33**, 6120–6135.
- 29 J. Yang, B. D. Siempelkamp, D. Liu and T. L. Kelly, *ACS Nano*, 2015, **9**, 1955–1963.
- 30 G. Niu, X. Guo and L. Wang, *J. Mater. Chem. A*, 2015, **3**, 8970–8980.
- 31 K. T. Cho, Y. Zhang, S. Orlandi, M. Cavazzini, I. Zimmermann, A. Lesch, N. Tabet, G. Pozzi, G. Grancini and M. K. Nazeeruddin, *Nano Lett.*, 2018, **18**, 5467–5474.
- 32 T. Leijtens, G. E. Eperon, S. Pathak, A. Abate, M. M. Lee and H. J. Snaith, *Nat. Commun.*, 2013, **4**, 2885.
- 33 S.-W. Lee, S. Kim, S. Bae, K. Cho, T. Chung, L. E. Mundt, S. Lee, S. Park, H. Park, M. C. Schubert, S. W. Glunz, Y. Ko, Y. Jun, Y. Kang, H.-S. Lee and D. Kim, *Sci. Rep.*, 2016, **6**, 38150.
- 34 H.-S. Kim, A. Hagfeldt and N.-G. Park, *Chem. Commun.*, 2019, **55**, 1192–1200.
- 35 L. Wang, Q. Zhou, Z. Zhang, W. Li, X. Wang, Q. Tian, X. Yu, T. Sun, J. Wu, B. Zhang and P. Gao, *J. Energy Chem.*, 2022, **64**, 179–189.
- 36 A. Abate, M. Saliba, D. J. Hollman, S. D. Stranks, K. Wojciechowski, R. Avolio, G. Grancini, A. Petrozza and H. J. Snaith, *Nano Lett.*, 2014, **14**, 3247–3254.
- 37 J. Yang, C. Liu, C. Cai, X. Hu, Z. Huang, X. Duan, X. Meng, Z. Yuan, L. Tan and Y. Chen, *Adv. Energy Mater.*, 2019, **9**, 1900198.
- 38 P. Guo, Q. Ye, X. Yang, J. Zhang, F. Xu, D. Shchukin, B. Wei and H. Wang, *J. Mater. Chem. A*, 2019, **7**, 2497–2506.
- 39 J. Y. Ye, J. Tong, J. Hu, C. Xiao, H. Lu, S. P. Dunfield, D. H. Kim, X. Chen, B. W. Larson, J. Hao, K. Wang, Q. Zhao, Z. Chen, H. Hu, W. You, J. J. Berry, F. Zhang and K. Zhu, *Sol. RRL*, 2020, **4**, 2000082.
- 40 Y. Shao, Y. Fang, T. Li, Q. Wang, Q. Dong, Y. Deng, Y. Yuan, H. Wei, M. Wang, A. Gruverman, J. Shield and J. Huang, *Energy Environ. Sci.*, 2016, **9**, 1752–1759.
- 41 Y. Li, L. Ji, R. Liu, C. Zhang, C. H. Mak, X. Zou, H.-H. Shen, S.-Y. Leu and H.-Y. Hsu, *J. Mater. Chem. A*, 2018, **6**, 12842–12875.
- 42 D. Wei, F. Ma, R. Wang, S. Dou, P. Cui, H. Huang, J. Ji, E. Jia, X. Jia, S. Sajid, A. M. Elseman, L. Chu, Y. Li, B. Jiang, J. Qiao, Y. Yuan and M. Li, *Adv. Mater.*, 2018, **30**, 1707583.
- 43 M. Bag, L. A. Renna, R. Y. Adhikari, S. Karak, F. Liu, P. M. Lahti, T. P. Russell, M. T. Tuominen and D. Venkataraman, *J. Am. Chem. Soc.*, 2015, **137**, 13130–13137.
- 44 D. Wang, M. Wright, N. K. Elumalai and A. Uddin, *Sol. Energy Mater. Sol. Cells*, 2016, **147**, 255–275.
- 45 Y. Jiang, M. Cui, S. Li, C. Sun, Y. Huang, J. Wei, L. Zhang, M. Lv, C. Qin, Y. Liu and M. Yuan, *Nat. Commun.*, 2021, **12**, 336.
- 46 L. N. Quan, M. Yuan, R. Comin, O. Voznyy, E. M. Beauregard, S. Hoogland, A. Buin, A. R. Kirmani, K. Zhao, A. Amassian, D. H. Kim and E. H. Sargent, *J. Am. Chem. Soc.*, 2016, **138**, 2649–2655.
- 47 M. A. Hope, T. Nakamura, P. Ahlawat, A. Mishra, M. Cordova, F. Jahanbakhshi, M. Mladenović, R. Runjhun, L. Merten, A. Hinderhofer, B. I. Carlsen, D. J. Kubicki, R. Gershoni-Poranne, T. Schneeberger, L. C. Carbone, Y. Liu, S. M. Zakeeruddin, J. Lewinski, A. Hagfeldt, F. Schreiber, U. Rothlisberger, M. Grätzel, J. V. Milić and L. Emsley, *J. Am. Chem. Soc.*, 2021, **143**, 1529–1538.
- 48 Y. Xu, M. Wang, Y. Lei, Z. Ci and Z. Jin, *Adv. Energy Mater.*, 2020, **10**, 2002558.
- 49 H. Park, S. Kumar, S. Chawla and F. El-Mellouhi, *Molecules*, 2021, **26**, 6184.
- 50 J. Hu, I. W. H. Oswald, S. J. Stuard, M. M. Nahid, N. Zhou, O. F. Williams, Z. Guo, L. Yan, H. Hu, Z. Chen, X. Xiao, Y. Lin, Z. Yang, J. Huang, A. M. Moran, H. Ade, J. R. Neilson and W. You, *Nat. Commun.*, 2019, **10**, 1276.
- 51 H. Lai, D. Lu, Z. Xu, N. Zheng, Z. Xie and Y. Liu, *Adv. Mater.*, 2020, **32**, 2001470.
- 52 M. C. Gélvez-Rueda, M. B. Fridriksson, R. K. Dubey, W. F. Jager, W. van der Stam and F. C. Grozema, *Nat. Commun.*, 2020, **11**, 1901.
- 53 Y. Liu, S. Akin, L. Pan, R. Uchida, N. Arora, J. V. Milić, A. Hinderhofer, F. Schreiber, A. R. Uhl, S. M. Zakeeruddin, A. Hagfeldt, M. I. Dar and M. Grätzel, *Sci. Adv.*, 2019, **5**, eaaw2543.
- 54 F. Zhang, H. Lu, J. Tong, J. J. Berry, M. C. Beard and K. Zhu, *Energy Environ. Sci.*, 2020, **13**, 1154–1186.
- 55 J. Xi, I. Spanopoulos, K. Bang, J. Xu, H. Dong, Y. Yang, C. D. Malliakas, J. M. Hoffman, M. G. Kanatzidis and Z. Wu, *J. Am. Chem. Soc.*, 2020, **142**, 19705–19714.
- 56 I. C. Smith, E. T. Hoke, D. Solis-Ibarra, M. D. McGehee and H. I. Karunadasa, *Angew. Chem., Int. Ed.*, 2014, **53**, 11232–11235.
- 57 Q. Zhou, L. Liang, J. Hu, B. Cao, L. Yang, T. Wu, X. Li, B. Zhang and P. Gao, *Adv. Energy Mater.*, 2019, **9**, 1802595.
- 58 M.-H. Tremblay, J. Bacsá, B. Zhao, F. Pulvirenti, S. Barlow and S. R. Marder, *Chem. Mater.*, 2019, **31**, 6145–6153.
- 59 Q. Li, Y. Dong, G. Lv, T. Liu, D. Lu, N. Zheng, X. Dong, Z. Xu, Z. Xie and Y. Liu, *ACS Energy Lett.*, 2021, **6**, 2072–2080.
- 60 J. Shi, Y. Gao, X. Gao, Y. Zhang, J. Zhang, X. Jing and M. Shao, *Adv. Mater.*, 2019, **31**, 1901673.
- 61 H. Pan, X. Zhao, X. Gong, Y. Shen and M. Wang, *J. Phys. Chem. Lett.*, 2019, **10**, 1813–1819.
- 62 J. Hu, I. W. H. Oswald, H. Hu, S. J. Stuard, M. M. Nahid, L. Yan, Z. Chen, H. Ade, J. R. Neilson and W. You, *ACS Mater. Lett.*, 2019, **1**, 171–176.
- 63 T. Liu, J. Guo, D. Lu, Z. Xu, Q. Fu, N. Zheng, Z. Xie, X. Wan, X. Zhang, Y. Liu and Y. Chen, *ACS Nano*, 2021, **15**, 7811–7820.
- 64 W. Fu, H. Liu, X. Shi, L. Zuo, X. Li and A. K.-Y. Jen, *Adv. Funct. Mater.*, 2019, **29**, 1900221.
- 65 G. Lv, L. Li, D. Lu, Z. Xu, Y. Dong, Q. Li, Z. Chang, W.-J. Yin and Y. Liu, *Nano Lett.*, 2021, **21**, 5788–5797.
- 66 L. Glasser, *Inorg. Chem.*, 2017, **56**, 8920–8925.

- 67 M. Kepenekian, B. Traore, J.-C. Blancon, L. Pedesseau, H. Tsai, W. Nie, C. C. Stoumpos, M. G. Kanatzidis, J. Even, A. D. Mohite, S. Tretiak and C. Katan, *Nano Lett.*, 2018, **18**, 5603–5609.
- 68 M. Yang, T. Tian, W. Feng, L. Wang and W.-Q. Wu, *Acc. Mater. Res.*, 2021, **2**, 1141–1155.
- 69 H. Zhang, M. K. Nazeeruddin and W. C. H. Choy, *Adv. Mater.*, 2019, **31**, 1805702.
- 70 T. Niu, Q. Xue and H.-L. Yip, *Nanophotonics*, 2021, **10**, 2069–2102.
- 71 X. Zhang, G. Wu, W. Fu, M. Qin, W. Yang, J. Yan, Z. Zhang, X. Lu and H. Chen, *Adv. Energy Mater.*, 2018, **8**, 1702498.
- 72 Y. Li, J. V. Milić, A. Ummadisingu, J.-Y. Seo, J.-H. Im, H.-S. Kim, Y. Liu, M. I. Dar, S. M. Zakeeruddin, P. Wang, A. Hagfeldt and M. Grätzel, *Nano Lett.*, 2019, **19**, 150–157.
- 73 G. Yan, G. Sui, W. Chen, K. Su, Y. Feng and B. Zhang, *Chem. Mater.*, 2022, **34**, 3346–3356.
- 74 Z. Xu, D. Lu, F. Liu, H. Lai, X. Wan, X. Zhang, Y. Liu and Y. Chen, *ACS Nano*, 2020, **14**, 4871–4881.
- 75 Y. Li, H. Cheng, K. Zhao and Z.-S. Wang, *ACS Appl. Mater. Interfaces*, 2019, **11**, 37804–37811.
- 76 B. Primera Darwich, N. Guijarro, H. Cho, L. Yao, L. Monnier, P. Schouwink, M. Mensi, J. Yum and K. Sivula, *ChemSusChem*, 2021, **14**, 3001–3009.
- 77 Y. Yan, S. Yu, A. Honarfar, T. Pullerits, K. Zheng and Z. Liang, *Adv. Sci.*, 2019, **6**, 1900548.
- 78 L. Mao, W. Ke, L. Pedesseau, Y. Wu, C. Katan, J. Even, M. R. Wasielewski, C. C. Stoumpos and M. G. Kanatzidis, *J. Am. Chem. Soc.*, 2018, **140**, 3775–3783.
- 79 M. E. F. Bouduban, V. I. E. Queloz, V. M. Caselli, K. T. Cho, A. R. Kirmani, S. Paek, C. Roldan-Carmona, L. J. Richter, J. E. Moser, T. J. Savenije, M. K. Nazeeruddin and G. Grancini, *J. Phys. Chem. Lett.*, 2019, **10**, 5713–5720.
- 80 Y. Qiu, J. Liang, Z. Zhang, Z. Deng, H. Xu, M. He, J. Wang, Y. Yang, L. Kong and C.-C. Chen, *J. Phys. Chem. C*, 2021, **125**, 1256–1268.
- 81 A. Coriolano, L. Polimeno, M. De Giorgi, F. Todisco, R. Mastria, V. Ardizzone, L. Dominici, D. Ballarini, A. Rizzo, G. Gigli, D. Sanvitto and L. De Marco, *Nanomaterials*, 2021, **11**, 465.
- 82 T. Niu, J. Lu, X. Jia, Z. Xu, M.-C. Tang, D. Barrit, N. Yuan, J. Ding, X. Zhang, Y. Fan, T. Luo, Y. Zhang, D.-M. Smilgies, Z. Liu, A. Amassian, S. Jin, K. Zhao and S. Liu, *Nano Lett.*, 2019, **19**, 7181–7190.
- 83 R. Yang, R. Li, Y. Cao, Y. Wei, Y. Miao, W. L. Tan, X. Jiao, H. Chen, L. Zhang, Q. Chen, H. Zhang, W. Zou, Y. Wang, M. Yang, C. Yi, N. Wang, F. Gao, C. R. McNeill, T. Qin, J. Wang and W. Huang, *Adv. Mater.*, 2018, **30**, 1804771.
- 84 T. M. Koh, J. Huang, I. Neogi, P. P. Boix, S. G. Mhaisalkar and N. Mathews, *ACS Appl. Mater. Interfaces*, 2017, **9**, 28743–28749.
- 85 H. Zheng, X. Dong, W. Wu, G. Liu and X. Pan, *ACS Appl. Mater. Interfaces*, 2022, **14**, 9183–9191.
- 86 A. H. Proppe, M. Wei, B. Chen, R. Quintero-Bermudez, S. O. Kelley and E. H. Sargent, *J. Am. Chem. Soc.*, 2019, **141**, 14180–14189.
- 87 J. Hu, C. Wang, S. Qiu, Y. Zhao, E. Gu, L. Zeng, Y. Yang, C. Li, X. Liu, K. Forberich, C. J. Brabec, M. K. Nazeeruddin, Y. Mai and F. Guo, *Adv. Energy Mater.*, 2020, **10**, 2000173.
- 88 P. Li, Y. Zhang, C. Liang, G. Xing, X. Liu, F. Li, X. Liu, X. Hu, G. Shao and Y. Song, *Adv. Mater.*, 2018, **30**, 1805323.
- 89 Y. Wei, P. Audebert, L. Galmiche, J.-S. Lauret and E. Deleporte, *Materials*, 2014, **7**, 4789–4802.
- 90 K. Reichenbacher, H. I. Süss and J. Hulliger, *Chem. Soc. Rev.*, 2005, **34**, 22–30.
- 91 B. Carsten, J. M. Szarko, H. J. Son, W. Wang, L. Lu, F. He, B. S. Rolczynski, S. J. Lou, L. X. Chen and L. Yu, *J. Am. Chem. Soc.*, 2011, **133**, 20468–20475.
- 92 Q. Zhang, M. A. Kelly, N. Bauer and W. You, *Acc. Chem. Res.*, 2017, **50**, 2401–2409.
- 93 W. Zhu, J. M. Alzola, T. J. Aldrich, K. L. Kohlstedt, D. Zheng, P. E. Hartnett, N. D. Eastham, W. Huang, G. Wang, R. M. Young, G. C. Schatz, M. R. Wasielewski, A. Facchetti, F. S. Melkonyan and T. J. Marks, *ACS Energy Lett.*, 2019, **4**, 2695–2702.
- 94 K. Feng, X. Zhang, Z. Wu, Y. Shi, M. Su, K. Yang, Y. Wang, H. Sun, J. Min, Y. Zhang, X. Cheng, H. Y. Woo and X. Guo, *ACS Appl. Mater. Interfaces*, 2019, **11**, 35924–35934.
- 95 Y. Sakamoto, T. Suzuki, M. Kobayashi, Y. Gao, Y. Fukai, Y. Inoue, F. Sato and S. Tokito, *J. Am. Chem. Soc.*, 2004, **126**, 8138–8140.
- 96 F. Babudri, G. M. Farinola, F. Naso and R. Ragni, *Chem. Commun.*, 2007, 1003–1022.
- 97 T. Kamata, H. Sasabe, Y. Watanabe, D. Yokoyama, H. Katagiri and J. Kido, *J. Mater. Chem. C*, 2016, **4**, 1104–1110.
- 98 S. Dai, F. Zhao, Q. Zhang, T.-K. Lau, T. Li, K. Liu, Q. Ling, C. Wang, X. Lu, W. You and X. Zhan, *J. Am. Chem. Soc.*, 2017, **139**, 1336–1343.
- 99 P.-P. Shi, S.-Q. Lu, X.-J. Song, X.-G. Chen, W.-Q. Liao, P.-F. Li, Y.-Y. Tang and R.-G. Xiong, *J. Am. Chem. Soc.*, 2019, **141**, 18334–18340.
- 100 Q. Zhou, C. Zuo, Z. Zhang, P. Gao and L. Ding, *J. Semicond.*, 2022, **43**, 010202.
- 101 Z. Wang, Q. Wei, X. Liu, L. Liu, X. Tang, J. Guo, S. Ren, G. Xing, D. Zhao and Y. Zheng, *Adv. Funct. Mater.*, 2021, **31**, 2008404.
- 102 F. El-Mellouhi, S. N. Rashkeev, A. Marzouk, L. Kabalan, A. Belaidi, B. Merzougui, N. Tabet and F. H. Alharbi, *J. Mater. Chem. C*, 2019, **7**, 5299–5306.
- 103 A. Shokri, X.-B. Wang and S. R. Kass, *J. Am. Chem. Soc.*, 2013, **135**, 9525–9530.
- 104 K. Kikuchi, Y. Takeoka, M. Rikukawa and K. Sanui, *Curr. Appl. Phys.*, 2004, **4**, 599–602.
- 105 C. Lermer, S. T. Birkhold, I. L. Moudrakovski, P. Mayer, L. M. Schoop, L. Schmidt-Mende and B. V. Lotsch, *Chem. Mater.*, 2016, **28**, 6560–6566.
- 106 V. H. Dalvi and P. J. Rossky, *Proc. Natl. Acad. Sci. U. S. A.*, 2010, **107**, 13603–13607.
- 107 G.-H. Kim, H. Jang, Y. J. Yoon, J. Jeong, S. Y. Park, B. Walker, I.-Y. Jeon, Y. Jo, H. Yoon, M. Kim, J.-B. Baek, D. S. Kim and J. Y. Kim, *Nano Lett.*, 2017, **17**, 6385–6390.

- 108 M. Salado, F. J. Ramos, V. M. Manzanares, P. Gao, M. K. Nazeeruddin, P. J. Dyson and S. Ahmad, *ChemSusChem*, 2016, **9**, 2708–2714.
- 109 J. Li, T. Bu, Z. Lin, Y. Mo, N. Chai, X. Gao, M. Ji, X.-L. Zhang, Y.-B. Cheng and F. Huang, *Chem. Eng. J.*, 2021, **405**, 126712.
- 110 Y. Wei, P. Audebert, L. Galmiche, J.-S. Lauret and E. Deleporte, *J. Phys. D: Appl. Phys.*, 2013, **46**, 135105.
- 111 I. García-Benito, C. Quarti, V. I. E. Queloz, S. Orlandi, I. Zimmermann, M. Cavazzini, A. Lesch, S. Marras, D. Beljonne, G. Pozzi, M. K. Nazeeruddin and G. Grancini, *Chem. Mater.*, 2018, **30**, 8211–8220.
- 112 N. Li, S. Tao, Y. Chen, X. Niu, C. K. Onwudinanti, C. Hu, Z. Qiu, Z. Xu, G. Zheng, L. Wang, Y. Zhang, L. Li, H. Liu, Y. Lun, J. Hong, X. Wang, Y. Liu, H. Xie, Y. Gao, Y. Bai, S. Yang, G. Brocks, Q. Chen and H. Zhou, *Nat. Energy*, 2019, **4**, 408–415.
- 113 F. Zhang, D. H. Kim, H. Lu, J.-S. Park, B. W. Larson, J. Hu, L. Gao, C. Xiao, O. G. Reid, X. Chen, Q. Zhao, P. F. Ndione, J. J. Berry, W. You, A. Walsh, M. C. Beard and K. Zhu, *J. Am. Chem. Soc.*, 2019, **141**, 5972–5979.
- 114 D. B. Mitzi, C. D. Dimitrakopoulos and L. L. Kosbar, *Chem. Mater.*, 2001, **13**, 3728–3740.
- 115 D. B. Mitzi, D. R. Medeiros and P. R. L. Malenfant, *Inorg. Chem.*, 2002, **41**, 2134–2145.
- 116 Z. Xu and D. B. Mitzi, *Chem. Mater.*, 2003, **15**, 3632–3637.
- 117 I. García-Benito, C. Quarti, V. I. E. Queloz, Y. J. Hofstetter, D. Becker-Koch, P. Caprioglio, D. Neher, S. Orlandi, M. Cavazzini, G. Pozzi, J. Even, M. K. Nazeeruddin, Y. Vaynzof and G. Grancini, *Front. Chem.*, 2020, **7**, 946.
- 118 R. Ishikawa, K. Ueno and H. Shirai, *Org. Electron.*, 2020, **78**, 105596.
- 119 P. Cheng, Z. Xu, J. Li, Y. Liu, Y. Fan, L. Yu, D.-M. Smilgies, C. Müller, K. Zhao and S. F. Liu, *ACS Energy Lett.*, 2018, **3**, 1975–1982.
- 120 H. Tsai, W. Nie, J.-C. Blancon, C. C. Stoumpos, R. Asadpour, B. Harutyunyan, A. J. Neukirch, R. Verduzco, J. J. Crochet, S. Tretiak, L. Pedesseau, J. Even, M. A. Alam, G. Gupta, J. Lou, P. M. Ajayan, M. J. Bedzyk, M. G. Kanatzidis and A. D. Mohite, *Nature*, 2016, **536**, 312–316.
- 121 W. Fu, J. Wang, L. Zuo, K. Gao, F. Liu, D. S. Ginger and A. K.-Y. Jen, *ACS Energy Lett.*, 2018, **3**, 2086–2093.
- 122 X. Zhang, G. Wu, S. Yang, W. Fu, Z. Zhang, C. Chen, W. Liu, J. Yan, W. Yang and H. Chen, *Small*, 2017, **13**, 1700611.
- 123 Q. Zhou, Q. Xiong, Z. Zhang, J. Hu, F. Lin, L. Liang, T. Wu, X. Wang, J. Wu, B. Zhang and P. Gao, *Sol. RRL*, 2020, **4**, 2000107.
- 124 S. Tan, N. Zhou, Y. Chen, L. Li, G. Liu, P. Liu, C. Zhu, J. Lu, W. Sun, Q. Chen and H. Zhou, *Adv. Energy Mater.*, 2018, 1803024.
- 125 X. Wang, K. Rakstys, K. Jack, H. Jin, J. Lai, H. Li, C. S. K. Ranasinghe, J. Saghaei, G. Zhang, P. L. Burn, I. R. Gentle and P. E. Shaw, *Nat. Commun.*, 2021, **12**, 52.
- 126 C. Cai, J. Wan, Y. Zhang, Z. Yuan, Q. Huang, G. Xu, Y. Hu, X. Zhao and Y. Chen, *J. Polym. Sci., Part A: Polym. Chem.*, 2018, **56**, 116–124.
- 127 F. Bella, G. Griffini, J.-P. Correa-Baena, G. Saracco, M. Grätzel, A. Hagfeldt, S. Turri and C. Gerbaldi, *Science*, 2016, **354**, 203–206.
- 128 D. Bi, P. Gao, R. Scopelliti, E. Oveisi, J. Luo, M. Grätzel, A. Hagfeldt and M. K. Nazeeruddin, *Adv. Mater.*, 2016, **28**, 2910–2915.
- 129 S.-C. Chen, D. Wang and Q. Zheng, *Sol. RRL*, 2020, **4**, 2000321.
- 130 H. Zhu, Y. Ren, L. Pan, O. Ouellette, F. T. Eickemeyer, Y. Wu, X. Li, S. Wang, H. Liu, X. Dong, S. M. Zakeeruddin, Y. Liu, A. Hagfeldt and M. Grätzel, *J. Am. Chem. Soc.*, 2021, **143**, 3231–3237.
- 131 K. M. M. Salim, T. M. Koh, D. Bahulayan, P. C. Harikesh, N. F. Jamaludin, B. Febriansyah, A. Bruno, S. Mhaisalkar and N. Mathews, *ACS Energy Lett.*, 2018, **3**, 1068–1076.
- 132 C.-Y. Chang, C.-P. Wang, R. Raja, L. Wang, C.-S. Tsao and W.-F. Su, *J. Mater. Chem. A*, 2018, **6**, 4179–4188.
- 133 L. Jia, L. Zhang, L. Ding and S. Yang, *J. Semicond.*, 2021, **42**, 120201.
- 134 X. Liu, F. Lin, C.-C. Chueh, Q. Chen, T. Zhao, P.-W. Liang, Z. Zhu, Y. Sun and A. K.-Y. Jen, *Nano Energy*, 2016, **30**, 417–425.
- 135 R. Sandoval-Torrientes, J. Pascual, I. García-Benito, S. Collavini, I. Kosta, R. Tena-Zaera, N. Martín and J. L. Delgado, *ChemSusChem*, 2017, **10**, 2023–2029.
- 136 L. Jia, F. Huang, H. Ding, C. Niu, Y. Shang, W. Hu, X. Li, X. Yu, X. Jiang, R. Cao, J. Zhu, G.-W. Wang, M. Chen and S. Yang, *Nano Today*, 2021, **39**, 101164.
- 137 M. Wang, F. Cao and L. Li, *Small Struct.*, 2022, **3**, 2100165.
- 138 I. Neogi, A. Bruno, D. Bahulayan, T. W. Goh, B. Ghosh, R. Ganguly, D. Cortecchia, T. C. Sum, C. Soci, N. Mathews and S. G. Mhaisalkar, *ChemSusChem*, 2017, **10**, 3765–3772.
- 139 D. Giovanni, W. K. Chong, H. A. Dewi, K. Thirumal, I. Neogi, R. Ramesh, S. Mhaisalkar, N. Mathews and T. C. Sum, *Sci. Adv.*, 2016, **2**, DOI: [10.1126/sciadv.1600477](https://doi.org/10.1126/sciadv.1600477).
- 140 H. Zhang, Nobel Prize: How click chemistry and bioorthogonal chemistry are transforming the pharmaceutical and material industries, *The 2022 Nobel Prize in click chemistry and bioorthogonal chemistry*, <https://www.buffalo.edu/ubnow/stories/2022/10/nobel-prize-chemistry.html#:~:text=>
- 141 C. Raju, S. Kunnikuruvaan and K. M. Sureshan, *Angew. Chem., Int. Ed.*, 2022, **61**, e202210453.
- 142 F. De Angelis, *ACS Energy Lett.*, 2021, **6**, 1586–1587.
- 143 A. Bauer and N. Maulide, *Chem. Sci.*, 2021, **12**, 853–864.
- 144 K. N. Parida and J. N. Moorthy, *Synlett*, 2022, DOI: [10.1055/a-1813-7319](https://doi.org/10.1055/a-1813-7319).